Report on International Collaboration Involving the FE Heater and HG-A Tests at Mont Terri

Fuel Cycle Research & Development

Prepared for
U.S. Department of Energy
Used Fuel Disposition Campaign
Jim Houseworth, Jonny Rutqvist, Daisuke Asahina, Fei Chen, Victor Vilarrasa, H.H. Liu, Jens Birkholzer
Lawrence Berkeley National Laboratory

November, 2013
FCRD-UFD-2014-000002
LBNL-6635E

Revision 2
12/20/2012

APPENDIX E

FCT DOCUMENT COVER SHEET [1]

Name/Title of Deliverable/Milestone/Revision No.	Report on International Collaboration Involving the FE Heater and HG-A Tests at Mont Terri
Work Package Title and Number	Argillite Disposal R&D International – LBNL FT-14LB080606
Work Package WBS Number	1.02.08.06
Responsible Work Package Manager	Hui-Hai Liu (Signature on File)

Date Submitted 11/06/2013

Quality Rigor Level for Deliverable/Milestone[2]	☐ QRL-3	☐ QRL-2	☐ QRL-1 ☐ Nuclear Data	☒ Lab/Participant QA Program (no additional FCT QA requirements)

This deliverable was prepared in accordance with Lawrence Berkeley National Laboratory
(Participant/National Laboratory Name)

QA program which meets the requirements of
☒ DOE Order 414.1 ☐ NQA-1-2000 ☐ Other

This Deliverable was subjected to:

☐ Technical Review ☐ Peer Review

Technical Review (TR)

Review Documentation Provided

☐ Signed TR Report or,
☐ Signed TR Concurrence Sheet or,
☐ Signature of TR Reviewer(s) below

Peer Review (PR)

Review Documentation Provided

☐ Signed PR Report or,
☐ Signed PR Concurrence Sheet or,
☐ Signature of PR Reviewer(s) below

Name and Signature of Reviewers

_____ _____
_____ _____
_____ _____

NOTE 1: *Appendix E should be filled out and submitted with the deliverable. Or, if the PICS:NE system permits, completely enter all applicable information in the PICS:NE Deliverable Form. The requirement is to ensure that all applicable information is entered either in the PICS:NE system or by using the FCT Document Cover Sheet.*

NOTE 2: *In some cases there may be a milestone where an item is being fabricated, maintenance is being performed on a facility, or a document is being issued through a formal document control process where it specifically calls out a formal review of the document. In these cases, documentation (e.g., inspection report, maintenance request, work planning package documentation or the documented review of the issued document through the document control process) of the completion of the activity along with the Document Cover Sheet is sufficient to demonstrate achieving the milestone. If QRL 1, 2, or 3 is not assigned, then the Lab/Participant QA Program (no additional FCT QA requirements box must be checked, and the work is understood to be performed, and any deliverable developed, in conformance with the respective National Laboratory/Participant, DOE- or NNSA-approved QA Program.*

This page is intentionally blank.

SUMMARY

Nuclear waste programs outside of the US have focused on different host rock types for geological disposal of high-level radioactive waste. Several countries, including France, Switzerland, Belgium, and Japan are exploring the possibility of waste disposal in shale and other clay-rich rock that fall within the general classification of argillaceous rock. This rock type is also of interest for the US program because the US has extensive sedimentary basins containing large deposits of argillaceous rock. LBNL, as part of the DOE-NE Used Fuel Disposition Campaign, is collaborating on some of the underground research laboratory (URL) activities at the Mont Terri URL near Saint-Ursanne, Switzerland. The Mont Terri project, which began in 1995, has developed a URL at a depth of about 300 m in a stiff clay formation called the Opalinus Clay. Our current collaboration efforts include two test modeling activities for the FE heater test and the HG-A leak-off test. This report documents results concerning our current modeling of these field tests. The overall objectives of these activities include an improved understanding of and advanced relevant modeling capabilities for EDZ evolution in clay repositories and the associated coupled processes, and to develop a technical basis for the maximum allowable temperature for a clay repository.

The R&D activities documented in this report are part of the work package of natural system evaluation and tool development that directly supports the following Used Fuel Disposition Campaign (UFDC) objectives:

- Develop a fundamental understanding of disposal-system performance in a range of environments for potential wastes that could arise from future nuclear-fuel-cycle alternatives through theory, simulation, testing, and experimentation.
- Develop a computational modeling capability for the performance of storage and disposal options for a range of fuel-cycle alternatives, evolving from generic models to more robust models of performance assessment.

Major FY13 accomplishments and plans for future work in FY14 are briefly summarized below.

Major FY13 Accomplishments:

- For the purpose of validating modeling capabilities for thermal-hydro-mechanical (THM) processes, we developed a suite of simulation models for the planned full-scale FE Experiment to be conducted in the Mont Terri URL, including a full three-dimensional model that will be used for direct comparison to experimental data once available. We performed for the first time a THM analysis involving the Barcelona Basic Model (BBM) in a full three-dimensional field setting for modeling the geomechanical behavior of the buffer material and its interaction with the argillaceous host rock. We have simulated a well defined benchmark that will be used for code-to-code verification against modeling results from other international modeling teams. The analysis highlights the complex coupled geomechanical behavior in the buffer and its interaction with the surrounding rock and the importance of a well characterized buffer material in terms of THM properties.
- A new geomechanical fracture-damage model, TOUGH-RBSN, was applied to investigate damage behavior in the ongoing HG-A test at Mont Terri URL. Two model modifications have been implemented so that the Rigid-Body-Spring-Network (RBSN) model can be used for analysis of fracturing around the HG-A microtunnel. These modifications are (1) a methodology to compute fracture generation under compressive stress conditions and (2) a method to represent anisotropic elastic and strength properties. The method for computing fracture generation under compressive load produces results that roughly follow trends expected for homogeneous and layered systems. Anisotropic properties for the bulk rock were represented in the RBSN model

using layered heterogeneity and gave bulk material responses in line with expectations. These model improvements were implemented for an initial model of fracture damage at the HG-A test. While the HG-A test model results show some similarities with the test observations, differences between the model results and observations remain.

Suggested Future Work in FY14:

- We plan to continue our THM continuum modeling study along with the development of the FE experiment including (1) comparison of our benchmarking simulation results with those of the other international modeling teams, (2) modeling newly available laboratory experiments for constraining THM parameters of the MX-80 granular bentonite, and (3) providing a final prediction of the FE heater experiment (should be completed and reported before start of heating).
- We plan to continue HM fracture damage modeling activities related to the HG-A test. Modeling capability will be improved by testing and possibly modifying the approach for representing anisotropic properties in the RBSN method. Further testing and refinement of the method for computing fracture damage under compressive load will also be conducted. Existing fault features were not included in the current modeling effort for the HG-A test. Because damage zones in the HG-A test were found to be strongly associated with such features, it is important to include them for predicting damage. Looking forward to modeling the HG-A fluid injection tests, the TOUGH-RBSN coupled model needs to be exercised for a simulation of the HG-A excavation including dynamic pore-pressure response to fracturing and dryout. Finally, any model of the HG-A fluid injection tests will require extending the model to three dimensions.

CONTENTS

FIGURES

TABLES

ACRONYMS

BBM	Barcelona Basic Model
CIEMAT	Centro de Investigaciones Energéticas, Medioambientales y Tecnológicas
DOE	Department of Energy
EBS	Engineered Barrier System
EDZ	Excavation Damaged Zone
FEPs	Features, Events, and Processes
FLAC	Fast Lagrangian Analysis of Continua
LBNL	Lawrence Berkeley National Laboratory
NBS	Natural Barrier System
RBSN	Rigid-Body-Spring-Network

THM	Thermal-Hydrological-Mechanical
TOUGH	Transport of Unsaturated Groundwater and Heat
UFD	Office of Used Fuel Disposition Research and Development
UPC	Universitat Politècnica de Catalunya
URL	Underground Research Laboratory

This page is intentionally blank.

1. INTRODUCTION

Recognizing the benefits of international collaboration in the common goal of safely and efficiently managing the back end of the nuclear fuel cycle, DOE's Office of Nuclear Energy (NE) and its Office of Used Fuel Disposition Research and Development (UFD) have developed a strategic plan to advance cooperation with international partners (Birkholzer et al., 2013; UFD, 2012). UFD's strategic plan lays out two interdependent areas of international collaboration. The first area is cooperation with the international nuclear community through participation in international organizations, working groups, committees, and expert panels. Such participation typically involves conference and workshop visits, information exchanges, reviews, and training and education. The second area of international collaboration is active R&D participation of U.S. researchers within international projects or programs (UFD, 2012). By active R&D, it is meant here that U.S. researchers work closely together with international scientists on specific R&D projects relevant to both sides. With respect to geologic disposal of radioactive waste, such active collaboration provides direct access to information, data, and expertise on various disposal options and geologic environments that have been collected internationally over the past decades. Many international programs have operating underground research laboratories (URLs) in clay/shale, granite, and salt environments, in which relevant field experiments have been and are being conducted. Depending on the type of collaboration, U.S. researchers can participate in planning, conducting, and interpreting experiments in these URLs, and thereby get early access to field studies without having in situ research facilities in the United States.

UFD considers this second area, active international R&D, to be very beneficial in achieving the program's long-term goals of conducting "experiments to fill data needs and confirm advanced modeling approaches" (by 2015) and of having a "robust modeling and experimental basis for evaluation of multiple disposal system options" (by 2020). Advancing opportunities for active international collaboration with respect to geologic disposal has therefore been the primary focus of UFD's international strategy in the recent year (Birkholzer et al., 2013; Birkholzer, 2012).

Here we report LBNL's international activities related to the FE heater and HG-A tests at the Mont Terri URL near St. Ursanne in Switzerland. The objective of the URL is to provide hydrogeological, geochemical and rock mechanical properties of an argillaceous formation to evaluate the potential of argillaceous rock for disposal of high-level nuclear waste (Thurry and Bossart, 1999). The FE heater test is a full-scale long-term heater experiment being planned for the Mont Terri URL. A benchmark analysis using the thermal-hydrological-mechanical (THM) process model, TOUGH-FLAC, is reported here. The benchmark problem considers THM processes associated with excavation of the FE test tunnel followed by heating of the bentonite buffer and argillaceous rock. The benchmark exercise considers the four main stages of the FE heater test: (1) excavation; (2) installation of ground support, (3) emplacement of the heating canister and bentonite buffer; and (4) heating of the cannister. The benchmark is intended to allow comparison of the different THM process-level computer models being used by the participating organizations that are collaborating on the FE heater test and to predict important test results such as peak temperature and buffer resaturation rate. The HG-A test is an ongoing test which provides data on hydromechanical processes associated with the excavation damaged zone (EDZ) surrounding underground waste emplacement tunnels. Modeling of this test is presented here using the THM fracture-damage model, TOUGH-RBSN. RBSN is the Rigid-Body-Spring-Network model, which is a geomechanics and fracture damage model. Key aspects of this analysis are (1) the development of techniques for computing shear fracture; (2) development of techniques for representing anisotropic rock properties; and (3) prediction of fracture damage in the EDZ for the HG-A field test.

Within the Natural Barrier System (NBS) group of the Used Fuel Disposition (UFD) Campaign at DOE's Office of Nuclear Energy, LBNL's research activities have focused on understanding and modeling EDZ evolution and the associated coupled processes, and impacts of high-temperature on parameters and

processes relevant to performance of a clay repository. This report documents results from some of these activities, addressing key Features, Events and Processes (FEPs), that have been ranked in importance from medium to high, as listed in Tables 7 and 8 of the *Used Fuel Disposition Campaign Disposal Research and Development Roadmap* (FCR&D-USED-2011-000065 REV0) (Nutt, 2011). Specifically, they address FEP 2.2.01, Excavation Disturbed Zone, for shale, by investigating how coupled processes affect EDZ evolution; FEP 2.2.05, Flow and Transport Pathways; and FEP 2.2.08, Hydrologic Processes, and FEP 2.2.07, Mechanical Processes. The activities documented in this report also address a number of research topics identified in *Research & Development (R&D) Plan for Used Fuel Disposition Campaign (UFDC) Natural System Evaluation and Tool Development* (Wang, 2011), including Topics S3, Disposal system modeling – Natural system; P1, Development of discrete fracture network (DFN) model; P14, Technical basis for thermal loading limits; and P15 Modeling of disturbed rock zone (DRZ) evolution (clay repository).

2. THM MODELING OF FE EXPERIMENT

Within the framework of participating in the international Mont Terri Project (Thurry and Bossart, 1999), DOE is a partner in the FE Experiment at Mont Terri and supports LBNL to participate as one of several international modeling teams. In this section we present the FE Experiment and the current status of the modeling, including scoping calculations, benchmark simulations, and predictive calculations. To date, we have conducted a number of scoping calculations, have engaged in a comparative benchmarking effort, and have initiated some model predictions for the real experiment. In parallel with these modeling efforts, more data are becoming available on the THM properties of the MX-80 granular bentonite that is used as a backfill material in this experiment. In the modeling results presented in this report, we started with bentonite properties available from a previous experimental study (FEBEX bentonite), whereas we are gradually including material specific MX-80 properties into our analysis when they become available from ongoing laboratory and field experimental studies.

2.1 FE experiment at the Mont Terri site

The Full-Scale Emplacement Experiment (FE) at the Mont Terri URL, Switzerland will be one of the largest and longest-duration heater tests worldwide (Figures 2-1 through 2-3). This heater experiment is undertaken by NAGRA and other international partners as an ultimate test for the performance of geologic disposal in Opalinus Clay, with focus on both the EBS components and the host-rock behavior. The experiment will provide data useful for the validation of THM coupling effects regarding the processes in the host rock while correctly accounting for (and examining) the conditions in the emplacement tunnel (temperature, saturation, and swelling pressure). Due to the 1:1 scale of the experiment, it will be possible to achieve realistic temperature, saturation, and stress gradients. It will also be possible to test backfilling technology with granular bentonite, as well as lining technology with shotcrete, anchors, and steel rips. Processes examined in the test cover many aspects of repository evolution, such as EDZ creation and desaturation of the EDZ during tunnel excavation and operation (including ventilation for about one year), as well as reconsolidation of the EDZ, resaturation, thermal stresses, and thermal pore-pressure increase after backfilling and heating (heating and monitoring period > 10 years).

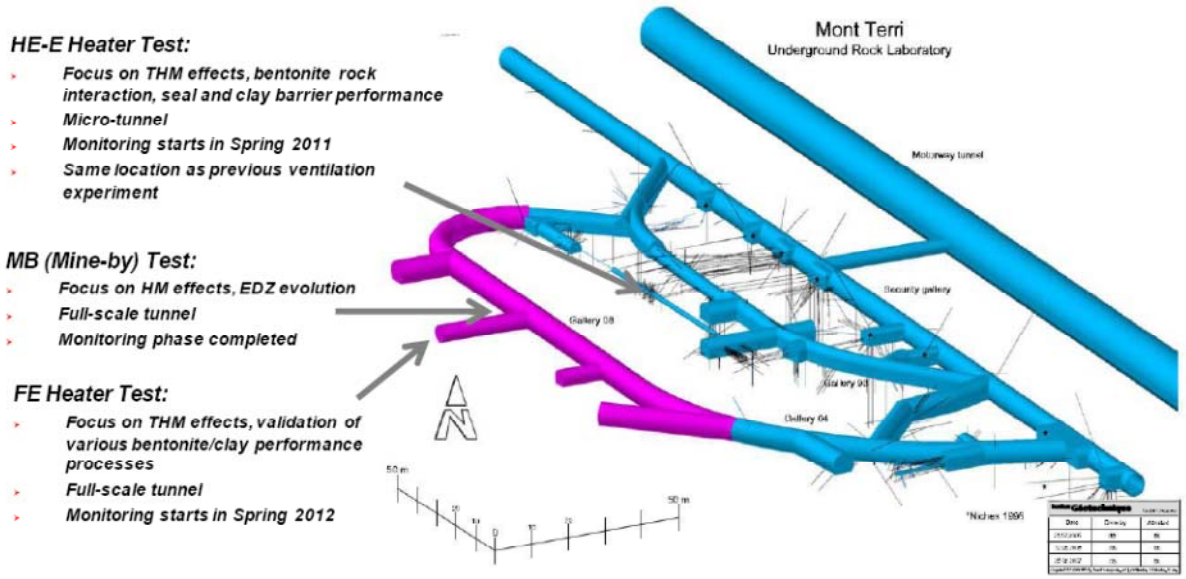

Figure 2-1. Summary schematic of the Mont Terri URL with side galleries and drifts for testing. Three specific experiments of relevance to UFDC are highlighted (based on Garitte and Gens, 2012).

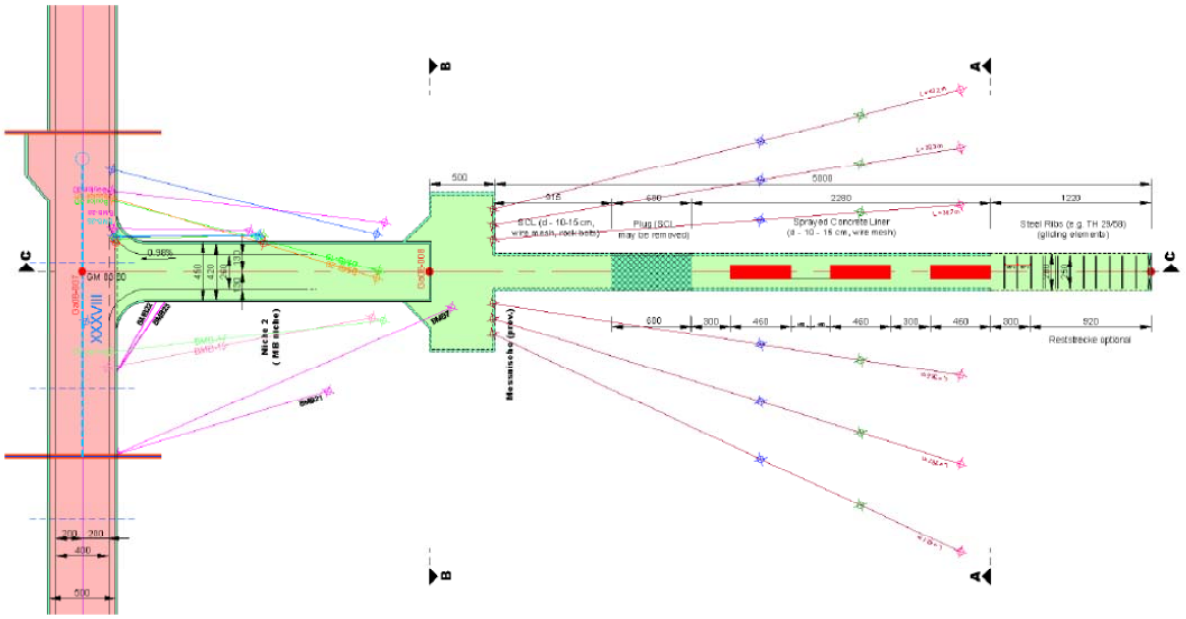

Figure 2-2. Plan view of experiment setup and borehole layout (from Garitte and Gens, 2012).

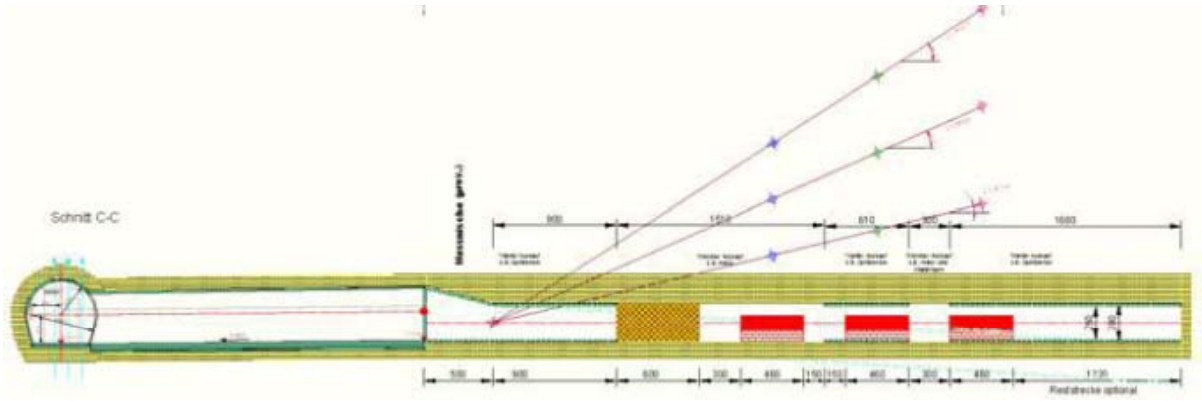

Figure 2-3. Side view of experiment setup and borehole layout (from Garitte and Gens, 2012).

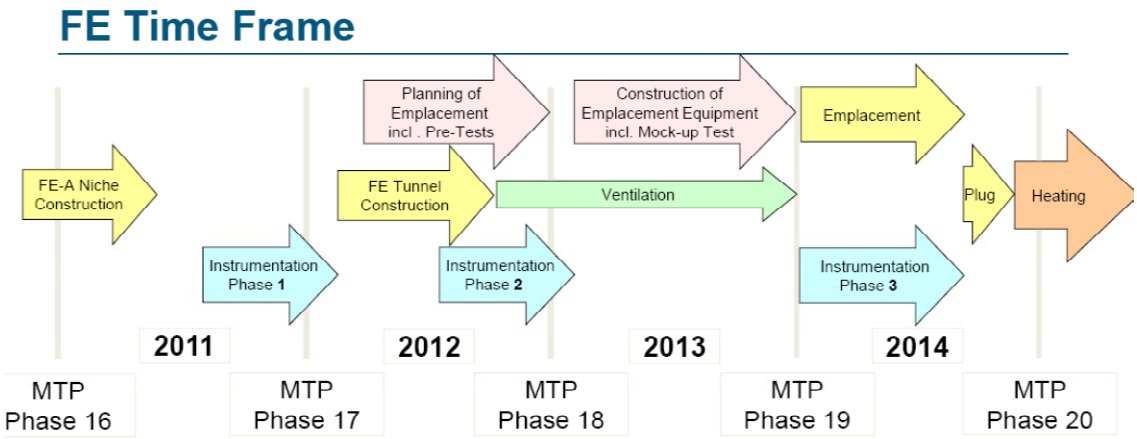

Figure 2-4. FE experiment time frame. Phases 16 to 20 refer to Mont Terri project phases (Vietor, 2012).

As shown in Figures 2-1 through 2-3, the FE experiment will be conducted in a side tunnel at Mont Terri, excavated along the claystone bedding planes for this purpose, extending 50 m in length and about 2.8 m in diameter. Heating from emplaced waste will be simulated by three heat-producing canisters of 1500 W maximum power. A sophisticated monitoring program is planned, including dense pre-instrumentation of the site for *in situ* characterization, dense instrumentation of the bentonite buffer and host rock, and extensive geophysical monitoring (seismic and electric tomography). A THM modeling program will be conducted in parallel with the testing and monitoring activities.

Figure 2-4 shows the FE experiment time frame (Vietor, 2012). A niche in front of the FE tunnel was constructed in 2011, followed by a first phase of instrumentation of the rock mass surrounding the tunnel using boreholes from the niche. The FE tunnel was then excavated by road-header in 2012, and this was followed by another phase of instrumentation. The tunnel is currently open for a 1-year ventilation period. This will be followed by the emplacement of the heaters, bentonite buffer, and a concrete plug, after which the heating is expected to start at the end of 2014. The heating is then expected to go on for at least 15 years, with continuous monitoring of THM processes in both the bentonite buffer and surrounding rock.

DOE is one of the experimental partners for the FE heater experiment, and LBNL is one of the modeling teams. The plans for the THM modeling program were determined in meetings with the FE modeling teams during 2012. Model simulation tasks for each of the international modeling teams (currently six modeling teams participate) include three types of computations:

1) Scoping computations
2) Benchmarking
3) Predictive simulations

The scoping computations included brainstorming on potential ongoing processes, evaluating their significance and parameter range, comparing simulation results and input parameters derived by each team, and lessons learnt (parameter range, importance, expected response). The benchmarking uses well-defined geometry problems with exact parameter values given to the teams, focusing on process modeling with precise comparison of codes. In the predictive calculations, likely parameters values and the as-built information of the experiment will be defined and then frozen as a starting point for all model teams. The modeling will be used to predict the behavior of the system, and this should be reported prior to heating start (in 2014). Currently, each modeling team develops their own conceptual models and material properties using available literature (papers and reports) on laboratory experiments and previous Mont Terri *in situ* tests etc. Moreover, this is complemented with a restricted benchmark test for code comparison, in which properties and model geometry are set by NAGRA. In the FY2012 NBS report, we presented our first initial 2D modeling of the FE experiment, including a parameter sensitivity study, to evaluate the importance of the different coupled processes and different components of the FE experiment. The following main conclusions were drawn from the FY2012 2D modeling of the FE experiment:

- The canister surface reaches the maximum temperature of 94.5°C after 4.8 years (for 2D model).
- The bentonite buffer resaturates very slowly and will still be unsaturated after 30 years.
- Temperature, water saturation, and pore pressure in the bentonite buffer are largely affected by the bentonite capillary pressure.
- Minor rock failure occurring during excavation does not expand much further during the assumed 20 years heating period, meaning that the rock mass will remain in an elastic mechanical state.

While the 2D analysis is very useful for performing such parameter studies, we also acknowledge that the 2D simplification does not provide an accurate quantitative prediction of the temperature evolution and the peak temperature. Consequently, in FY2013, we have developed a new full 3D model of the FE experiment. Using the 3D model, we conducted simulations, first for a prediction of the thermal-hydrologic evolution and then to predict the peak temperature. We have also conducted a full-scale 3D THM simulation using the Barcelona Basic Model for the bentonite buffer. Results using the new 3D model were also presented in a recent UFD milestone report (Liu et al., 2013).

2.2 Modeling approach

LBNL's model simulations of the FE experiment are carried out using the TOUGH-FLAC software (Rutqvist et al. 2002; 2011), which is based on linking the TOUGH2 multiphase flow and heat transport simulator (Pruess et al. 2011) with the FLAC3D geomechanical simulator (Itasca, 2009). The TOUGH-FLAC simulator has in recent years been extended and applied to issues related to nuclear waste disposal in clay host rock within bentonite backfilled tunnels (Rutqvist et al. 2011; 2013a). This includes implementation of the Barcelona Basic model (BBM), for the mechanical behavior of unsaturated soils and applied for modeling of bentonite back-fill behavior (Alonso et al. 1990). Recently, as part of the

UFD EBS program, the BBM has been extended to a double structure model, corresponding to the Barcelona Expansive Model (BExM), a model that we also plan to use for advanced modeling of the FE experiment. For the modeling of the FE experiment, we have developed an initial conceptual model and modeling approach based on experiences from recent design scoping calculations conducted by teams contracted by NAGRA, to help with the experimental design:

1) Pöyry (Engineering and Consulting): Modeling for excavation design using FLAC3D with ubiquitous joint model (anisotropic plasticity with different shear strength along bedding planes). This modeling approach was used to analyze the ground support design (Nater, 2012).
2) CIEMAT and UPC of Spain conducted scoping calculations for thermal and monitoring design using the CODE-Bright FEM code, and they used the BBM for modeling bentonite mechanical behavior (Garitte and Gens, 2012).
3) The Interra Swiss Branch performed 3D TOUGH2 model simulations with anisotropic properties and inclined mesh. Their modeling was limited to thermal-hydrological processes (no mechanics) and done for thermal and monitoring design (Ewing and Senger, 2011).

Our modeling approach contains important components from these three models. The host rock is modeled using TOUGH-FLAC with anisotropic properties considering bedding planes of the Opalinus Clay. The bedding planes across the FE tunnel can be seen in Figure 2-5. These bedding planes are oriented with its strike along the tunnel axis, and dipping about 45°. To accurately model anisotropic thermal and hydrological behavior, we created an inclined TOUGH2 mesh, the same way as done by the INTERA team. Anisotropic mechanical material behavior is simulated using the FLAC3D ubiquitous joint model, with initial properties of those derived from the excavation design analysis by the Pöyry team (Nater, 2012). For the bentonite, we started with the BBM model as applied by the CIEMAT and UPC (Garitte and Gens, 2012), and derived specific input material parameters for the MX-80 bentonite pellets that will be used as emplacing bentonite buffer around the heaters. With this modeling approach, we are able to simulate THM processes in both the bentonite and host rock, as well as their interactions.

Figure 2-5. View of FE tunnel face from the FE niche showing beddings dipping 45° (Vietor, 2012).

2.3 FE model setup

Figure 2-6 presents the new 3D numerical grid that has been developed as an extension of the previous 2D grid. This model grid includes all vital material components for the modeling of the FE experiment, including layered Opalinus Clay host rock, excavation disturbed zone, tunnel, three heaters, bentonite buffer, concrete liner, and concrete plug. The initial conditions for the model simulation are 2 MPa in pore fluid pressure and 15°C in temperature for the host rock. The 2 MPa of pore pressure is not under hydrostatic conditions, and the process is affected by the existing tunnel system at the site. In our simulations, we first run a simulation with an open tunnel at the atmospheric pressure for 1 year, creating a pressure drop and hydraulic gradient around the tunnel. Potential desaturation caused by ventilation effects will be considered in future simulations. Thereafter, we assume instantaneous emplacement of the heater and buffer, and start our heating simulation.

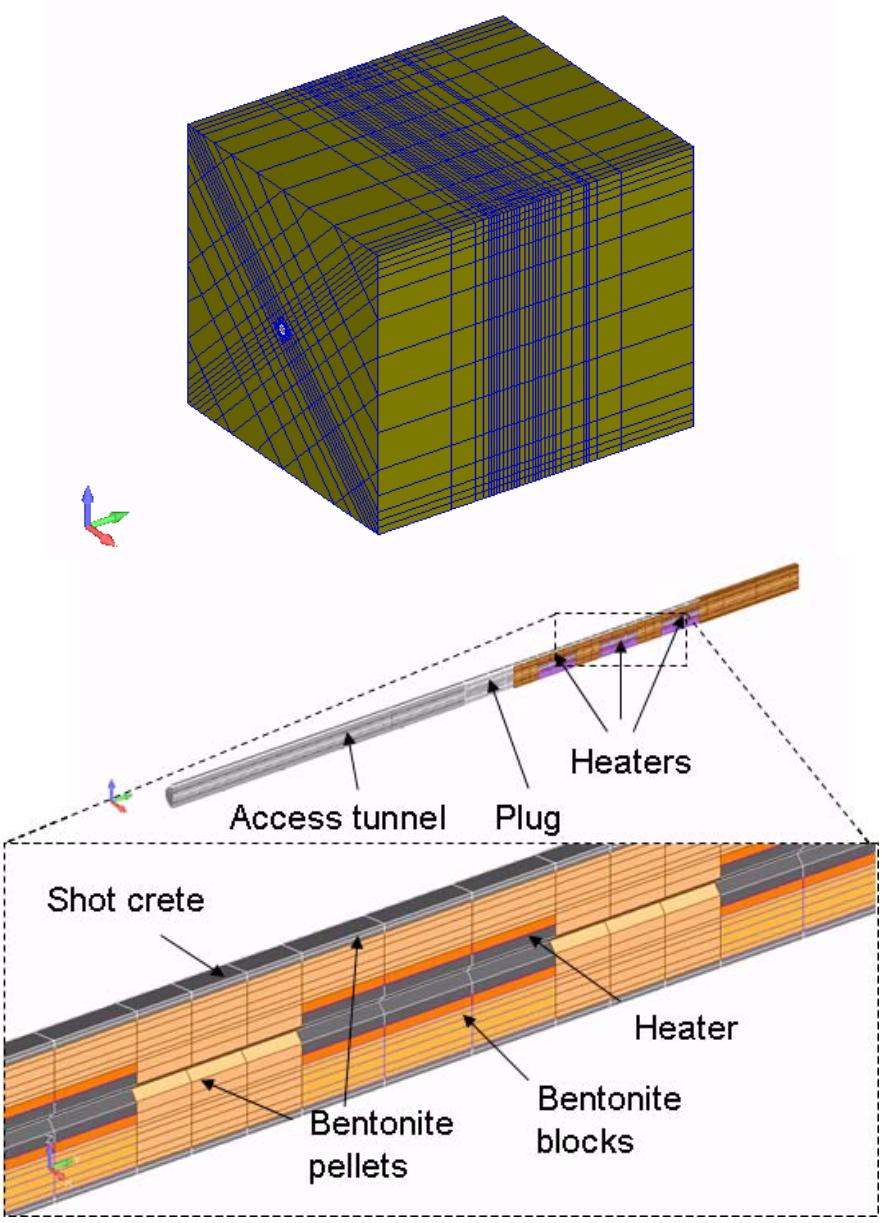

Figure 2-6. TOUGH-FLAC 3D numerical grid of the FE experiment (Rutqvist et al., 2013b).

Heating is assumed to occur for 20 years, according to the specifications set by NAGRA. The output from each of the heaters will be approximately 1500 W, and this is the heat power assumed in the current model. However, the heater power may be regulated to achieve a desired temperature evolution. For example, the targeted maximum temperature at the heater/bentonite interface is 125 to 135°C. On the other hand, a preliminary model simulation by the UPC team indicates that the temperature might not exceed 110°C, if the initial bentonite saturation is about 20 to 25%. A much higher peak temperature was calculated by the INTERA when assuming an initial saturation of 1%. Since buffer thermal conductivity depends on water saturation, the 1% initial saturation leads to a lower thermal conductivity in the buffer, which in turn results in a relatively high temperature at the heater/bentonite interface. A 1% saturation is reasonable for the pellets being deposited into the tunnel during buffer emplacement. However, experience from the ongoing HE-E heater test at Mont Terri shows that the bentonite pellets quickly draw moisture from the air and equilibrate with air relative humidity. Therefore, the initial buffer saturation of 18% is a reasonable value for the modeling.

Table 2-1. Parameters for the Opalinus and Bentonite clay used in the scoping calculation

Properties	Parameters	Symbol	Opalinus Clay	Bentonite	Unit
Physical	Grain density	ρ_s	2.7×10^{3}	2.7×10^{3}	kg/m^3
	Porosity	$\emptyset$	0.15	0.389	-
	Pore compressibility	B	1.0×10^{-9}	5.0×10^{-8}	Pa^{-1}
Hydraulic	Intrinsic permeability	K	5.0×10^{-20}	2.0×10^{-21}	m^2
	Liquid relative permeability	N	-	3	-
	Capillary curve	P_0	1.47×10^{7}	2.00×10^{7}	Pa
	Capillary curve	λ	0.595	0.51	-
	Capillary curve	S_{ls}	1.0	1.0	-
	Capillary curve	S_{lr}	0.01	0.00	-
Thermal	Thermal conductivity (wet)	λ_{sat}	2.0	1.3	W/m-K
	Thermal conductivity (dry)	λ_{dry}	2.0	0.3	W/m-K
	Grain specific heat	C	900	800	J/kg-K
Mechanical	Bulk modulus	K	4170	-	MPa
	Shear modulus	G	1920	-	MPa
	Cohesion	C	5	-	MPa
	Friction angle	ϕ	25	-	°
	Thermal exp. coeff.	α_T	1.0×10^{-5}	1.5×10^{-4}	1/°C
	Dilation angle	D	10	-	°
	Tensile strength	T	1.0	-	MPa
	Joint cohesion	C_J	2.2	-	MPa
	Joint friction	ϕ_J	23	-	°
	Joint tensile strength	T_J	0.5	-	MPa
	Joint dilation angle	d_J	10	-	°

The basic thermal and hydraulic material parameters are presented in Table 2-1. These are equivalent to the material parameters used in our previous 2D model analysis of the FE experiment. The properties for the Opalinus Clay are derived from Gens et al. (2007). We started with bentonite properties, including the thermal and hydraulic properties, derived from laboratory experiments and *in situ* tests related to the FEBEX experiment at Grimsel, Switzerland (Rutqvist et al., 2011). We then modified some of the properties to represent a bentonite buffer composed of MX-80 pellets. In our initial modeling we also consider the water-retention curves for the bentonite and Opalinus Clay as important parameters for the behavior. The capillary curves used in the model are shown in Figure 2-7. We use the van Genuchten formulation to describe the water-retention characteristic curves (van Genuchten, 1980):

$$P_c = -P_0 \left[\left(\frac{S_l - S_{lr}}{S_{ls} - S_{lr}} \right)^{-1/\lambda} - 1 \right]^{1-\lambda} \quad (2\text{-}1)$$

where P_0 is the air entry pressure, S_l is water saturation, the subscripts ls and lr refer to the fully saturated and residual conditions, respectively, and λ is a curve fitting parameter. These values are presented in Table 2-1. Those for the Opalinus Clay are taken from the previous simulation and fit against a series of laboratory and *in situ* measurements (Garitte et al., 2013), and those for bentonite clay are adjusted to match an *in situ* measurement of the initial state at the Mont Terri site (approximately 100 MPa at water saturation of 20%).

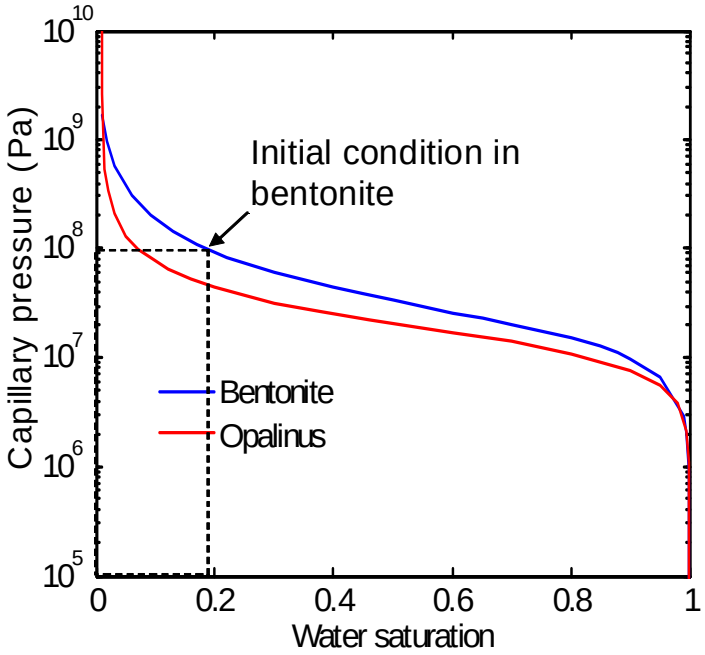

Figure 2-7. Capillary curves for Bentonite and Opalinus clays

2.4 3D TH scoping calculations with comparison to 2D results

Figure 2-8 shows the TH results from the new 3D analysis, and in Figure 2-9 we compare the results of the new 3D and the previous 2D analyses, where the 2D model domain is a cross section orthogonal to the tunnel axis. The monitoring points in the 3D model are located at the middle of the center heater at different radial distances from the tunnel axis. In the new 3D simulation, the peak temperature in the bentonite near the heater surface (0.55 m) is higher than in the 2D analysis; it is about 120°C (Figure 2-8(a)). Similar to the 2D analysis, the buffer is not fully saturated after 30 years (Figure 2-8(b)). At the buffer and concrete interface (1.18 m), the temperature peaks at about 67°C after 20 years, i.e., slightly lower than in the 2D analysis. Consistent with the previous 2D analysis, as soon as the bentonite buffer is installed, liquid water is pulled from the host rock due to the strong capillary pressure at an initial saturation of 18%. Water saturation near the bentonite buffer and concrete liner interface (1.18 m in Figure 2-8 (b)) increases immediately after the installation; correspondingly, a slight desaturation is observed in the host rock. The resaturation process is quite slow due to the low permeability of the host rock and bentonite buffer. The water saturation near the canister is approximately 68% after 30 years.

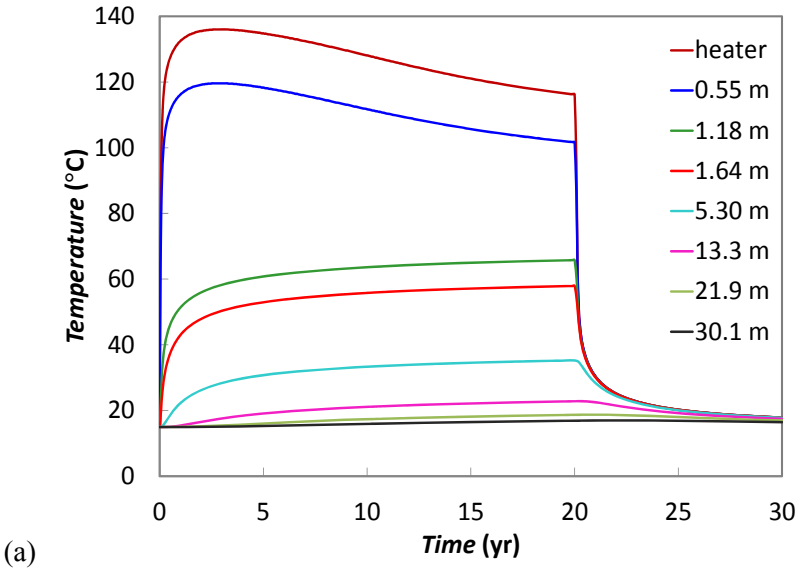

(a)

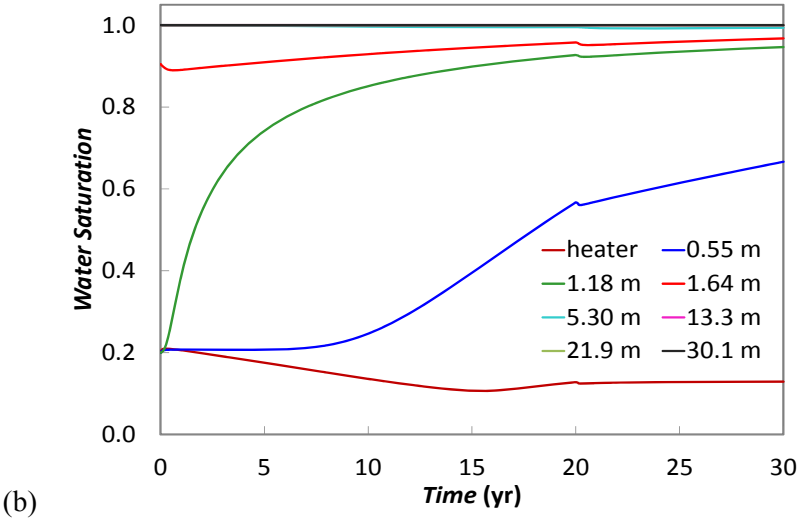

(b)

Figure 2-8. 3D simulation results related to the evolution of TH processes in the buffer and host rock: (a) temperature, (b) liquid saturation. Monitoring points are located at the middle of the center heater at different radial distances from the tunnel axis.

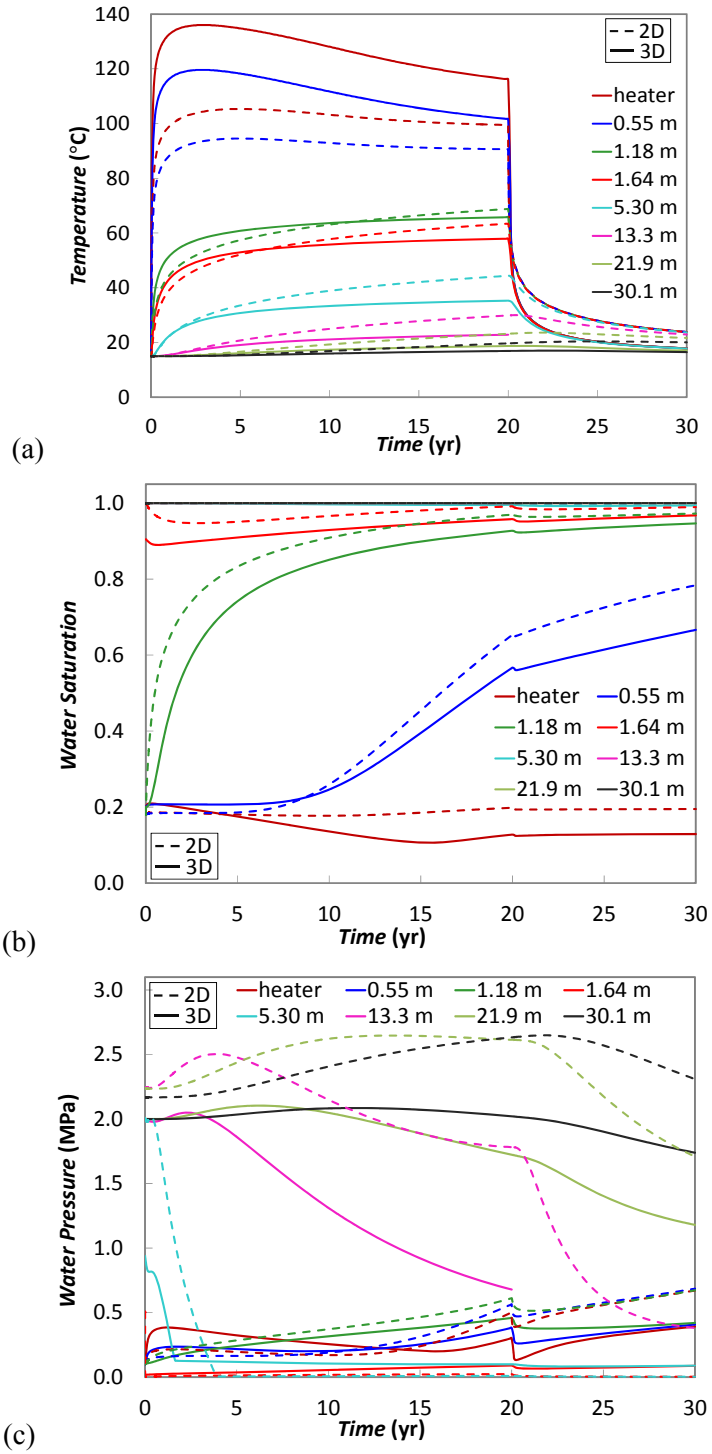

Figure 2-9. Comparison of previous 2D and new 3D simulation results: (a) temperature, (b) liquid saturation, (c) fluid pressure.

The pore-pressure evolution is rather complex in the buffer and rock system around the FE experiment, but these are all responses that can be explained by the coupled TH processes. The pressure increases gradually in the bentonite buffer along with the resaturation of the buffer. The host rock near the concrete/Opalinus interface experiences a sudden depressurization after the installation of the bentonite buffer. Because the rock is unsaturated, the pore pressure remains low during the 20 years of heating.

However, the deep host rock (>13.3 m away from canister) is pressurized owing to the increase in temperature in the first few years, whereupon the pressure declines again as a result of suction from the bentonite-filled tunnel.

In the comparison of the new 3D versus the previous 2D analysis, we can observe that the most significant difference occurs in the temperature evolution close to the heater and in the pressure evolution in the Opalinus Clay at some distance away from the tunnel (Figure 2-9). The 3D analysis predicts a higher peak temperature at the heater; this is expected, because in the 2D analysis the heat load was based on an average line thermal load of 197 W/m, taking into account the spacing between individual heaters. The 3D analysis is more accurate for calculating the peak temperature at the mid-heater surface; this was about 120°C compared to 94°C for the 2D analysis. The fluid pressure in the host rock away from the tunnel is different in terms of magnitude of thermal pressurization, which is significantly higher in the case of the 2D model analysis. In the 2D analysis, an incremental pressure increase of about 0.5 MPa can be observed (e.g., black dashed line in Figure 2-9(c)), whereas the maximum pressure increase is about 0.1 MPa in the 3D analysis (e.g., black solid line in Figure 2-9(c)). The thermal pressurization is lower in the case of the 3D analysis, because the pressure can escape in the third dimension, whereas in the 2D analysis, the pressure is confined within the 2D model.

2.5 Study of peak temperature considering diffusion

In the previous simulation, we had neglected diffusion of water vapor, which is an important process for capturing early time drying of the bentonite buffer near the heater. We therefore conducted another simulation in which we assigned a diffusion coefficient of 1.73e-5 m^2/s. Figure 2-10 presents the evolution of temperature and saturation in the case where the thermal diffusion causes drying and a decrease in saturation near the heater. This reduction in liquid saturation results in a lower buffer thermal conductivity and (consequently) a higher peak temperature of 130°C. We note that the evolution of the liquid saturation in the buffer is important for the peak temperature, and that 130°C is right within the targeted 125 to 135°C temperature range. However, further analysis should be made once the accurate thermal properties have been determined for the MX-80 granular bentonite to be used in the actual experiment. For example, in our first predictive analysis presented in Section 2.7, we used parameters that are likely to be more representative of the MX-80 granular bentonite, and in that case a substantially higher peak temperature is predicted.

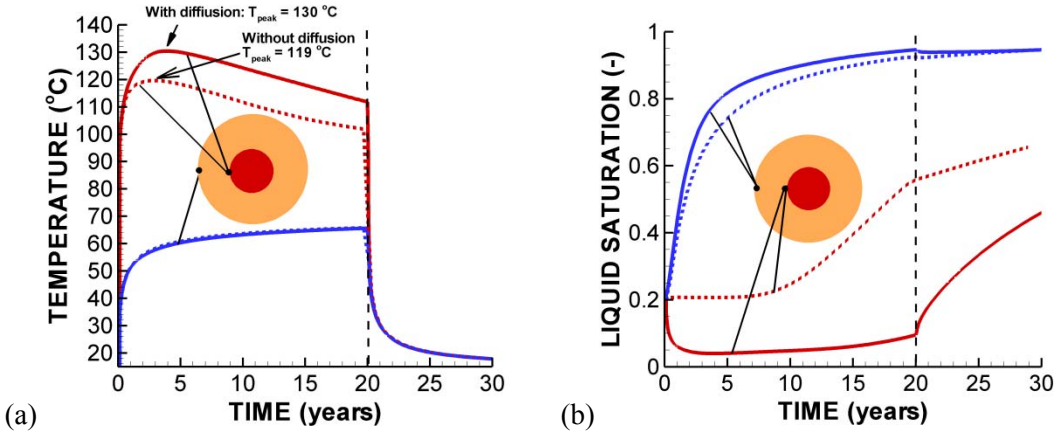

Figure 2-10. Simulation results considering drying induced by diffusion of water vapor within the buffer: (a) temperature, (b) liquid saturation.

2.6 3D THM scoping simulation using the BBM

We have conducted new modeling simulations using (for the first time) the BBM in a full 3D setting. The BBM (Alonso et al., 1990) has been implemented into TOUGH-FLAC as part of the UFD EBS program. BBM is a constitutive model for elasto-plastic mechanical behavior of unsaturated soil, which has been applied for modeling of bentonite-buffer behavior (Gens et al., 2009). It includes important coupled hydraulic and mechanical features such as strengthening and stiffening with drying. In this model simulation, we are using the same TH properties, which are given in Table 2-1. In addition, we now add the material parameters for the BBM, which are given in Table 2-2. The parameters for the BBM used in this initial 3D THM model simulation are those derived for FEBEX bentonite by Gens et al. (2009), and also applied in Rutqvist et al. (2013a) for the modeling of THM processes around a generic nuclear waste repository. A large number of material parameters are required to describe the THM material behavior, and those given in Table 2-2 have been determined from laboratory experiments. As mentioned, for the rock-mass behavior, we used a ubiquitous joint model (anisotropic plasticity with different shear strength along bedding planes) consistent with the previous ground-support design analysis (Nater, 2012). The rock mechanical properties for the Opalinus Clay were taken from Corkum and Martin (2007).

A significant number of measurements using different procedures (borehole slotter, undercoring, and hydraulic fracturing) of the in situ stress have been made at Mont Terri. A synthesis of these is given in Garitte et al. (2013):

- Major principal stress is subvertical and corresponds approximately with overburden weight (about 7MPa)
- The magnitude of the intermediate principal stress obtained from the undercoring technique is consistent with the results from hydraulic fracture tests (about 5MPa)
- The value of the minor principal stress is quite low and probably controlled by the presence of a deep valley to the SW of the laboratory. A low value of the minor principal stress is consistent with the small number of breakouts observed in vertical boreholes (about 2MPa).

In our modeling we then set the vertical stress to 7 MPa, whereas the maximum horizontal stress perpendicular to the tunnel is set to 5 MPa.

Figure 2-11 shows the simulated stress evolution in the buffer; Figure 2-12 shows the evolution of the mean effective stress and bulk modulus in the buffer. The compressive stress increases along with the resaturation of the buffer, which first takes place at the tunnel wall. The maximum stress at the end of heating (20 years) is about -2.5 MPa (compressive stress), with highest maximum occurring at the tunnel wall, i.e., at the buffer and concrete lining interface. After 20 years, there is a sudden drop in compressive stress as a result of the temperature drop once the heater is turned off. This drop in buffer stress, caused by the cooling shrinkage, results in a substantial stress drop because the buffer is relatively stiff at that time (Figure 2-12). The radial compressive stress in the buffer is quite uniform (similar to the magnitude at the heater and concrete lining) and is about -1.7 MPa at the end of this simulation. This compressive stress is applied on the concrete lining and supports the rock wall.

The rock stress evolution is shown in Figure 2-13. The initial stress is quite anisotropic at the tunnel wall, with a relatively high tangential stress, while the radial stress is small as a result of the free rock surface. However, the concrete lining provides some support, so the radial stress is not zero, but rather a few MPa. During the heating of the rock, and as a result of the buffer swelling, the stress changes with time (as expected). At 20 years, the stress at the tunnel wall is about -3.3 MPa, which is higher than initial, as the swelling pressure from the buffer provides some support to the rock wall. Note that in our FY2012 report, we presented 2D results for stress evolution using a simple swell model for the buffer and achieved a

higher swelling stress in the buffer. The magnitude of this swelling stress depends on the parameter input governing the swelling in both the simple swell model and the BBM. However, the higher swelling pressure in our previous model simulation resulted in more substantial effects on the rock stress near the tunnel wall, making the stress more isotropic than was achieved in the current 3D model simulation. A detailed back analysis of swelling stress parameters will be made for the MX-80 granular bentonite material to be used in the FE experiment.

Table 2-2. BBM material parameter values for the bentonite buffer (Gens et al., 2009)

Parameter	**Value**
Compressibility parameter for stress-induced elastic strain, κ_{PS0} [-]	0.05
Compressibility parameter for suction-induced elastic strain, κ_{SP0} [-]	0.25
Shear modulus, G [MPa]	NA
Poisson's ratio, ν [-]	0.4
Parameter for suction induced elastic strain, α_{SS} [-]	0
Parameter for stress-induced strain α_{PS} [MPa^{-1}]	-0.003
Parameter for stress-induced strain, α_{SP} [-]	-0.161
Reference stress state for relating elastic compressibility to suction, P_{ref} [MPa]	0.5
Parameters that relate elastic volumetric strain and temperature changes, α_0 [$°C^{-1}$]	1.5e-4
Compressibility parameter in virgin soil states at zero suction, λ_{PS0} [-]	0.15
Parameter defining soil stiffness associated with loading collapse yield, r_λ [-]	0.925
Parameter for the increase of soil stiffness with suction, β_λ [MPa^{-1}]	0.1
Parameter that relates cohesion to temperature, ρ_s [$°C^{-1}$]	0
Parameter describing the increase of cohesion with suction, k_s [-]	0.1
Tensile strength at saturated conditions, P_{S0} [MPa]	0
A reference stress state for compressibility relation in virgin states, P^C [MPa]	0.5
Slope of the critical state line, M [-]	1
Nonassociativity parameter in the plasticity flow rule, α_a [-]	0.53
Specific volume at reference stress states P^C in virgin states, v^c [-]	1.937
Net mean yield stress for saturated conditions at reference temperature, P^*_{0T} [MPa]	12.0

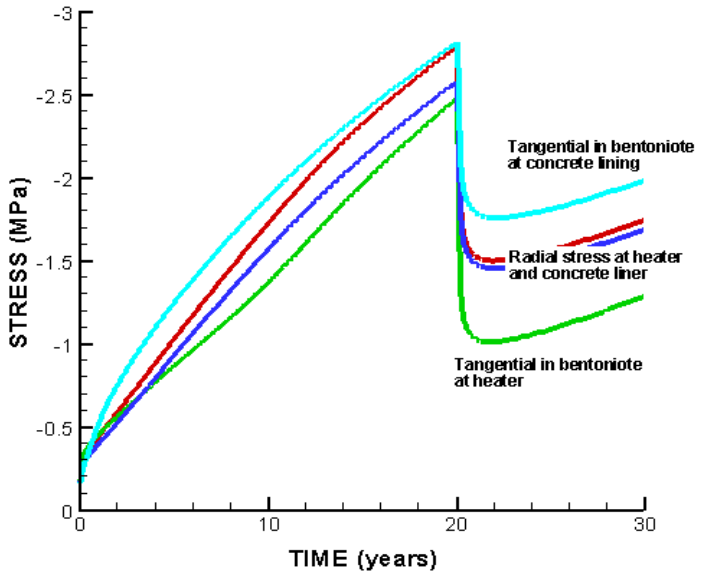

Figure 2-11. Simulated stress evolution within the bentonite buffer.

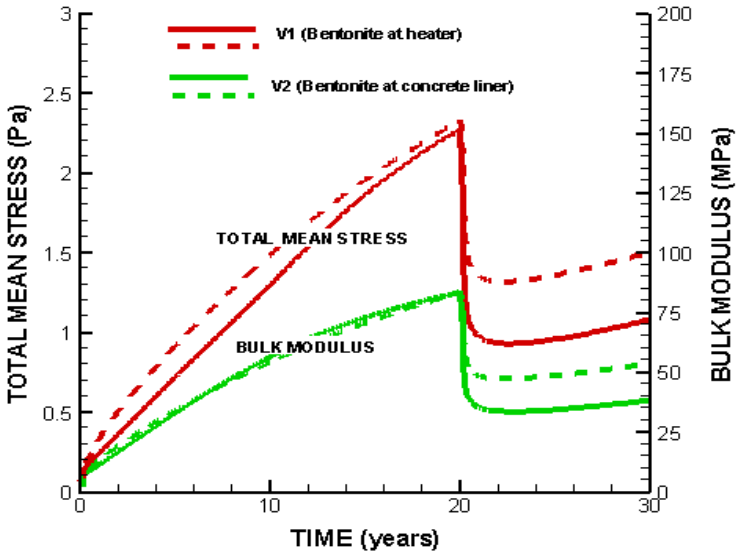

Figure 2-12. Simulated evolution of mean stress and bulk modulus within the buffer.

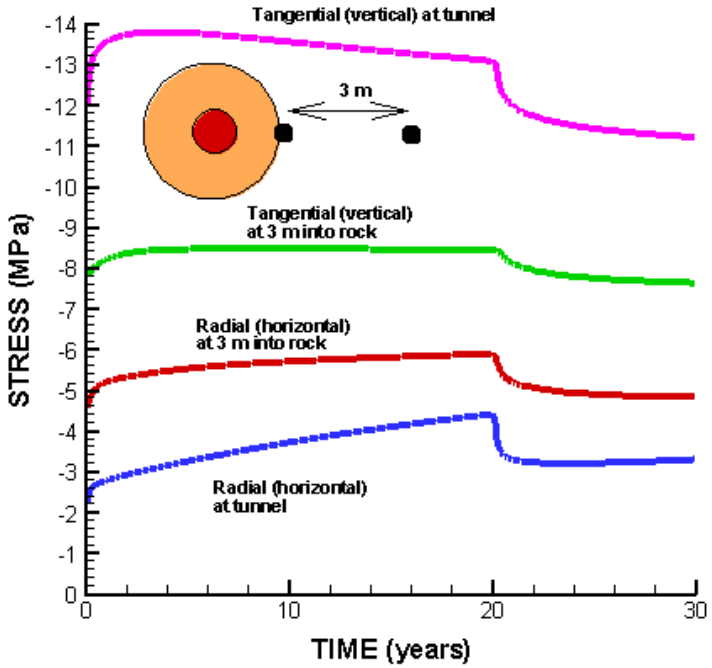

Figure 2-13. Simulated stress evolution within the Opalinus Clay.

2.7 1D axisymmetric benchmark calculation

A benchmark calculation has been defined by NAGRA aiming at validating the different models used for the THM analysis of the FE experiment (Garitte, 2013). The models developed for this benchmark aim at reproducing the THM response of the backfill material and the rock considering the simplest possible approach. The model results will thus not be representative of the response expected in the real FE experiment. Our approach was to first conduct a TOUGH2 simulation to calculate TH responses, uncoupled from geomechanics. Then, we conducted a full TOUGH-FLAC simulation to add geomechanical processes to the analysis.

2.7.1 Definition of the Benchmark

The modeling of the benchmark involves simulation of initial conditions, tunnel excavation, emplacement of shotcrete, emplacement of backfill and finally heating. The geometry and initial and boundary conditions for each of these steps are shown in Figure 2-14 and summarized in Table 2-3. The model domain shown in Figure 2-14 represents a 1D slice of Opalinus Clay of 30 m radial extension with:

- an axisymmetric axis on the left boundary and
- a temperature of 15°C, a pore water pressure of 2 MPa and 5 MPa normal stress on the right boundary. The right boundary condition will remain in this state throughout the simulation.

Before tunnel excavation, Opalinus Clay is considered saturated, with a pore water pressure of 2 MPa and isotropic stress state of 5 MPa, and an initial temperature of 15°C (Figure 2-14a).

The tunnel excavation is simulated by removing instantaneously 1.5 m of Opalinus Clay at the centre of the model. The new left boundary condition is characterized by 0 normal stresses, a pore water pressure of 0 MPa and a temperature of 15°C (Figure 2-14b).

The shotcrete is emplaced one day after the tunnel excavation (Figure 2-14c). The shotcrete is initially saturated, with 0 MPa of pore water pressure, a temperature of 15°C and the initial stress state is 0 MPa. The new left boundary condition is characterized by 0 normal stresses, a pore water pressure of -20 MPa and a temperature of 15°C.

The backfill material is emplaced 668 days after the shotcrete (Figure 2-14d). As a consequence of the 1D assumption no difference can be made between the bentonite blocks and the bentonite pellets mixture. The initial conditions of the bentonite are:

- Degree of saturation of 18.5% and dry density of 1.45.
- Pore water pressure: according to retention curve (see parameters section)
- Temperature of 15°C
- 0 MPa stresses

The new left boundary condition is characterized by zero displacement, no water, and no heat flux.

Heating is turned on 1 day after the bentonite has been emplaced. A constant heat flux of 325 W/m is applied on the left boundary. This heat flux was determined as 1500 W (heat output of one heating device) divided by the length of a heating device.

The material parameters were strictly defined by NAGRA, but may have to be adjusted depending on the specific numerical model used by a modeling team. We discuss how the material parameters were input to the TOUGH2 TH model in Section 2.7.2 and to the TOUGH-FLAC THM model in Section 2.7.4.

Table 2-3. Summary of the initial and boundary conditions. Start of each action is referenced to the start of heating

Action	Start (Days)	Left boundary condition				Initial conditions new material			
		Position	T	H	M	Material	T	H	M
Excavation	-670	1.5m	15°C	0MPa	0MPa	Opa.	15°C	2MPa	5MPa
Shotcrete emplacement	-669	1.35m	15°C	-20MPa	0MPa	Shotcrete	15°C	0MPa	0MPa
Bentonite emplacement	-1	0.525m	0W/m	0 flux	0 displ.	Bentonite	15°C	Sr=18.5%	0MPa
Heating	0	0.525m	325W/m	0 flux	0 displ.	-	-	-	-

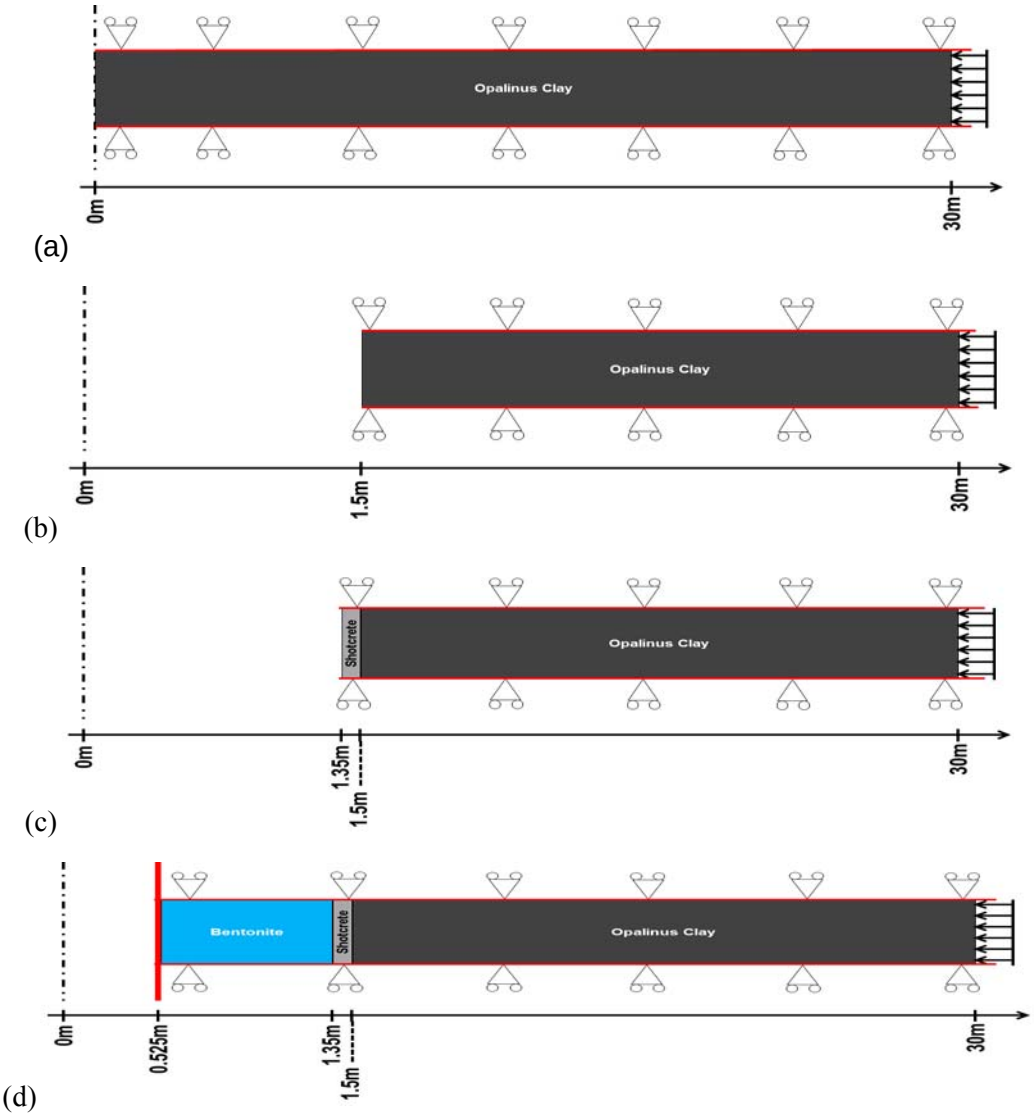

Figure 2-14. Model geometry and boundary conditions at (a) initial state, (b) after excavation, (c) after shotcrete emplacement, and (d) after emplacement of backfill material (Garitte, 2013)

2.7.2 Setup of a TOUGH2 model for TH analysis

The system is a one-dimensional, radial slice of the buffer and rock out of an infinitely long cylinder (Figure 2-15). The origin of the radial coordinate system is at the center of the waste package and extends out to 30 m. The system is modeled in stages starting with tunnel excavation, followed by shotcrete emplacement, followed by buffer emplacement, and then by heating from the waste package. The model domain was discretized into 323 cells with the radial dimensions given in Table 2-4. The cell thickness is a constant 1 m. A large-volume cell is also included at the end of the rock section to maintain constant thermodynamic conditions at the rock boundary.

Table 2-4. TOUGH2 numerical discretization of the 1D BMT

Component	Number of cells	Cell size (m)
Buffer	1	0.005
Buffer	82	0.01
Shotcrete	15	0.01
Rock	50	0.01
Rock	50	0.1
Rock	115	0.2

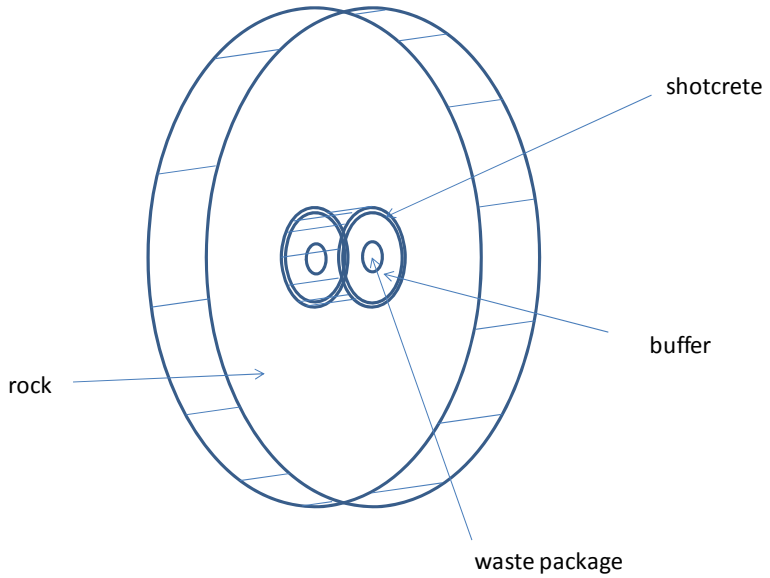

Figure 2-15. Three-dimensional view of overall problem domain.

In the TOUGH2 simulation of this problem, the model domain changes for the different stages according to the benchmark description, and the exact initial and boundary conditions used in the model are presented in Figure 2-16. Stages 1 to 3 are simulated to provide correct initial conditions for the heating in Stage 4. The heat flux for Stage 4 was applied at the inner buffer radius into a cell representing the heater. As mentioned before, according to the benchmark definition, heat flux was applied at a constant rate of 325 W/m.

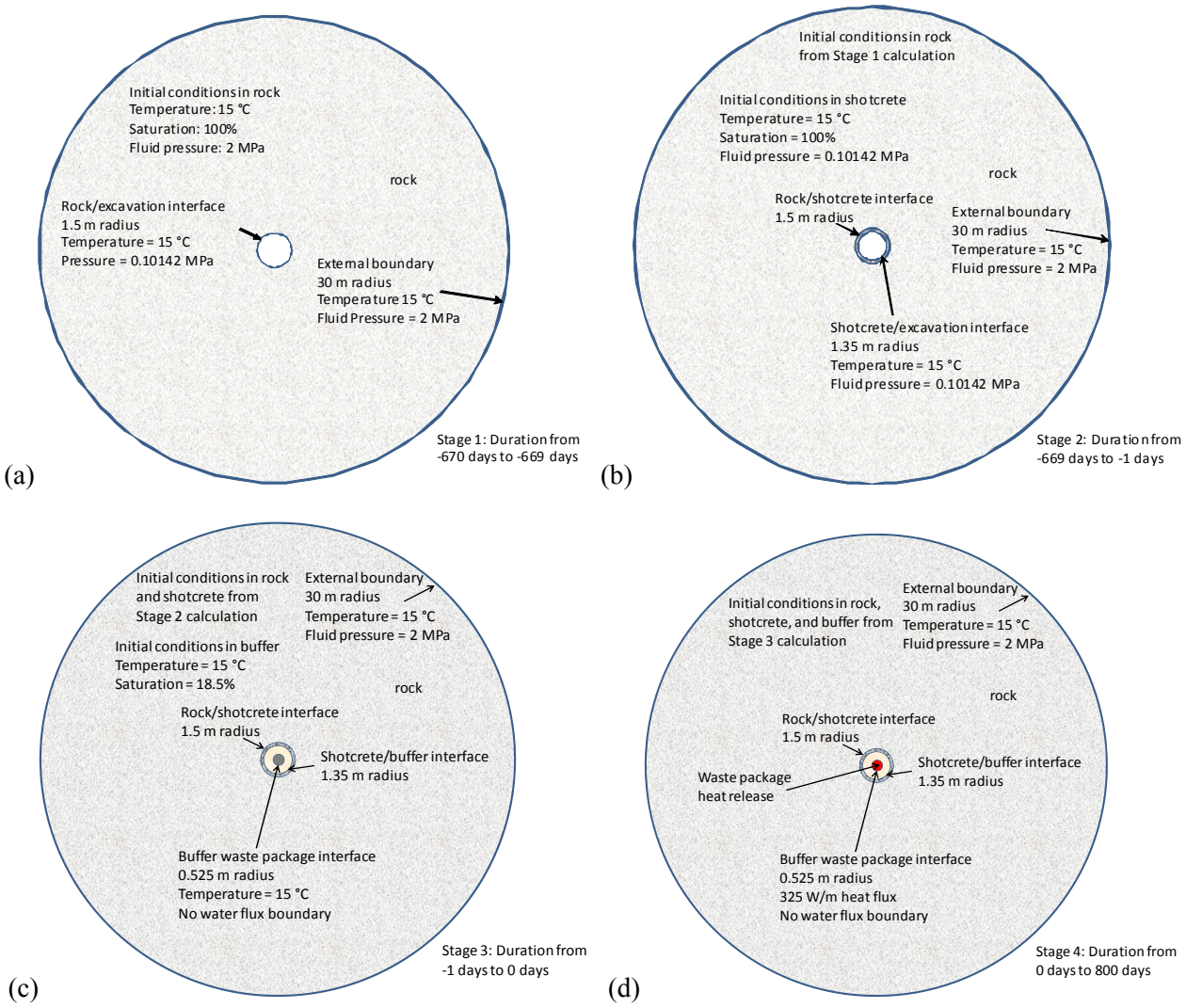

Figure 2-16. TOUGH2 model conditions during (a) Stage 1 (-670 to -669 days), (b) Stage 2 (-669 to -1 day), (c) stage 3 (-1 to 0 days), and (d) stage 4 (0 to 800 days)

The parameters used in the TOUGH2 model are those defined in the task description and given in Table 2-5. Note that there are differences in values of some of these parameters compared to those used in the previous scoping calculation. Most significantly, the thermal conductivity of the both the buffer and the rock are lower than those used in the scoping calculation.

Table 2-5. Parameters for FE 1-D benchmark.

	Overpack	Buffer	Shotcrete	Rock
Solids density (kg/m^3)	8000.	2700.	2700.	2700.
Porosity	0.46	0.46	0.15	0.15
Permeability (m^2)	5 x 10^{-52} (3,4)* 5 x 10^{-11} (1,2)*	3.5 x 10^{-21}	3.5 x 10^{-21}	3.5 x 10^{-20}
Thermal conductivity (saturated) (W/m-K)	20.	1.	1.7	1.7
Specific heat (solids) J/kg-°C	490.	950.	800.	800.
Thermal conductivity (desaturated) (W/m-K)	20.	0.3	1.06	1.06
Tortuosity	10^{-11} (3,4)* NA (1,2)*	1.	1.	1.
Water relative permeability parameter A, (Equation (2-2))	1.3	5	NA	NA
Water relative permeability residual saturation, S_r (Equation (2-2))	0.	0.	NA	NA
Water relative permeability maximum saturation, S_m (Equation (2-2))	1.	1.	NA	NA
Water relative permeability parameter m, (Equation (2-3))	NA	NA	0.52	0.52
Water relative permeability residual saturation, S_r (Equation (2-3))	NA	NA	0.0071	0.0071
Water relative permeability maximum saturation, S_m (Equation (2-3))	NA	NA	1.	1.
Capillary pressure parameter, α (Pa^{-1}) (Equation (2-4))	10^{-7}	10^{-7}	9.091 x 10^{-8}	9.091 x 10^{-8}
Capillary pressure parameter, m, (Equation (2-4))	0.4	0.4	0.29	0.29
Capillary pressure residual saturation, S_r (Equation (2-4))	0.	0.	0.0071	0.0071
Capillary pressure maximum saturation, S_m (Equation (2-4))	1.	1.	1.	1.
Vapor and air diffusion coefficients (D in Equation (2-6)) (m^2/s)	2.68 x 10^{-5}	2.68 x 10^{-5}	2.68 x 10^{-5}	2.68 x 10^{-5}
Vapor and air diffusion temperature exponents, (n in Equation (2-6))	2.3	2.3	2.3	2.3

*The numbers in parentheses indicate to which of the four stages the parameter applies (tunnel excavation is 1, shotcrete emplacement is 2, bentonite emplacement is 3, and heating is 4).
NA = not applicable

The water relative permeability in the buffer is a power-law relationship given by

$$k_{rw}(S_w) = \left(\frac{S_w - S_r}{S_m - S_r}\right)^A \qquad (2\text{-}2)$$

The water relative permeability in the shotcrete and rock is given by the van Genuchten relationship

$$k_{rw}(S_w) = \left(\frac{S_w - S_r}{S_m - S_r}\right)^{1/2}\left[1 - \left\{1 - \left(\frac{S_w - S_r}{S_m - S_r}\right)^{1/m}\right\}^m\right]^2 \quad (2\text{-}3)$$

Capillary pressure in the buffer, shotcrete, and rock are given by the van Genuchten relationship:

$$\psi(S_w) = \frac{1}{\alpha}\left\{\left(\frac{S_w - S_r}{S_m - S_r}\right)^{-1/m} - 1\right\}^{1-m} \quad (2\text{-}4)$$

The relative permeability to gas for the buffer is set to a constant value of 1. The relative permeability to gas in the shotcrete and rock is:

$$k_{rg}(S_w) = 1 - k_{rw}(S_w). \quad (2\text{-}5)$$

Variations in thermal conductivity and specific heat with water saturation are assumed to be linear between the defined end points. The vapor and air diffusion coefficients are a function of temperature and gas saturation defined by:

$$D_g^w = \tau S_g D \frac{P_{g0}(273.15+T)^n}{P_g(273.15)^n} \quad (2\text{-}6)$$

The problem was solved using TOUGH2 with the EOS4 equation-of-state module. From the simulations of this benchmark test, we discovered some numerical instability in the water saturation when the relatively high diffusion coefficient listed in Table 2-5 was used. One remedy to avoid such numerical instability was to change diffusion driving force in TOUGH2 from the mass fraction gradient times the phase density to the density gradient of the diffusing component. If the phase density is constant, these two methods give the same result. However, we also found that if a high intrinsic gas permeability was used numerical instability in water saturation did not occur. It is known from numerous laboratory and field experiments that intrinsic permeability to gas flow can be high, and a difference of about six order of magnitude between intrinsic gas and water permeability has been observed (Olivella and Gens, 2000). In TOUGH2 we simulated this high gas permeability through the Klinkenberg parameter according to:

$$K_g = K_l\left(1 + b/P\right) \quad (2\text{-}7)$$

where K_g is intrinsic permeability for gas flow, K_l is intrinsic permeability for water flow, b is the Klinkenberg parameter, and P is pressure. In this case we assigned a high value, 2.5×10^{11} $Pa^{-1,}$ for the Klinkenberg parameter. For a near atmospheric pressure, i.e. 0.1×10^6 Pa as assumed initially in the buffer, b/P would be 2.5×10^6, that is, intrinsic permeability for gas flow would be about 6 orders of magnitude higher than the intrinsic permeability for water flow.

2.7.3 TOUGH2 TH benchmark simulation results

TOUGH2 simulation results are given in Figures 2-17, 2-18, and 2-19 for temperature, water saturation, and pore-water pressure, respectively. The waste package-buffer interface is at x = 0.525 m, the buffer-shotcrete interface is at x = 1.35 m, shotcrete-rock interface is at 1.5 m, and the far boundary is at 30 m. Time histories are given in Figure 2-20 for water saturation and temperature at the heater (r = 0.525 m) and near the outer edge of the buffer (r = 1.275 m). The simulation results show that the buffer remains dry near the heater whereas water infiltrates from the rock and saturates the buffer near its interface with the rock. The temperature increases substantially near the heater with a peak temperature exceeding 200°C. Note, though, that the temperature will be overestimated compared to what will be expected in the field because of the simplified 1D model geometry and the assumed heat load.

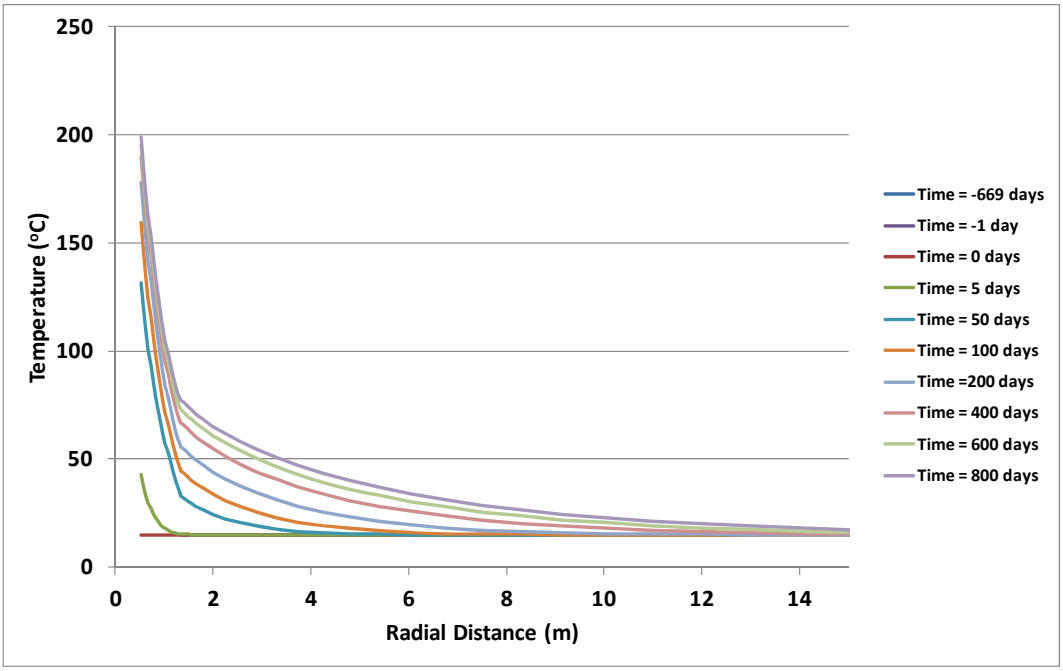

Figure 2-17. Temperature profiles.

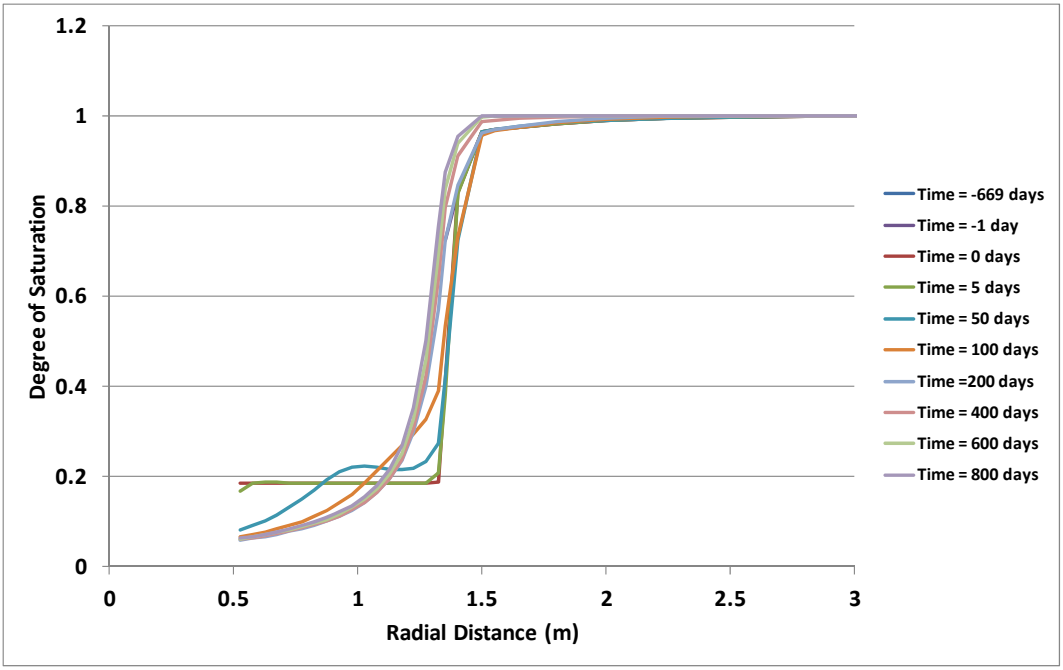

Figure 2-18. Degree of saturation profiles.

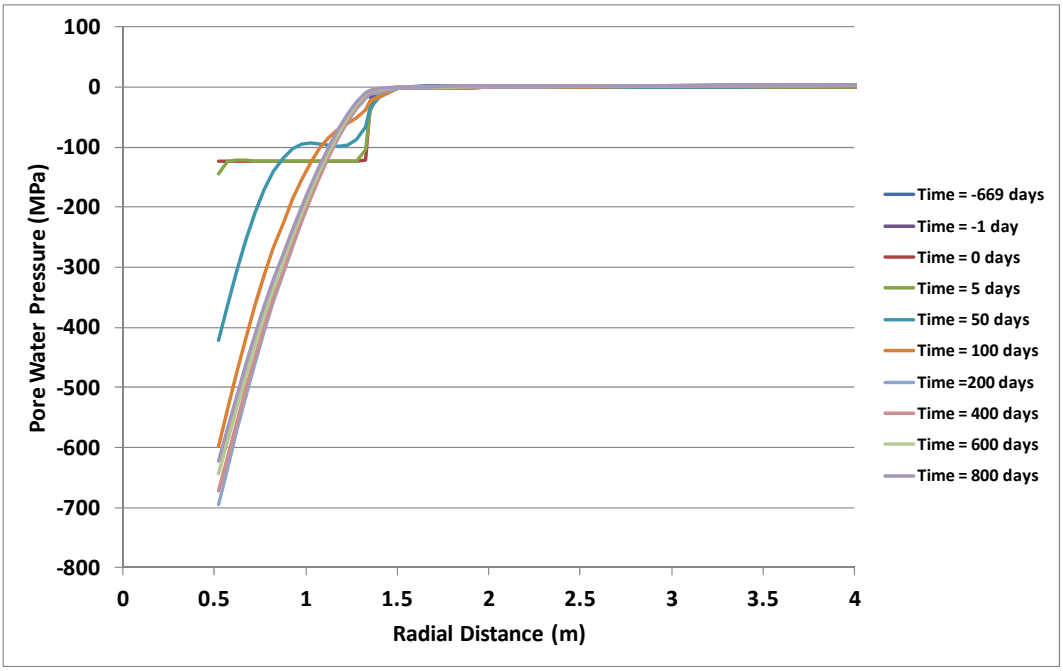

Figure 2-19. Water pressure profiles.

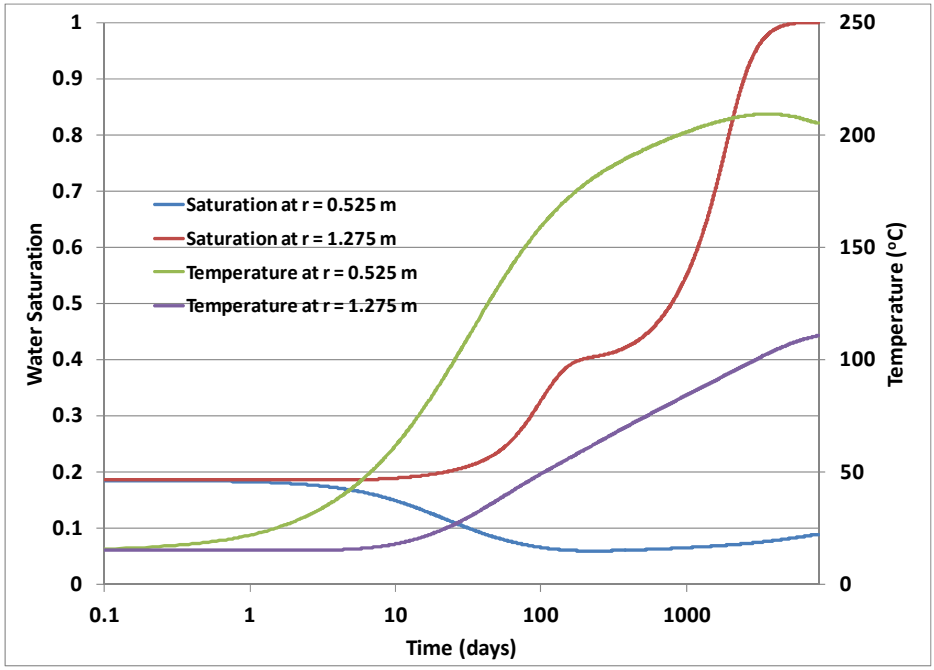

Figure 2-20. Time histories for saturation and temperature at two locations in the buffer.

2.7.4 TOUGH-FLAC THM benchmark simulation results

We conducted an initial THM model simulation of the benchmark example using TOUGH-FLAC. The THM simulation was conducted over the same modeling stages including tunnel excavation, shotcrete projection, canister and bentonite placement and heating induced by the nuclear waste. In this case we make use of axisymmetry and model only 10º of the cylinder for the FLAC3D part of the TOUGH-FLAC model. The mechanical properties used in the THM model are summarized in Table 2-6. From recent experiments conducted on laboratory samples of MX-80 granular bentonite, the swelling stress developed when going from about 18.5% to 100% liquid saturation is about 7 MPa (Rizzi et al., 2011). In this model simulation, and as defined in the benchmark, a simple elastic model is used to simulate the mechanical behavior of the bentonite with a Young's modulus fixed at 300 MPa. We used a linear elastic swelling model (Rutqvist et al., 2011), in which the volumetric swelling and the swelling stress depends on the changes in water saturation, ΔS_l, according to:

$$\Delta\sigma'_{sw} = 3K\Delta\varepsilon_{sw} = K\Delta S_l \beta_{sw} \tag{2-8}$$

where $\Delta\sigma'_{sw}$ is the induced swelling stress (an effective stress), K is the bulk modulus, and β_{sw} is a model input parameters can be determined analytically to achieve a desired maximum swelling stress of 7 MPa. For the given Young's modulus and Poisson's ratio the bulk modulus would be 200 MPa, and then the appropriate moisture swelling coefficient can be calculated using Equation (2-9) as:

$$\beta_{sw} = \frac{\Delta\sigma'_{sw}}{3K\Delta S_l} = \frac{7\cdot 10^6}{3\cdot 200\cdot 10^6\cdot(1.0-0.185)} = 0.0143 \tag{2-9}$$

The results of stress profiles are shown in Figure 2-21. The highest stress occurs in the shotcrete as longitudinal and tangential stress with maximums of 75 and 40 MPa, respectively. These are thermal stresses as these can be very high as a result of the relatively high Young's modulus and high thermal expansion coefficient in the shotcrete. The tangential and longitudinal stresses in the Opalinus Clay peak at about 25 to 30 MPa just outside the shotcrete and is also a result of thermally induced stress. In the bentonite buffer, the stress is less than 2 MPa and is affected by both thermally induced stress and moisture swelling induced stress. Tangential and longitudinal stress is low near the heater due to drying shrinkage in that area, whereas it is higher near the interface of the buffer with the shotcrete. However, overall the buffer stays quite dry throughout the 800 days of simulations and therefore the stress in the buffer is relatively low till the end of the simulation.

Table 2-6. FLAC3D Mechanical parameters for FE 1-D benchmark.

	Overpack	Buffer	Shotcrete	Rock
Young's modulus (MPa)	$200\text{x}10^3$	300	$30\text{x}10^3$	$6\text{x}10^3$
Poisson ratio (-)	0.3	0.25	0.25	0.25
Thermal expansion coefficient (ºC^{-1})	$1.5\text{x}10^{-5}$	$1.5\text{x}10^{-5}$	$3.5\text{x}10^{-5}$	$3.5\text{x}10^{-5}$
Swelling coefficient	0	0.0143	0	0

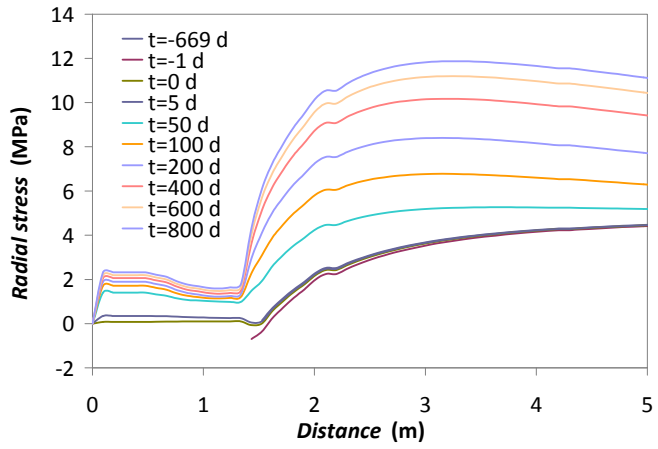

(a)

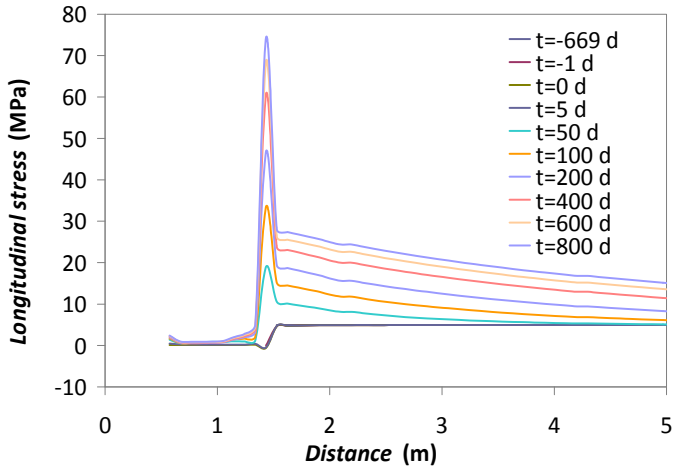

(b)

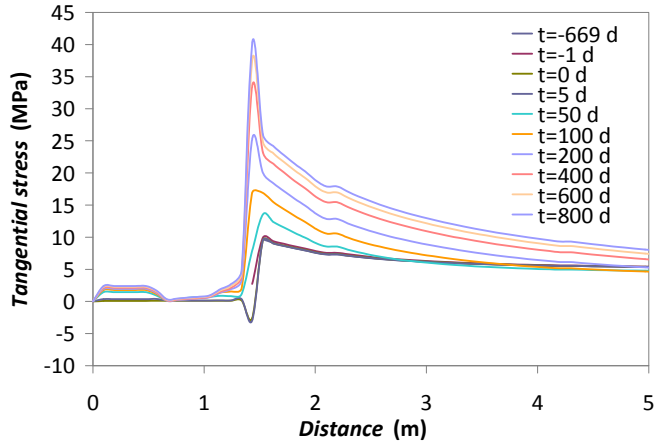

(c)

Figure 2-21. Profiles of (a) radial, (b) longitudinal, and (c) tangential stress.

2.8 Initial 3D TH model prediction of peak temperature

In this section we present an initial model prediction of temperature evolution during the FE Experiment using the current best estimate of TH properties. These properties are equivalent to those given in the benchmark definition. With regard to predicting the peak temperature, some of the most significant differences compared to the scoping calculation in Section 2.4 is the properties are the thermal conductivity of the buffer and the Opalinus Clay as well as water diffusivity. The results of the 3D TOUGH2 simulation are presented in Figure 2-22. The most striking result is that the peak temperature at the buffer now is about 160°C, i.e., considerably higher than the targeted 125 to 135°C. The temperature at the outer edge of the buffer is up from 68 to 74°C, which is a result of the slightly lower thermal conductivity of the host rock in this case. The substantially higher peak temperature at the canister surface is caused by the combined effects of lower thermal conductivity of the buffer and the rock as well as the high diffusion coefficient that keep the buffer dry around the heater. We consider this an initial predictive modeling result as there are still uncertainties related to the thermal conductivity and diffusion coefficient to be applied for this type of bentonite material.

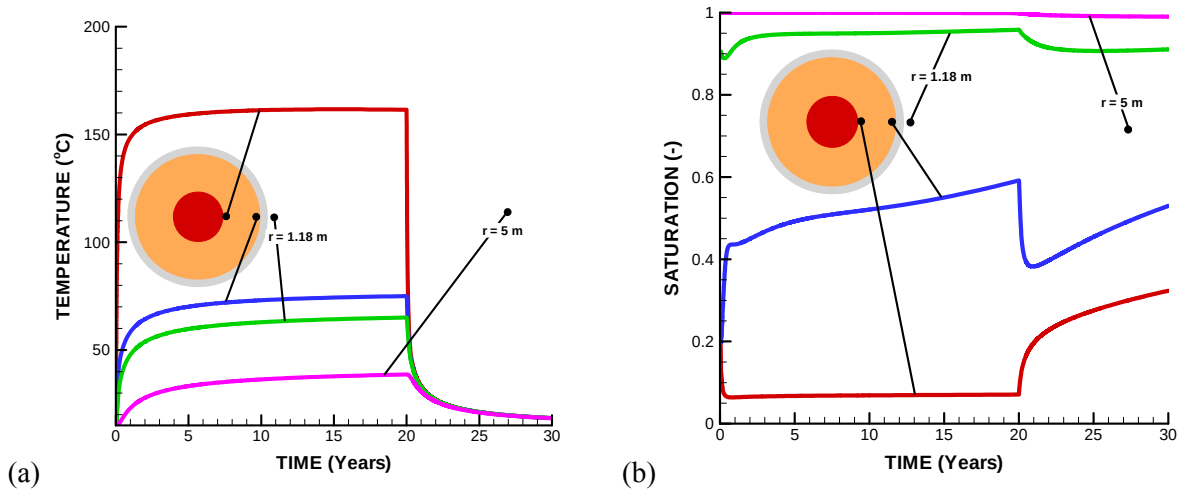

Figure 2-22. Initial model prediction using parameters defined in the benchmark simulation: (a) temperature and (b) liquid saturation.

3. HG-A test

The HG-A test is being conducted in the Opalinus Clay at the Mont Terri underground research laboratory (URL) near Saint-Ursanne, Switzerland. The HG-A test is intended to provide data on the geomechanical and hydrogeologic effects of the excavation damage zone (EDZ). The test is specifically targeted to observe how fluids injected into a test section sealed by a packer penetrate both into the rock and within the EDZ (Marschall et al., 2006).

In this section, we describe the test, discuss some of the test attributes and observations, apply an analytical model for rock failure around the tunnel, and then use a coupled hydro-mechanical fracture damage model, TOUGH-RBSN, to investigate the development of fractures around the tunnel in greater detail. The development of the TOUGH-RBSN model is documented in Liu et al. (2013). The goal of this activity is to use the Mont Terri test data to help build confidence in the TOUGH-RBSN model for predicting various facets of fracture development and evolution within the EDZ.

3.1 Location and description of the HG-A microtunnel test

Figure 3-1 shows the general location of the HG-A test within the Mont Terri URL. This test is being conducted in a 13-m long, 1 m diameter microtunnel located off Gallery 04. The tunnel was excavated in February 2005 over a period of about 3 weeks. Steel liner was installed in the first 6 m, and the mid-section where the packer is installed was coated with an epoxy resin (Meier et al., 2005). The test section is supported by a wire mesh and is backfilled with sand. A retaining wall to hold the gravel backfill is grouted in place between the packer and the test section (Lanyon et al., 2009). Finally, the packer seals the test section from the front end of the microtunnel and Gallery 04.

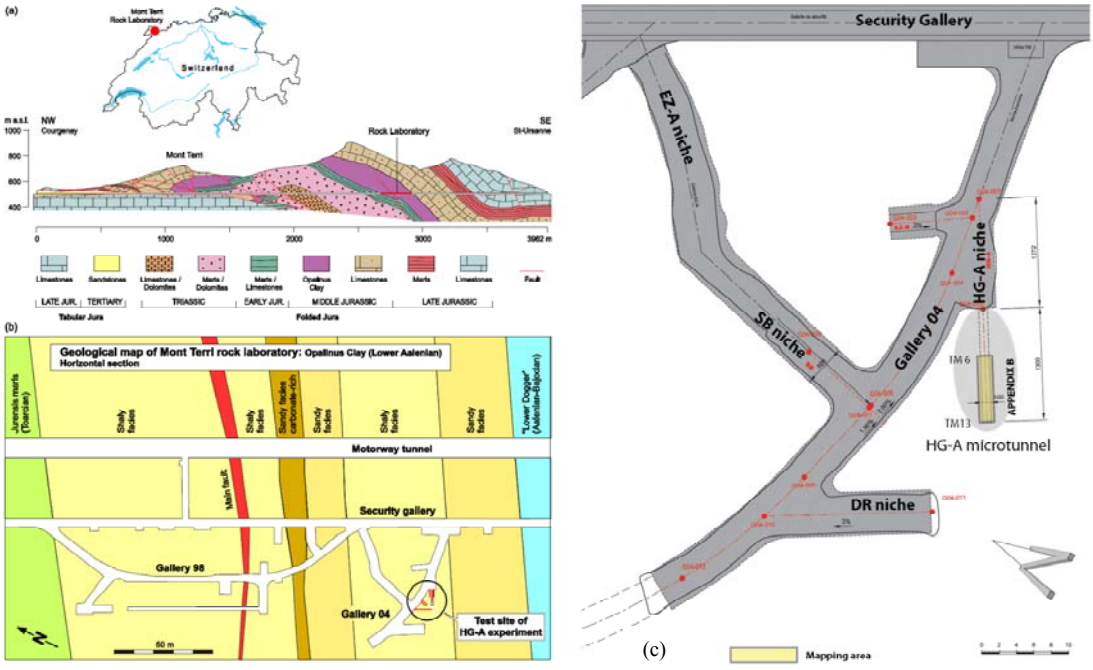

Figure 3-1. The Mont Terri underground rock laboratory: (a) geological profile of the site after Freivogel and Huggenberger (2003), (b) site map showing the underground facilities of the laboratory. The HG-A microtunnel is located in the New Gallery 04. (source: Marschall et al., 2006), (c) map view of the HG-A microtunnel and adjacent excavations; structural map of tunnel surface shown in Figure 3-3 is the area highlighted in yellow (source: Nussbaum and Bossart, 2006).

The HG-A test configuration is shown in Figure 3-2. Instrumented boreholes emanate from the nearby gallery and from the face of the HG-A niche into the rock surrounding the tunnel. The instrumentation outside the tunnel includes piezometers for monitoring water pressure, stressmeters for rock stress, and chain deflectometers for deflection of tunnel axis. The region inside and adjacent to the tunnel is instrumented with piezometers, total pressure cells along the packer for radial stress, time-domain reflectometers for water saturation, strain gauges measuring tangential movement, and extensometers for radial movement. The locations of some of these instruments are shown in Figure 3-2.

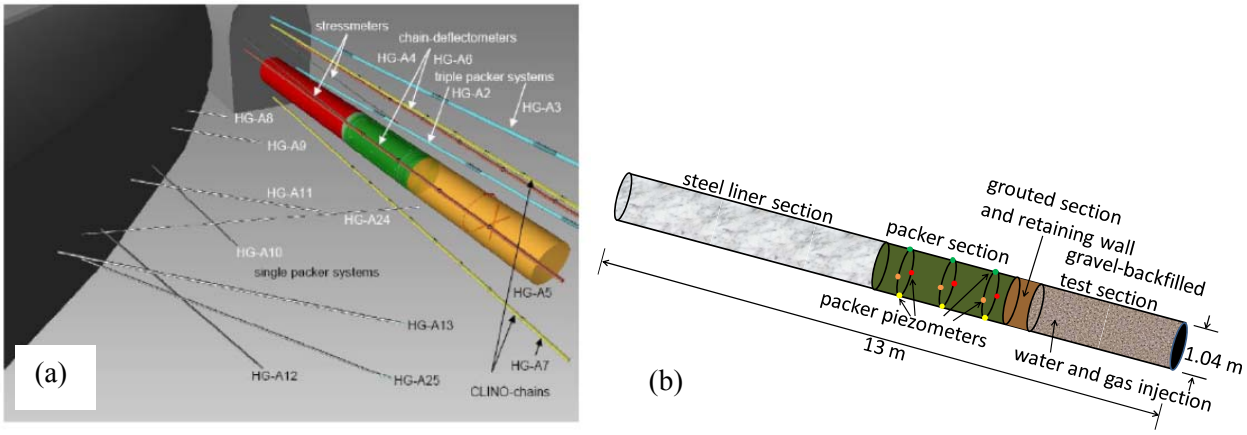

Figure 3-2. HG-A test configuration: (a) schematic drawing of the microtunnel and the site instrumentation. Color coding refers to the steel liner (red), the packer seat (green) and the backfilled test section (orange) (source: Marschall et al., 2008); (b) detail of tunnel showing packer piezometers and test section for fluid injection.

3.2 Observations of rock features, EDZ damage, and tunnel convergence

The HG-A microtunnel was mapped to identify natural structural features and any induced fracturing or damage. The tunnel map is shown in Figure 3-3. The natural features include bedding planes and tectonic-related fractures and faults. The rock is relatively homogeneous on the meter scale but pronounced bedding was mapped at finer scales (Marschall et al., 2006). The rock is highly fractured with fracture frequencies ranging from 0.3 to 1 m, although fracture permeability is not significant indicating that fractures are mainly closed under natural stress conditions (Marschall et al., 2006; 2008). There are two main fault orientations: (1) an SSE-dipping system subparallel to the bedding planes and (2) a low-angle S to SW dipping system. The microtunnel is oriented along the bedding strike, and the bedding planes dip at 48° SSE, such that the bedding planes are tangent to the tunnel surface at about 3 to 5 o'clock and 9 to 11 o'clock (see also Figure 3-4) (Marschall et al., 2006).

Extensional and shear brittle fracturing, tunnel wall breakouts, and reactivation of bedding and fault planes are features related to the excavation damage zone. These features are mapped in Figure 3-3 and can be seen to be quite non-uniform around the tunnel.

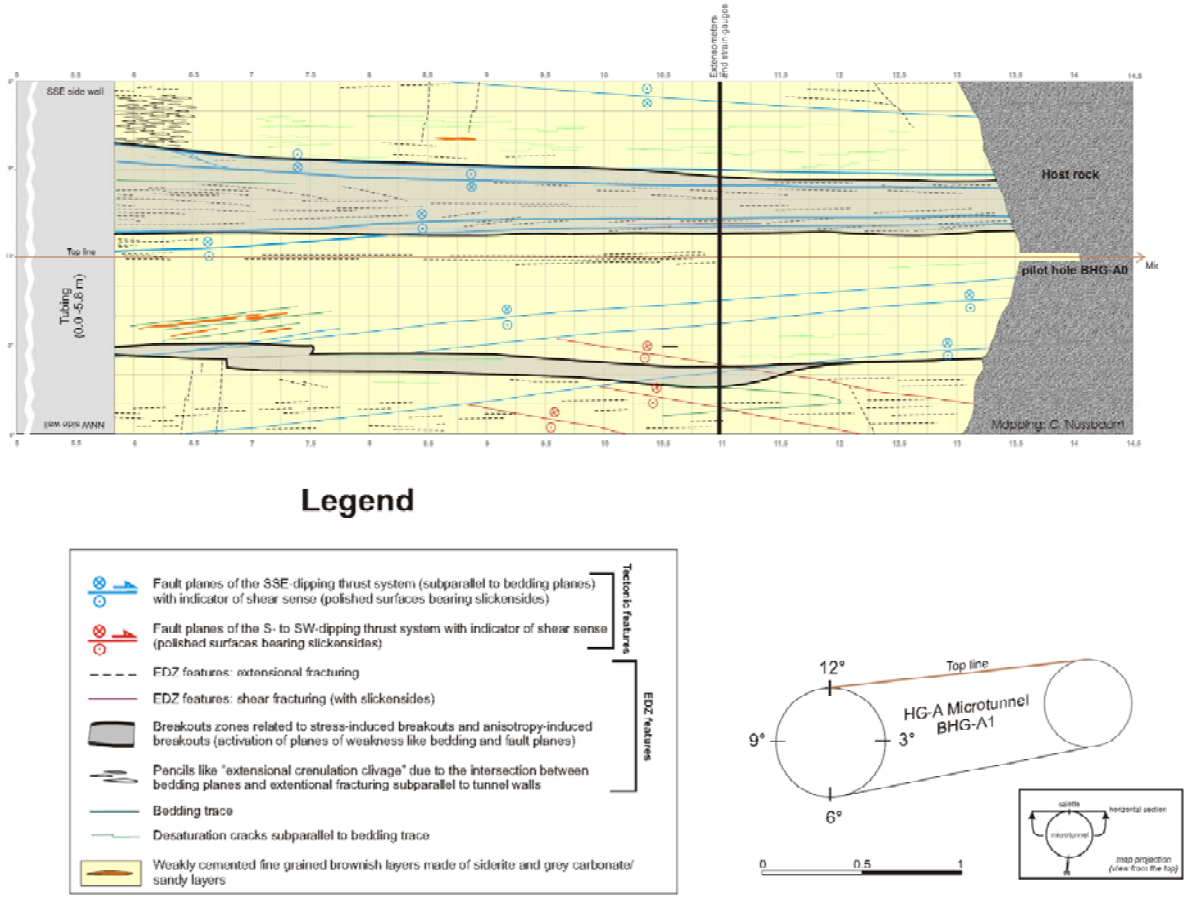

Figure 3-3. Structural Mapping of the HG-A microtunnel (source: Nussbaum and Bossart, 2006)

Excavation resulted in some visible damage along the microtunnel walls as shown in Figure 3-4(a). A conceptual model for the occurrence of damage is given in Figure 3-4(b), which attributes most of the damage to anisotropic strength characteristics of the rock and anisotropic stresses. Rock strength is found to be a function of orientation relative to the bedding (Bock, 2001). The damage is not uniform around the tunnel as shown above, a result of the relative weakness of the rock orthogonal to the bedding planes and as a result of weakness near faults intercepting the tunnel.

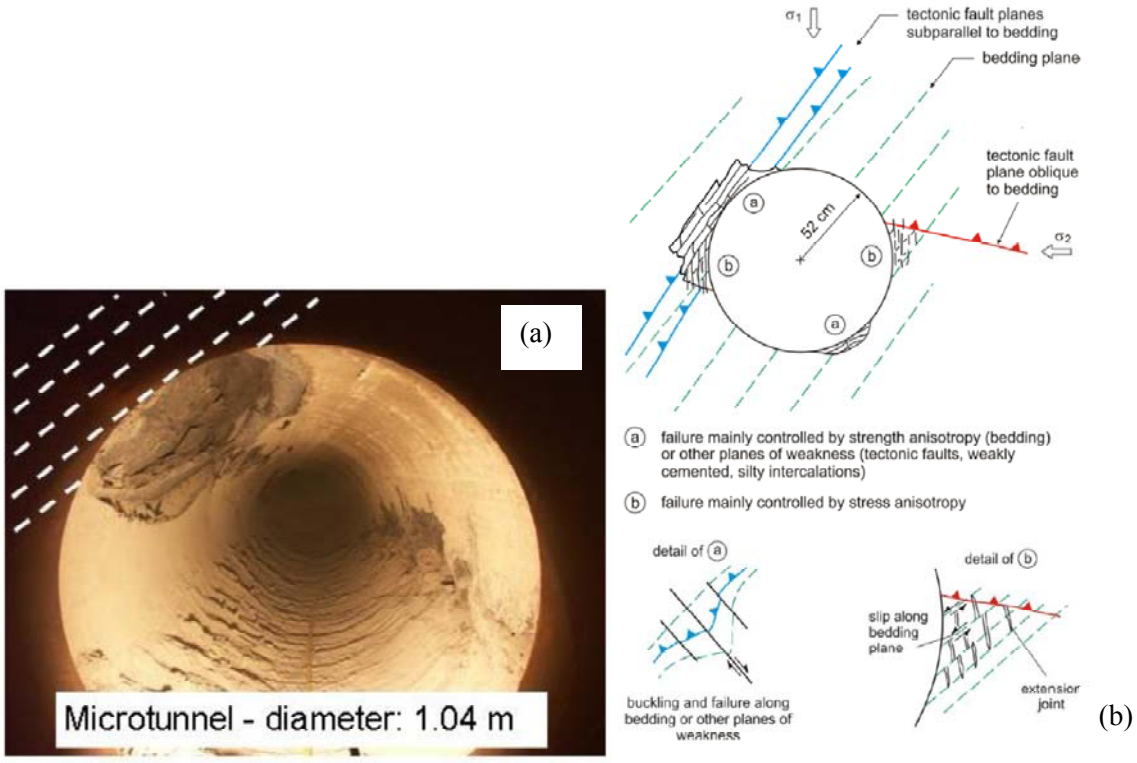

Figure 3-4. Excavation damage. (a) Breakouts along microtunnel walls, with an orientation looking from the HG-A Niche towards back end of microtunnel (source: Marschall et al., 2006); (b) Conceptual diagram of the damage zone with the same orientation as in (a). (source: Lanyon et al., 2009; Marschall et al., 2006)

Horizontal and vertical extensometers in the test section of the tunnel (at about 11 m from the tunnel entrance) provide data on the rate of tunnel convergence. Figure 3-5 shows the horizontal and vertical convergence rates. Over a five-year period, the tunnel diameter decreased about 3 mm in the horizontal direction and about 0.3 mm in the vertical direction. Most of the horizontal convergence occurred during the first year, whereas the slower vertical convergence continued over the entire 5 years. Shorter-term variations in convergence are also seen. These are in response to changes in the megapacker pressure and fluid injection (Lanyon et al., 2009) discussed in the next section.

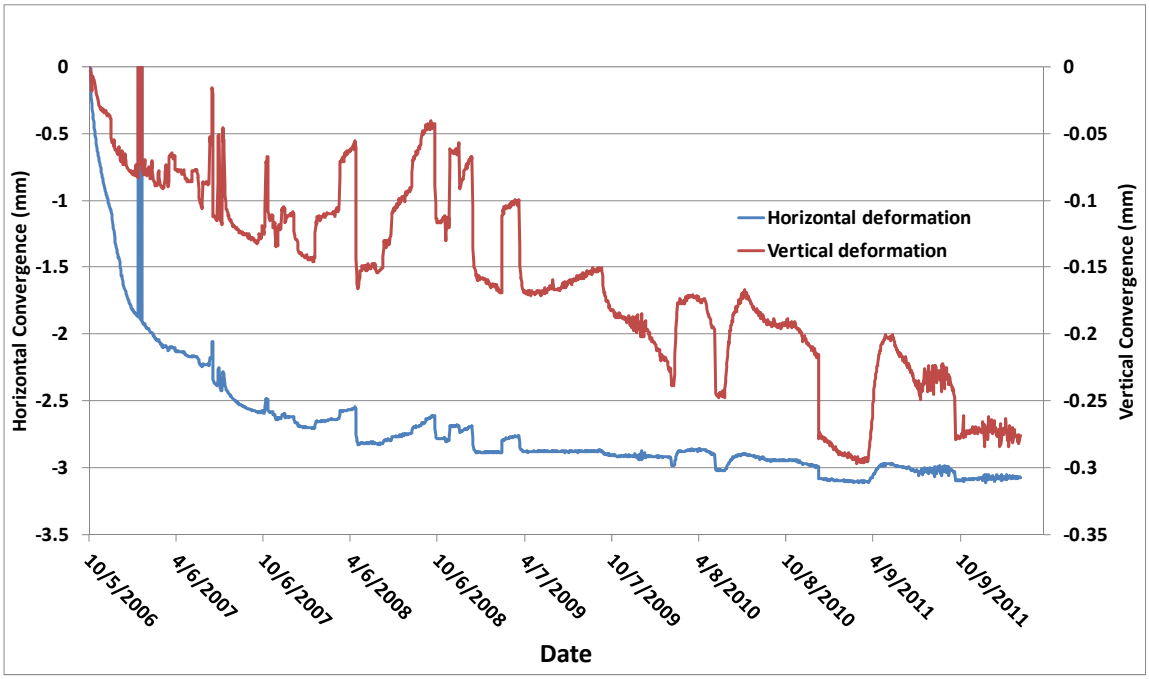

Figure 3-5. Tunnel convergence over a 5-year period.

Figure 3-6 plots convergence over the last 2.5 years with the horizontal and vertical axes at the same scale. The figure shows that for this time period, convergence in the horizontal and vertical directions have been similar, about -0.05 to -0.08 mm/year.

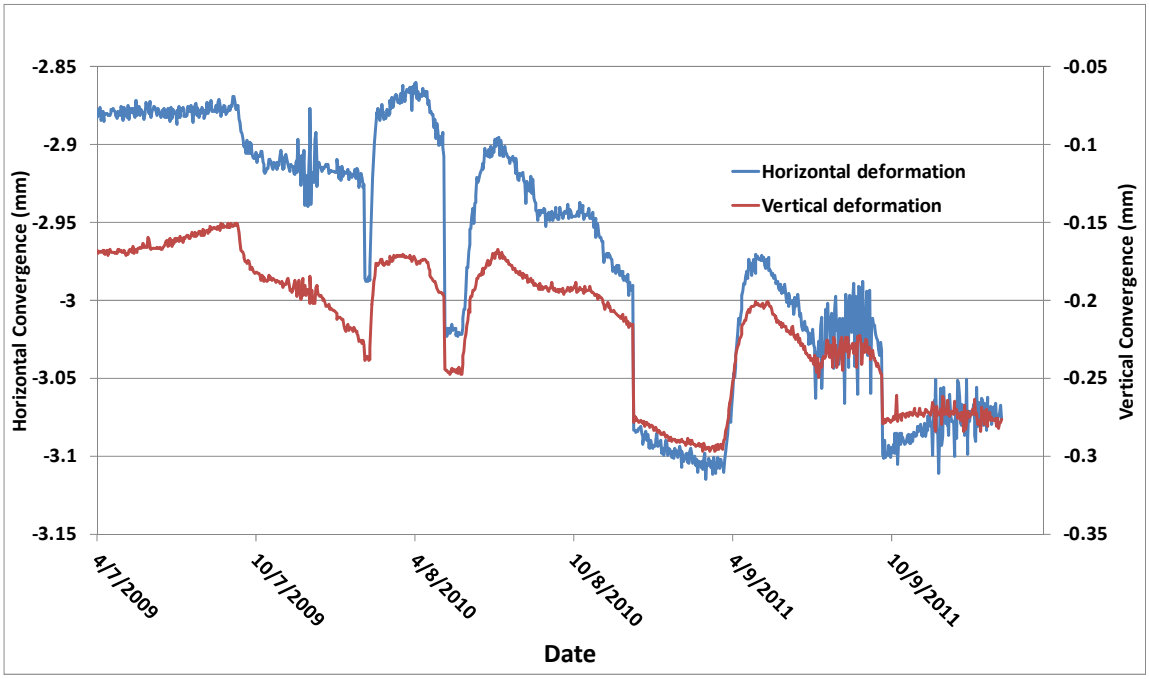

Figure 3-6. Tunnel convergence over the last 2.5 years.

3.3 Water and gas injection testing

Water was injected into the test section at a variety of rates from 2007 to February 2010, followed by three periods of gas injection until September 2011. Pressure signals from piezometers along the packer (see Figure 3-2(b)) are shown in Figure 3-7. Figure 3-7(a) is for the piezometer ring furthest from the test section, Figure 3-7(c) is for the piezometer ring nearest to the test section, and Figure 3-7(b) is for the intermediate piezometer ring. As can be seen, pressure response is most vigorous and ubiquitous in Figure 3-7(c); moving away from the test section, pressure response dies out in several locations in Figures 3-7(b) and 3-7(a). However, the "3 o'clock position" still shows significant pressure response to the injected fluid pressure in the test section, signifying a high-permeability connection several meters from the packer. The testing has also shown indirect evidence of fracture self-sealing, where injection rate and/or pressure behavior is consistent with an increasing resistance to fluid injection into the test section. The increased resistance to injected fluids, presumably in the EDZ fractures, is identified by the sealing index, S, introduced by Lanyon et al. (2009), where $S = \frac{Q}{P-100}$ and Q is the flow rate (mL/min) and P is the pressure in (kPa), with self-sealing indicated by S decreasing with time, as shown in Figure 3-8.

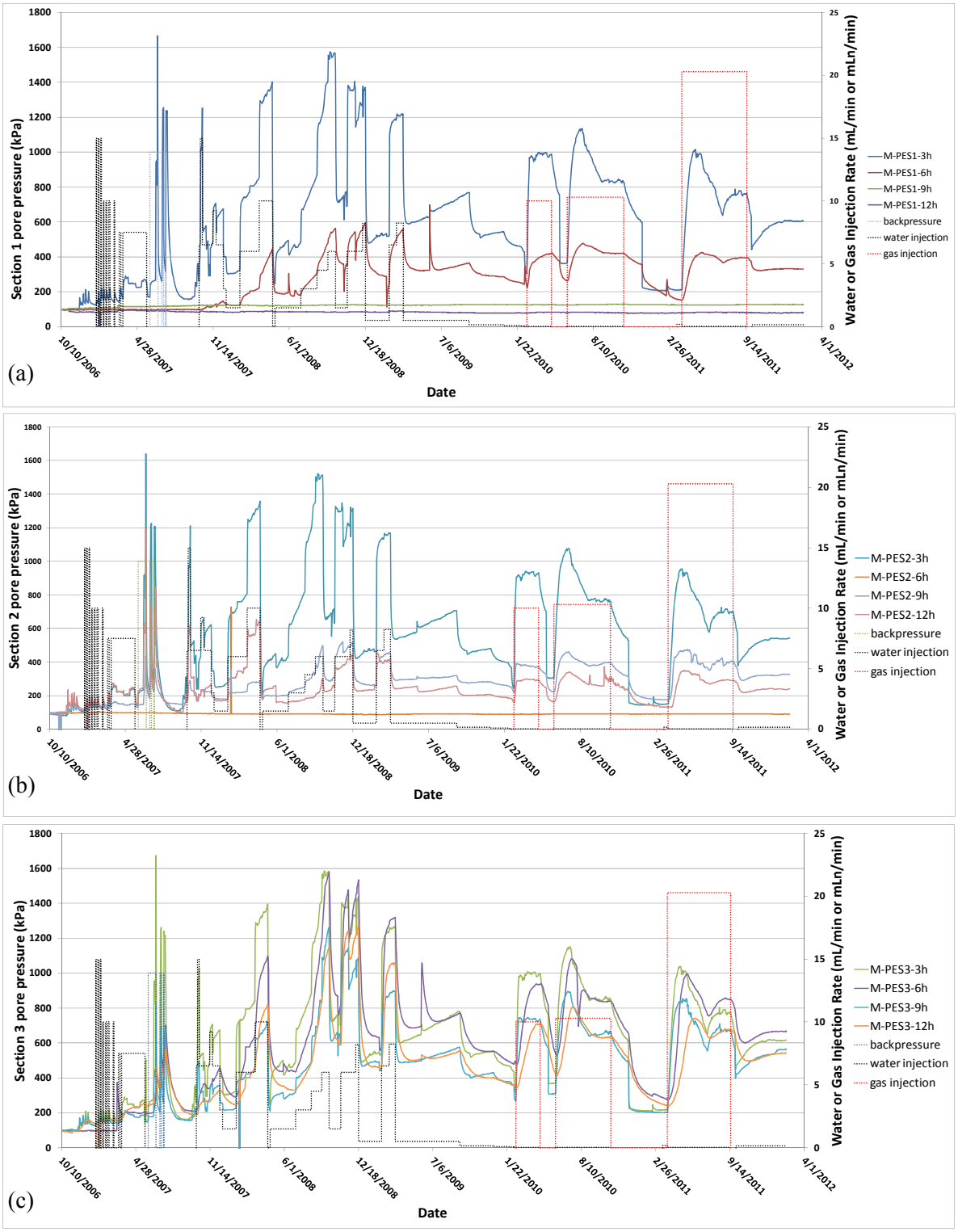

Figure 3-7. Fluid pressure response along packer section; (a) piezometer ring furthest from test section; (b) intermediate piezometer ring; (c) piezometer ring nearest to test section.

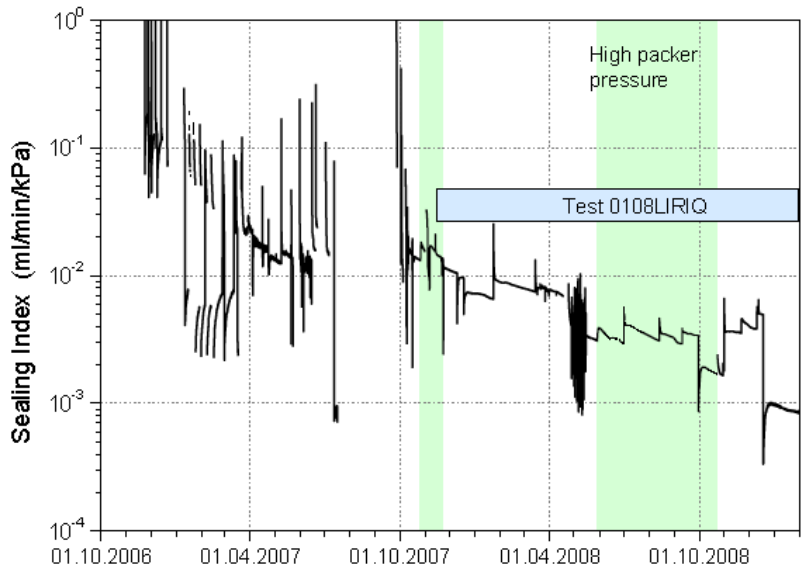

Figure 3-8. Sealing index as a function of time over a 2-year period. (source: Lanyon et al., 2009)

Packer pressure was also varied during the test over a range of 1 to 3 MPa. The effects of packer pressure on EDZ appeared to be consistent with the idea that fracture permeability decreased with increased packer pressure (Lanyon et al., 2009).

3.4 Initial analysis of rock failure along the drift wall

An initial analysis has been performed to investigate failure mechanisms along the tunnel wall. Failure is computed by first computing the stress around an open drift using an analytical solution for this problem derived by Kirsch (1898). The Kirsch solution is limited to a homogeneous rock mass, therefore, the effects of faults are not included. The solution also requires that the rock be treated as isotropic in terms of the elasticity parameters, Young's modulus and Poisson's ratio, but can accommodate anisotropic stress conditions at the far boundaries. The elasticity parameters for the Opalinus Clay are known to be anisotropic for measurements parallel and orthogonal to bedding (Bock, 2001). However, the assumption that these parameters are isotropic does not significantly impact the computed stress field around the tunnel if the far field can be treated as a constant stress boundary (Tonon and Amadei, 2003). It should be pointed out that displacements in response to the stress field are not accurately predicted using isotropic elastic parameters (Tonon and Amadei, 2003), but the present analysis is not evaluating displacements. Once the stress field is known, the anisotropic rock strength parameters may be used to evaluate whether tensile or shear failure is expected. Tensile failure is simply evaluated by comparing the effective normal stresses with the corresponding tensile strength. Shear failure is evaluated using a Mohr-Coulomb failure approach.

The solution for the mechanical stress, σ_{rr}^{m}, $\sigma_{\theta\theta}^{m}$, and $\sigma_{r\theta}^{m}$ is given by Pollard and Fletcher (2005, p. 236):

$$\sigma_{rr}^{m} = \left(1 - \frac{a^2}{r^2}\right)\left(\frac{\sigma_h + \sigma_H}{2}\right) - \left(1 - 4\frac{a^2}{r^2} + 3\frac{a^4}{r^4}\right)\left(\frac{\sigma_h - \sigma_H}{2}\right)\cos(2\theta) \tag{3-1}$$

$$\sigma_{\theta\theta}^{m} = \left(1 + \frac{a^2}{r^2}\right)\left(\frac{\sigma_h + \sigma_H}{2}\right) + \left(1 + 3\frac{a^4}{r^4}\right)\left(\frac{\sigma_h - \sigma_H}{2}\right)\cos(2\theta) \tag{3-2}$$

$$\sigma_{r\theta}^{m} = \left(1 + 2\frac{a^2}{r^2} - 3\frac{a^4}{r^4}\right)\left(\frac{\sigma_h - \sigma_H}{2}\right)\sin(2\theta) \tag{3-3}$$

where r is the radial coordinate (radially outward positive), θ is the angular coordinate (counterclockwise positive), a is the tunnel radius, p is the fluid pressure, σ_H is the minimum far-field stress (which is horizontal in this case), and σ_h is the maximum far-field stress (which is vertical in this case) (Figure 3-9). The stresses are defined here such that compression is positive.

The effective stresses accounting for fluid pore pressure are:

$$\sigma_{rr}^{e} = \sigma_{rr}^{m} - p \tag{3-4}$$

$$\sigma_{\theta\theta}^{e} = \sigma_{\theta\theta}^{m} - p \tag{3-5}$$

$$\sigma_{r\theta}^{e} = \sigma_{r\theta}^{m} \tag{3-6}$$

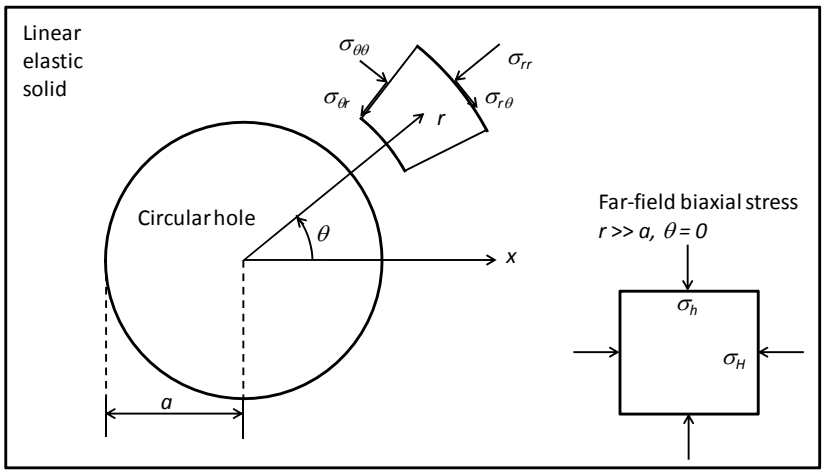

Figure 3-9. Definition diagram for plane stress around a circular hole.

First consider damage at the tunnel wall, where $r = a$. The stress Equations (3-1) through (3-3) simplify to:

$$\sigma_{rr}^{e} = -p \tag{3-7}$$

$$\sigma_{\theta\theta}^{e} = (\sigma_h + \sigma_H) + 2(\sigma_h - \sigma_H)\cos(2\theta) - p \tag{3-8}$$

$$\sigma_{r\theta}^{e} = 0 \tag{3-9}$$

Tensile failure occurs if either of the effective normal stresses fall below the negative of the tensile strength, $-T_r(\theta)$ in the radial direction, and $-T_\theta(\theta)$ in the circumferential direction, because of the anisotropic nature of the Opalinus Clay rock strength:

$$\sigma_{rr}^{e} = -p < -T_r(\theta) \tag{3-10}$$

$$\sigma_{\theta\theta}^{e} = (\sigma_h + \sigma_H) + 2(\sigma_h - \sigma_H)\cos(2\theta) - p < -T_\theta(\theta) \tag{3-11}$$

Shear failure occurs if the stress state of the system touches the Mohr-Coulomb failure curve,

$$\tau_m \geq \sigma_m \sin(\phi) + c(\theta)\cos(\phi) \tag{3-12}$$

where

$$\tau_m = \frac{|\sigma_{rr} - \sigma_{\theta\theta}|}{2} \tag{3-13}$$

And

$$\sigma_m = \frac{\sigma_{rr} + \sigma_{\theta\theta}}{2}. \tag{3-14}$$

The cohesive strength, $c(\theta)$, is also a function of angle because of the anisotropic nature of the Opalinus Clay rock strength, and the friction angle, ϕ.

Far-field, natural, stress conditions in the Opalinus Clay are approximated by $\sigma_h = 6.5$ MPa and $\sigma_H = 4.5$ MPa, and pore pressure is approximated by, $p = 1.5$ MPa (Martin and Lanyon, 2003, p. 1085 and 1087). Tensile strength is characterized by values parallel and normal to bedding, $T_p = 2$ MPa and $T_n = 1$ MPa, respectively (Bossart, 2012, Annex 4-21). Similarly, cohesive strength is also characterized by values parallel and normal to bedding, $c_p = 5.5$ MPa and $c_n = 2.2$ MPa (Bossart, 2012, Annex 4-22). The friction angle ranges from 24° to 26° is adequately characterized by the value 25° (Bossart, 2012, Annex 4-22).

The radial tensile strength is represented as a function of angle through the following:

$$T_r(\theta) = T_p \cos^2(\theta - \theta_b) + T_n \sin^2(\theta - \theta_b) \tag{3-15}$$

where θ_b is the angle of the bedding, previously identified to be 48°. The circumferential tensile strength is given by

$$T_\theta(\theta) = T_p \sin^2(\theta - \theta_b) + T_n \cos^2(\theta - \theta_b) \tag{3-16}$$

The cohesive strength is given by

$$c(\theta) = c_p \cos^2(\theta - \theta_b) + c_n \sin^2(\theta - \theta_b) \tag{3-17}$$

Calculations done for effective stress and the negative of tensile strength around a tunnel are shown in Figure 3-7. When radial or circumferential stress falls below the negative of tensile strength, tensile failure occurs. As seen in Figure 3-10, tensile failure only occurs for some positions in the radial direction.

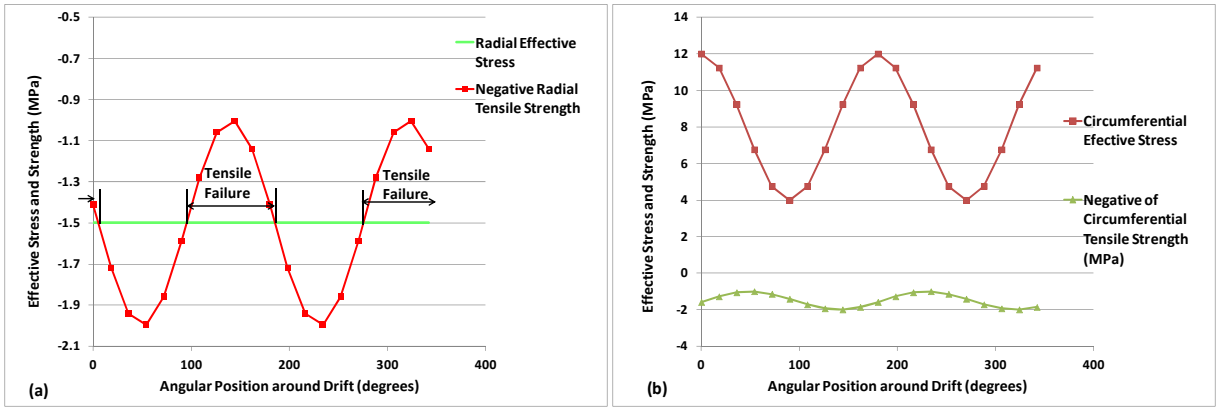

Figure 3-10. Comparison of effective stress and tensile strength to identify tensile failure: (a) radial direction; (b) circumferential direction.

Calculations for shear failure using Equation (3-12) are shown in Figure 3-11. When the ordinate in Figure 3-11 exceeds zero, shear failure occurs.

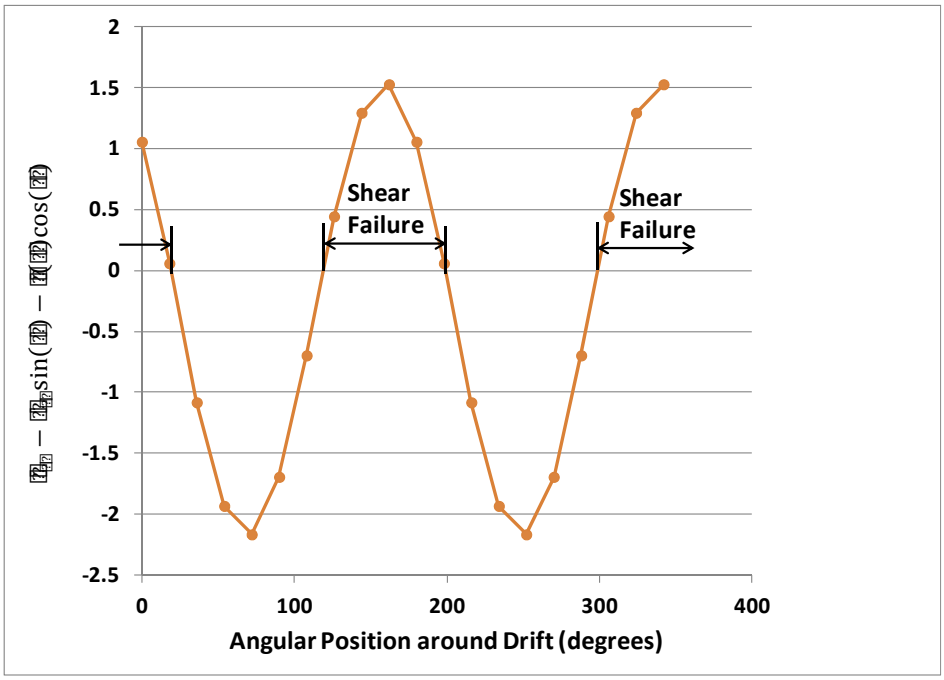

Figure 3-11. Results for shear failure.

The failure analyses results are summarized in Figure 3-12. This shows that both shear and tensile failure occur along the NNW side of the drift wall roughly between 3 and 5 o'clock, with shear failure only at 2:30 o'clock and tensile failure at 5:30 o'clock. Along the SSE side, both shear and tensile failure occur roughly between 9 and 11 o'clock, with shear failure at 8:30 o'clock and tensile failure at 11:30 o'clock. This is in qualitative agreement with the observations of failure, although the observed failure (Figure 3-3), especially on the NNW side, is restricted to a narrower region than predicted here.

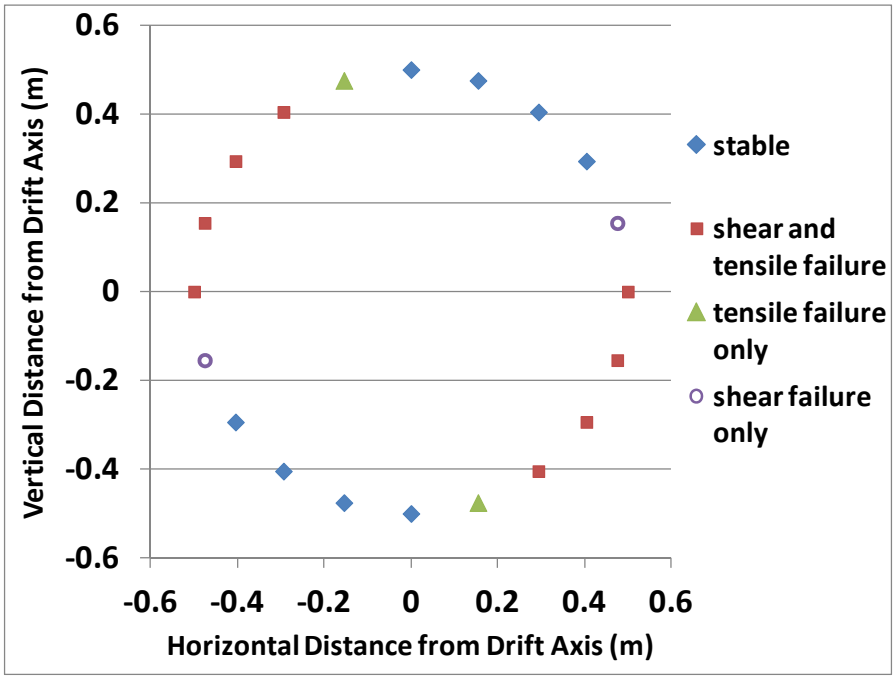

Figure 3-12. Results for failure analysis, with an orientation looking from the HG-A Niche towards the back end of microtunnel.

Failure analysis at radii greater than 0.5 m (the radius of the drift) suggests that damage is confined to a narrow region around the drift. Tensile failure is found to be limited to only 3 to 4 cm into the drift wall, while shear failure is limited to about 10 cm into the drift wall.

The analysis can be extended to determine the extent of rock failure into the drift wall. The results are shown in Figure 3-13, which indicates that damage lies within 0.1 m of the drift wall. The other observation is that the failure mode changes from "shear and tensile failure" at a number of locations along the drift wall to "shear failure only" as the radial coordinate increases. At radial distances less than 0.1 m from the drift wall, the rock condition becomes "stable" at all orientations. This analysis demonstrates that shear failure may be expected to play an important role in the development of fractures in the EDZ.

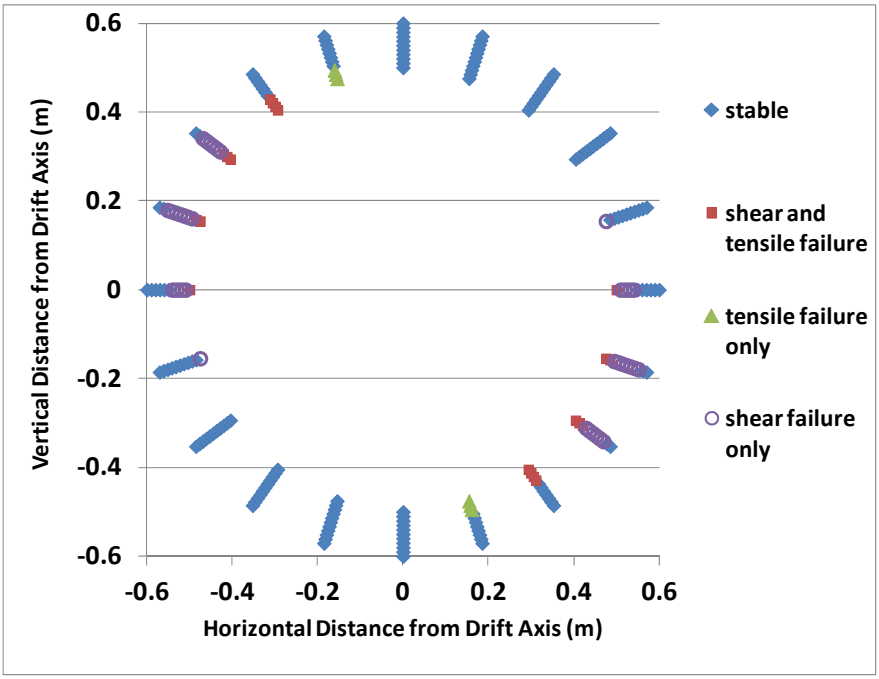

Figure 3-13. Results for failure analysis as a function of depth into the drift wall, with an orientation looking from the HG-A Niche towards back end of microtunnel.

3.5 Implementation of RBSN for modeling the HG-A test

This section presents work to date on the implementation of RBSN to model the HG-A test. The initial focus of the work is not on the injecting testing, which requires a three-dimensional model, but to first look at geomechanical behavior including fracture development in the EDZ with a two-dimensional model. The problem has been further simplified for the present analysis by assuming a constant uniform pore pressure such that the geomechanical and fracture damage calculations may be performed using RBSN as a stand-alone model, i.e., without coupling to TOUGH2 for hydrogeologic processes. This approximation is accurate up until rock failure leads to fracturing and a rapid loss of pore pressure (Liu et al., 2013).

Previous applications of the RBSN model have mainly focused on fracturing under tensile stress conditions. However, as discussed in Section 3.4, shear failure under compressive stress conditions also plays an important role in the development of fractures in the EDZ for the for the HG-A test. This section presents the development and testing of compressive behavior and failure using the RBSN model.

3.5.1 Background and model formulation

Discrete models have become popular as computational tools for studying the heterogeneous characteristics of geomaterials. This category includes the Rigid-Body-Spring network (RBSN), in which system behavior is represented by primitive two-node elements interconnected on a set of nodal points. The approach considered here is based on the Rigid-Body-Spring concept of Kawai (1978). To provide a basic understanding of this modeling approach, an overview is given here. Details regarding the RBSN are given elsewhere (Bolander and Saito, 1998; Asahina et al., 2011).

Geometry of the RBSN is defined by the dual Delaunay tessellation of the nodal points. The basic unit of RBSN is a 1D lattice element consisting of a zero-size spring set located at the centroid of the Voronoi

boundary (Fig. 3-14). Each node has six degrees of freedom for the 3D case. The spring set is formed from three axial springs and three rotational springs (referenced to local coordinate axes n-s-t) as shown in Figure 3-14 (the rotational springs have been omitted for clarity). The local spring coefficients are assigned according to

$$k_s = k_t = \beta_1 k_n = \beta_1 \beta_2 E \frac{A_{ij}}{h_{ij}} \tag{3-18}$$

in which E is the Young's modulus and A_{ij} is the area of the Voronoi boundary common to nodes i and j. By adjusting $\beta 1$ and β_2 in accordance with experimental results, macroscopic modeling of both elastic constants (E and Poisson ratio,) is possible. The Voronoi scaling of the spring constants, A_{ij}/h_{ij}, enables the method to be elastically homogeneous under uniform modes of straining. Such Voronoi scaling also results in energy conserving, grid-size-insensitive representations of tensile fracture.

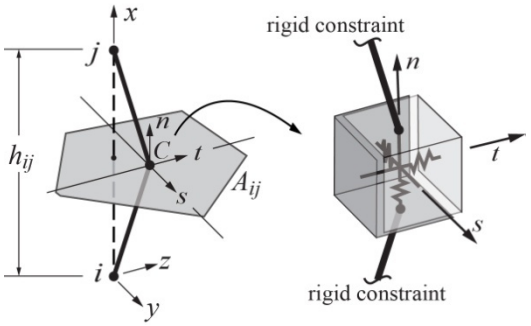

Figure 3-14. Typical lattice element *ij* with a zero-size spring set located at centroid *C* of facet area A_{ij}. Note that A_{ij} is the Voronoi facet or cell boundary, and *i* and *j* are the neighboring Voronoi cell nodes (matrix nodes).

In this study, the strength properties of the RBSN elements are defined by a Mohr-Coulomb criterion as shown in Fig. 3-15. The fracture line is defined by three parameters: the angle of internal friction φ (surface inclination with respect to the σ_n axis), surface intersection c with the shear axis; and the tensile strength, f_n, of the material. Axial stresses are measured as $\sigma_I = F_I/A_{ij}$, where F is axial spring force and I indicate corresponding each of the *n-s-t* local axes, respectively. The stress condition at each element is measured as $\rho = \mathrm{OP}/\mathrm{OP_o}$, where $\mathrm{OP_o}$ is the point at which $\mathrm{OP} = \sqrt{\sigma_n^2 + \sigma_s^2 + \sigma_t^2}$ intersects the fracture surface. Element breaking occurs when $\rho = 1$. The most critical element undergoes fracture in a brittle manner, which entails a complete reduction of its elastic stiffness and an associated release of element forces.

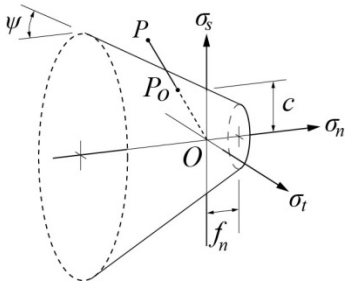

Figure 3-15. Mohr-Coulomb surface with tension cut-off.

3.5.2 Anisotropy in the RBSN model

As discussed in Section 3.2 the Opalinus Clay presents strong anisotropy as shown by comparing a number of properties measured parallel or perpendicular to the bedding planes. In terms of the rock elastic mechanical behavior, anisotropy is found in Young's modulus, shear modulus, and Poisson's ratio (Bossart, 2012). Anisotropy is also found for tensile and cohesive strength, however, friction angle is close to isotropic (Bossart, 2012). Because the RBSN model is a mechanical analogue to the continuum equations for rock mechanics, methodologies to match continuum properties using the RBSN model must be developed. Methods for matching isotropic values of Young's modulus and Poisson's ratio have been discussed previously (Liu et al., 2013). Here we discuss one methodology using a layered system which leads to anisotropic bulk elastic and strength properties in the RBSN model. This in fact mimics the physical system because bedding is the feature in the Opalinus Clay that drives anisotropy. As we will show, using alternating soft and stiff layers can produce the desired bulk anisotropic behavior.

3.5.2.1 Anisotropic elastic properties

Qualitatively, it is clear that a system built from layers that are individually homogenous and isotropic but have properties that vary from layer to layer will result in effective bulk anisotropy. Consider a system with two layers of equal thickness, one with a low Young's modulus and one with a high Young's modulus. If force is applied orthogonal to the layers, the soft layer will dominate the resulting strain of the system. However, if force is applied parallel to the layers, the stiff layer will dominate the resulting strain of system. The exact linkage for elastic properties (Young's modulus, shear modulus, and Poisson's ratio) between layer properties and the bulk rock properties has been derived (Salamon, 1968), so the effective bulk rock properties may be computed from known layer properties. Young's modulus for the Opalinus Clay is characterized by different values parallel and normal to bedding, E_p = 15.5 GPa and E_n = 9.5 GPa, respectively (Bossart, 2012). The relationships between the bulk and layer Young's modulus are,

$$E_p = \phi_1 E_1 + \phi_2 E_2 \tag{3-19}$$

$$E_n = 1/(\frac{\phi_1}{E_1} + \frac{\phi_2}{E_2}) \tag{3-20}$$

where ϕ_i is the volume fraction and E_i is Young's modulus for each layer i.

For alternating layers of equal thickness, there is a unique pair of individual layer properties that will produce a given pair of anisotropic bulk rock properties. For such conditions, Young's modulus for two layers, E_1 and E_2 , can be calculated to be 25.1 GPa and 5.8 GPa, respectively. The exact nature of the layering that exists in the Opalinus Clay has not been investigated in detail and individual layer characteristics are not known. However, the formation is known to be finely bedded and numerous measurements have been made of the bulk rock geomechanical properties. So our approach is to use alternating layers of equal thickness and assign layer properties such that the correct bulk rock behavior is obtained. Although not addressed in the current study, it should be pointed out that layering is also a potential avenue to represent anisotropic hydrogeological properties. While hydrogeological anisotropy in permeability using TOUGH2 can be implemented directly for a structured grid oriented along the principal axes, modeling permeability anisotropy for a general unstructured grid is a subject of current research.

3.5.2.2 Anisotropic strength properties

Anisotropic strength behavior is also found for the Opalinus Clay as discussed in Section 3.4. This anisotropy is represented in the RBSN through alternating stiff and soft layers as presented in Section 3.5.2.1 for elastic properties. The basis for evaluating the individual layer properties is shown in Figure 3-16.

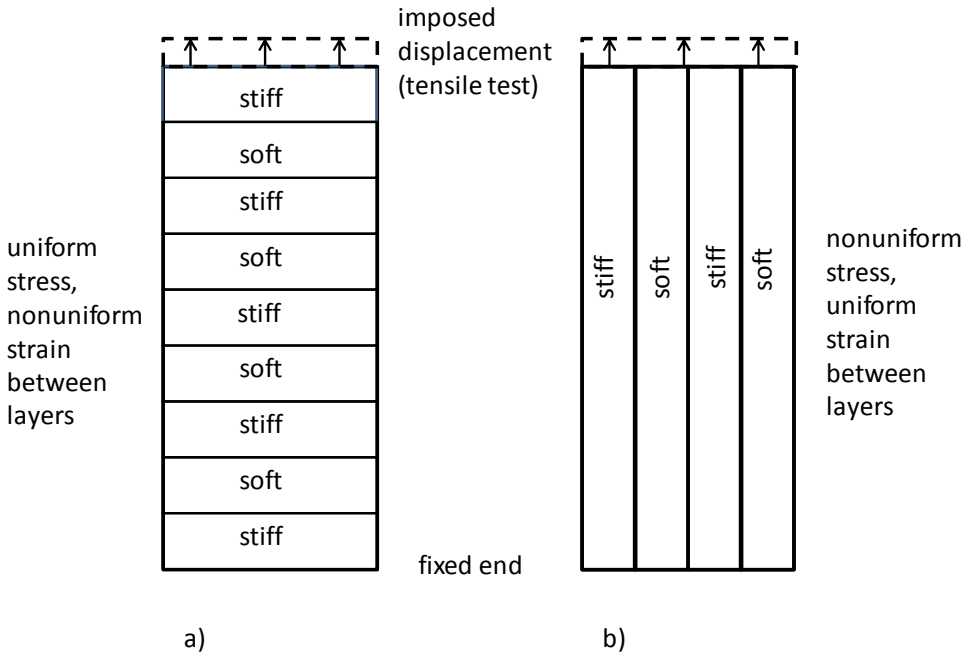

Figure 3-16. Tensile strength test for layered rock. a) strength perpendicular to the layers; b) strength parallel to the layers

A uniaxial tensile strength test causes different responses when the imposed displacement is parallel or perpendicular to the layering. In Figure 3-16a), the displacement is perpendicular to the layers. For this orientation, a uniform displacement of the top end of the sample (with the other end held motionless) results in a uniform stress across the material with different strains within the stiff and soft layers. Because stress is uniform, it is clear that the tensile strength of the layered rock will be equal to the value in the soft layer because it will fail at lower stress. For displacement parallel to bedding shown in Figure 3-16b), the strain, ε, will be uniform across the sample, however, stress will vary between the stiff and soft layers. The bulk stress, σ_B, is equal to the total force divided by the bulk area, A_B. The total force, F_T, is the sum of the forces for the soft and stiff layers,

$$F_T = \varepsilon(A_1E_1 + A_2E_2) \tag{3-21}$$

Where A_1 is the total area of stiff layers, A_2 is the total area of soft layers, E_1 is Young's modulus for the stiff layer, and E_2 is Young's modulus for the soft layer. Because the stiff and soft layers have equal area, this becomes

$$F_T = A_B\varepsilon\left(\frac{E_1+E_2}{2}\right) = A_B\bar{E}\varepsilon \tag{3-22}$$

where $\bar{E} = \frac{E_1+E_2}{2}$. Then the bulk stress is given by

$$\frac{F_T}{A_B} = \sigma_B = \bar{E}\varepsilon \tag{3-23}$$

To obtain the tensile strength of the strong layer, T_1, such that tensile failure occurs when the bulk stress reaches the tensile strength of the bulk rock parallel to the layering, T_{BP}, the strain is

$$\varepsilon = \frac{T_{BP}}{\bar{E}}. \tag{3-24}$$

Then the stress in the strong layer associated with this strain is the tensile strength of the stiff layer,

$$T_1 = \frac{E_S}{\bar{E}} T_{BP}. \tag{3-25}$$

If, instead of tensile loading the sample is placed under compressive loading the results are similar. For compressive loading, the displacement of the top of the material is reversed to move downward in Figure 3-16. For compressive loading oriented perpendicular to the layering, the stress is uniform and failure will occur at the same stress as for the soft layer. Therefore, the bulk rock cohesive strength perpendicular to the layering equals the cohesive strength of the soft layer. For displacement parallel to the layering, the relationships remain as for the tensile case. That is, the magnitude of the maximum (vertical) normal stress required to achieve failure in the stiff layer, σ_1, is equal to

$$\sigma_1 = \frac{E_1}{\bar{E}} \sigma_{BP} \tag{3-26}$$

where $\sigma_{BP}$is the maximum normal stress parallel to bedding required for failure of the bulk rock. Figure 3-17 shows a schematic diagram of the Mohr-Coulomb failure envelopes for the bulk rock and for the stiff layer (the diagram is schematic only – it does not correspond quantitatively with parameter values for the Opalinus Clay). The envelopes are parallel because, according to Bossart (2012), the friction angle, φ, is approximately isotropic and equals 25°. Therefore, there is only one friction angle for the individual layers and for the layered rock. As shown in Figure 3-17, the cohesive strength scales the same as the maximum normal stress on Mohr's circle such that

$$c_1 = \frac{E_1}{\bar{E}} c_{BP}\ , \tag{3-27}$$

where c_s is the cohesive strength of the stiff layer and c_{BP} is the bulk cohesive strength of the layered system parallel to the bedding.

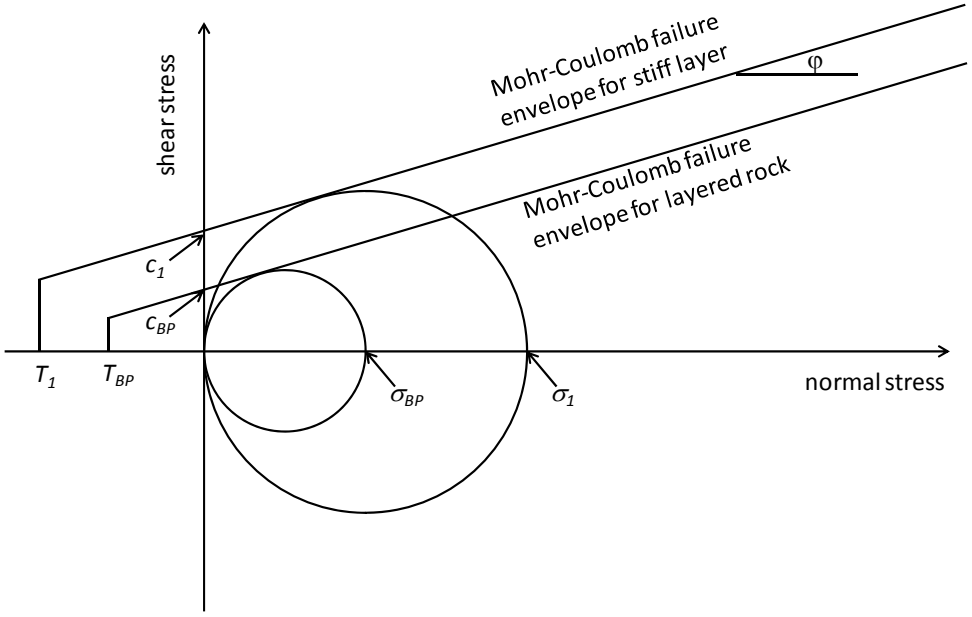

Figure 3-17. Schematic of the Mohr-Coulomb failure diagram for the layered rock and the strong layer.

The Young's moduli for the strong and weak layers are 5 and 25 GPa, respectively, as presented in Section 3. 5.2.1. Therefore, $\frac{E_1}{\bar{E}} = 5/3$. The bulk rock tensile and cohesive strengths and the stiff and soft layer values are given in Table 3-1.

Table 3-1. Tensile and cohesive strengths of layered rock and individual layers.

	tensile strength perpendicular to layers (MPa)	tensile strength parallel to layers (MPa)	cohesive strength perpendicular to layers (MPa)	cohesive strength parallel to layers (MPa)
layered rock	1	2	2.2	5.5
	tensile strength (isotropic) (MPa)		cohesive strength (isotropic) (MPa)	
stiff layer	3.33		9.17	
soft layer	1		2.2	

Note: source for layered rock values is Bossart (2012).

3.5.2.3 Voronoi discretization of transversely isotropic rock

Voronoi discretization is an effective approach for partitioning a computational domain containing a set of nodal points within a set of spatial regions or cells. Each cell is associated with an individual nodal point such that all locations within the cell lie closer to the given nodal point than to any other nodal point. The Voronoi grid is computed from the nodal point set by first constructing the Delaunay tessellation, which is then used to construct the dual Voronoi tessellation (Asahina and Bolander, 2011).

Here, the Voronoi grid is used to represent transversely isotropic rock. The bedding configuration is directly mapped onto Voronoi cells and the boundaries of layer are identified by the edges of a polygon. Figure 3-18 shows a reference geometry of transversely isotropic material and its approximation by a collection of Voronoi cells. With reference to the 2-D case, a transversely isotropic specimen is discretized as follows:

- Discretize rock matrix based on an irregular Voronoi grid (Fig. 3-18(a)).
- Overlay the reference layers onto the Voronoi grid (Fig. 3-18(b)).
- Select node for each reference layer. The corresponding Voronoi cells represent the reference layers (Fig. 3-18(c)).

By automating this approach, layered materials can be effectively generated. Figure 3-19 shows the discretized two phase transversely isotropic material for equal volume fraction with different angles.

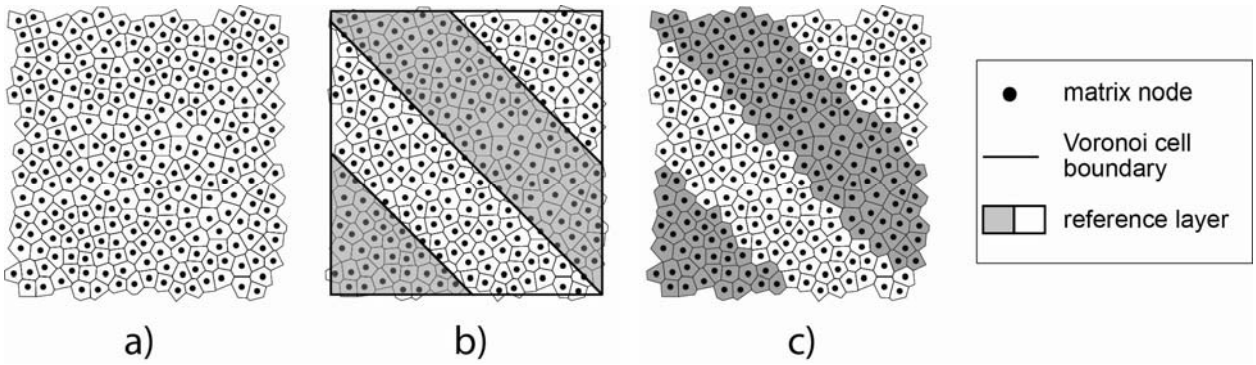

Figure 3-18. (a) An irregular 2-D Voronoi grid, (b) Voronoi grid with overlay transverse isotropic layer, and (c) Voronoi grid representation of transversely isotropic material.

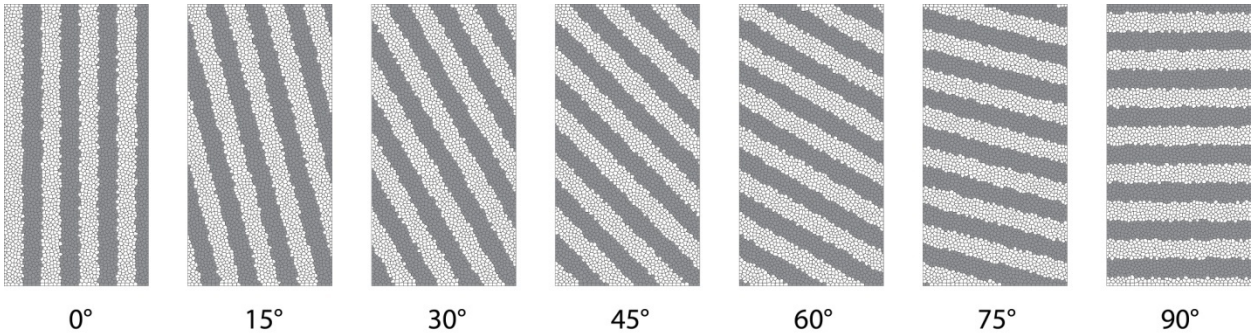

Figure 3-19. 2-D Voronoi discretization of transversely isotropic materials with 7 different bedding angles.

3.5.3 Modeling compression failure with RBSN

Failure in compression is more complex than failure in tension because combined modes of failure (tension and shear) are possible. Identification of compressive behavior and failure characteristics such as specific fracture energy and local failure mechanisms is difficult. Furthermore, heterogeneous composition and anisotropy found in many geomaterials lead to complications in determining the elastic properties of the continuum. To accurately model compressive behavior and failure processes of heterogeneous and anisotropic materials one needs to:

- Introduce heterogeneity in the model to capture the fracture processes and strength characterization.
- Select fracture criteria and the associated parameters. For example, cohesion and friction angle are inputs for a Mohr-Coulomb fracture criterion.

Several approaches have been applied to include the effect of heterogeneity in fracture-damage models such as, random assignment of different element properties based on spatial heterogeneous distribution (Tang, 1997), random geometry of mesh with equal properties for the elements (Garboczi and Day, 1995), mapping micro/meso structure onto regular/irregular mesh (Schlangen and Van Mier, 1992; Asahina et al., 2011), random geometry of mesh and associated grain structure (Cusatis et al., 2003), and statistical approach with a Weibull distribution (Tang, 1997). Although it is possible in the RBSN model to simulate heterogeneity of a rock, in this study the focus is on anisotropic behavior as discussed in Section 3.5.2.

3.5.3.1 Numerical example: uniaxial compression for two homogeneous rocks

Prior to modeling transversely isotropic materials, homogeneous specimens are considered here to demonstrate the basic simulation capability of RBSN model under uniaxial compression loading. Consider a 2-D section of cylindrical core sample which is subjected to unconfined uniaxial compression as shown in Fig. 3-20(a). The model is discretized with about 10,000 lattice elements and 3,800 nodes. The top and bottom cells, represented with darker cells in Fig. 3-20(a), are restrained while others are free to move. Incremental loads are applied along top layer by displacement control and load rate/duration effects are not considered. Two Young's moduli, 25.1 GPa and 5.8 GPa, obtained in section 3.5.2.1 are used to represent two homogeneous specimens. Fracture is based on a multi-component vectorial measure of stress, limited by a Mohr-Coulomb surface with a tension cut-off (Figure 3-15). The cohesive strength, and the internal friction angle is set to 3.5 MPa, and 25°, respectively, reported as best approximation of the Opalinus Clay in the literature (Bossart, 2012). The tensile strength is set to 1.5 MPa which is the mean value of uniaxial tensile strength of normal to bedding, 1 MPa, and parallel to bedding, 2 MPa, of the Opalinus Clay.

As can be seen in the axial stress and strain curves in Fig. 3-21, the model shows brittle behavior. After the first element breakage neighboring elements undergo fracture even without increasing the load point displacement. After many of the elements have broken, the fracture process stabilizes in the sense that small load steps no longer produce bursts of element failures. Young's moduli obtained by the stress-strain curve agree with their elemental values. Figure 3-20(b)-(d) shows simulated fracture processes under uniaxial compressive loading. The broken line in Fig. 3-20 (b) indicates the angle of 57.5° which is based on the critical plane angle $\varphi/2 + 45°$. As indicated, the angle of shear failure in early stage of fracture development roughly captures this theoretical angle.

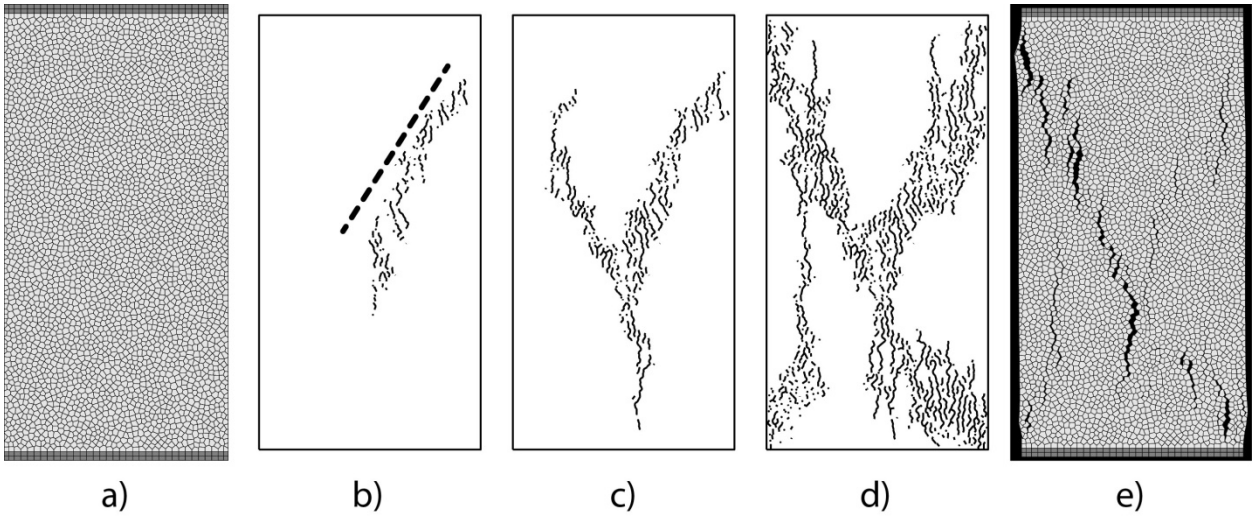

Figure 3-20. 2-D specimen under uniaxial compression loading: a) Voronoi discretization, (b), (c), (d) fracture processes in early, intermediate, and late stages, and (e) failure patterns in late stage.

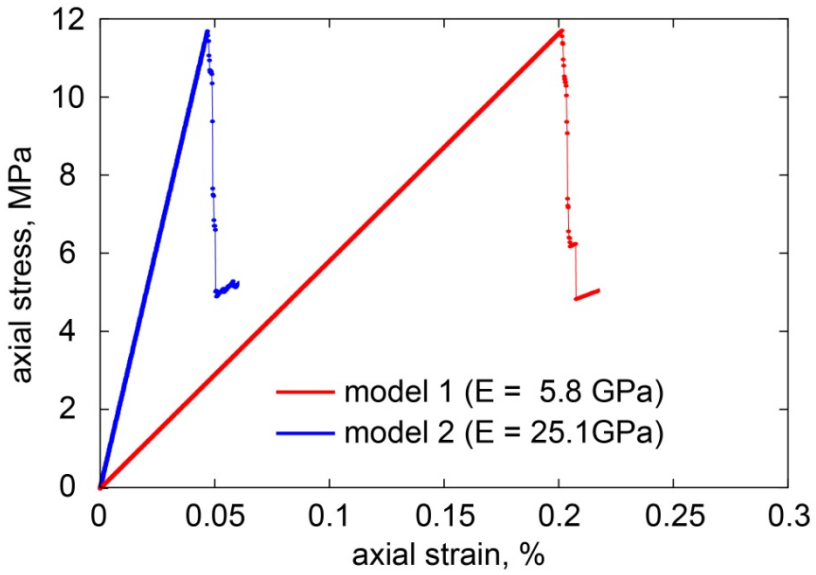

Figure 3-21. Axial stress-strain curve of two homogeneous rock models under uniaxial compression loading.

3.5.3.2 Numerical example: uniaxial compression for transversely isotropic rock

Compressive behavior and failure of the transversely isotropic rocks are simulated using the RBSN modeling. Figure 3-D4 shows the Voronoi discretization of 2-D specimens with seven different angles. The same loading boundary conditions used for the homogeneous materials (section 3.5.3.5) are considered. As discussed in Section 3.5.2.2, the stiff and soft phases are alternatively layered, and each layer is assumed to be a homogeneous. The bulk Young's modulus with different bedding angle can be obtained by (Pariseau, 2006):

$$\frac{1}{E} = \frac{\cos^2(\beta)}{E_p} + \left(\frac{1}{G_{12}} - \frac{2\nu_{12}}{E_p}\right)\sin^2(\beta)\cos^2(\beta) + \frac{\sin^4(\beta)}{E_n} \tag{3-27}$$

where β is the angle between the normal to the bedding plane and axial load, G_{12} is shear modulus, and ν_{12} is Poisson's ratio. When Poisson's ratio is set to zero and equal volume fraction for the stiff and soft phases is used, G_{12} can be expressed as:

$$G_{12} = 1 \Big/ \left(\frac{1}{E_p} + \frac{1}{E_n}\right) \tag{3-28}$$

Figure 3-22 compares the results of Eq 3-27 and simulated bulk Young's modulus with three different layer thicknesses, d/5, d/7.5, and d/15, where d is the diameter (width in 2-D model) of the sample. The variation in elastic modulus is found to be nearly independent of layer thickness. The numerical results for bulk Young's modulus using at bedding angles of β = 0° and 90° show good agreement with measured values from the Opalinus Clay for these orientations, E_p= 15.5 GPa and E_n = 9.5 GPa, respectively (Bossart, 2012). Agreement for other bedding angles (β = 15°, 30°, 45°, 60°, 75°) can be viewed as predictions. The numerical model results roughly agree with the analytical values.

Figures 3-23 through 3-29 show fracture developments of transversely isotropic rock for each bedding angle. Although Young's modulus is varied between stiff and soft layers, for the simulations in Figures 3-24 through 3-30, cohesive and tensile strength are the same in both stiff and soft layers. The light- and

dark-shaded regions represent stiff and soft phase, respectively. For most cases, many fractures occur within one loading step.

In Figure 3-23, the bedding is parallel to the loading direction resulting in a bedding angle of 0°. Layering is seen to dominate both fracture orientation and distribution. Failure is found to occur first in the stiff layers (Figure 3-23 b) and c)), which is consistent with the conceptual arguments given in Section 3.5.2.2. However, as fractures develop, failure spreads into the soft layers as well (Figure 3-23 d)). Similar trends are also found when bedding is at a 15° angle to the loading direction in Figure 3-24.

The fracture pattern begins to change when the bedding angle reaches 30°, as shown in Figure 3-25. Although the initial fracture orientation still follows the bedding angle, the fractures are initially formed preferentially in the soft layers rather than the stiff layers. This occurs because there is now sufficient stress across the layers such that the load is not supported as much by the stiff layers. As fracturing continues (Figure 3-25 c) and d)), there is some loss of the orientation of the fracturing along bedding. The pattern is roughly similar for the case with a bedding angle of 45°, but the orientation of fractures along the bedding angle deteriorates further, as shown in Figure 3-26. At later stages (Figure 3-26 c) and d)), a secondary overall fracture orientation appears. The orientation of the secondary fracture pattern is associated with the friction angle of the material rather than the bedding angle.

At the highest bedding angles in Figures 3-27, 3-28, and 3-29, the orientation of the general fracture pattern departs from the bedding angle and begins to follow an orientation associated with the friction angle of the material. As for a homogeneous material (Figure 3-20), the general fracture pattern shows two orientations. Furthermore, fracturing is not focused in the stiff or soft layers because at high bedding angles there is a more uniform stress distribution across layers as discussed in Section 3.5.5.2. Therefore, fracturing should be reasonably equivalent in the different layers, given uniform cohesive and tensile strength across layers.

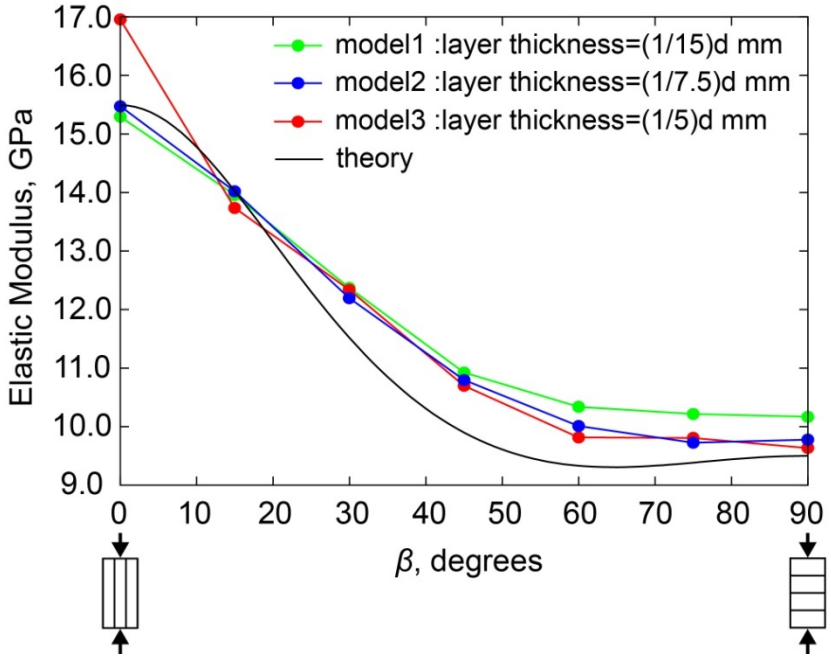

Figure 3-22. Variation of elastic modulus with the angle β between the bedding plane and the loading (vertical) direction.

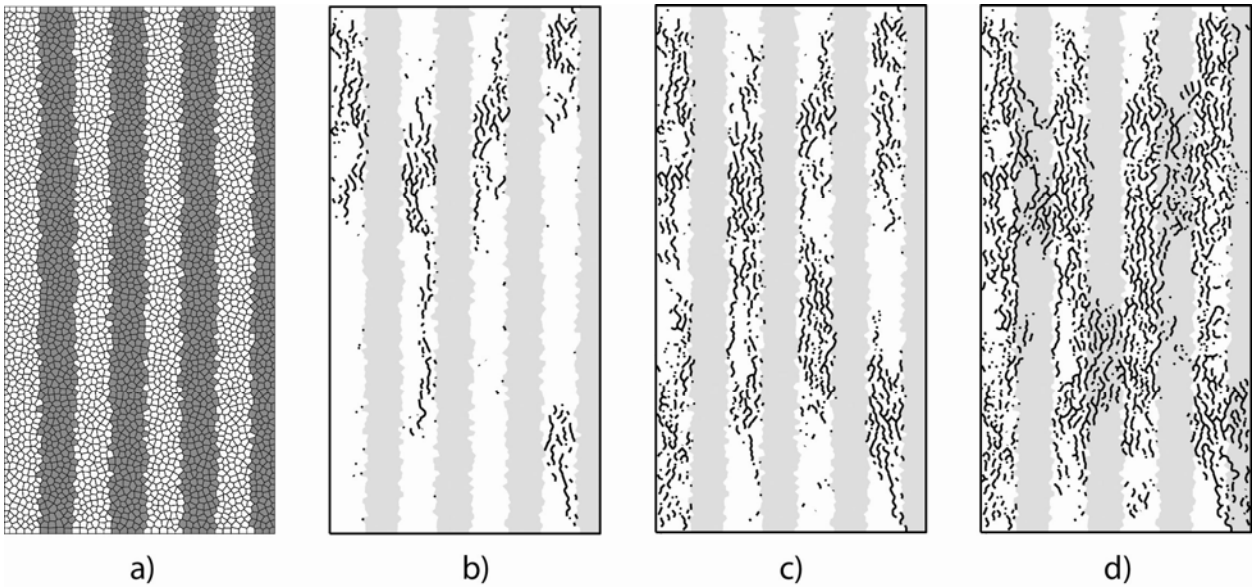

Figure 3-23. Transversely isotropic rock with bedding angle β=0°: (a) Voronoi discretization, (b), (c), (d) numerical results of fracture processes under uniaxial compression loading (early, intermediate and late stages).

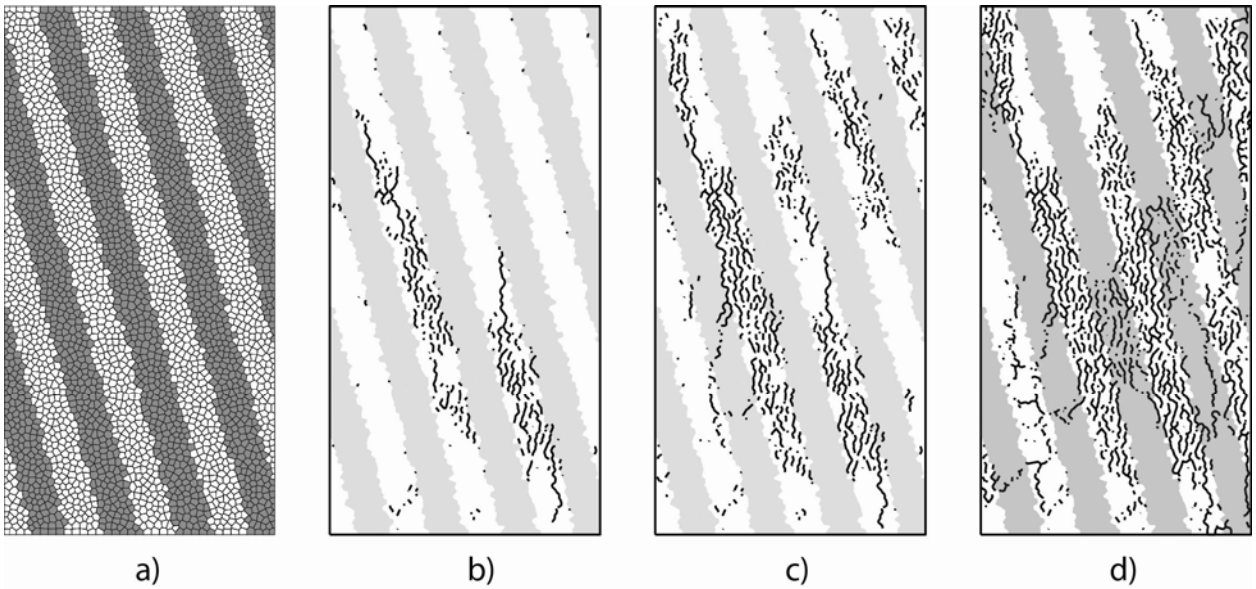

Figure 3-24. Transversely isotropic rock with bedding angle β=15°: (a) Voronoi discretization, (b), (c), (d) numerical results of fracture processes under uniaxial compression loading (early, intermediate and late stages).

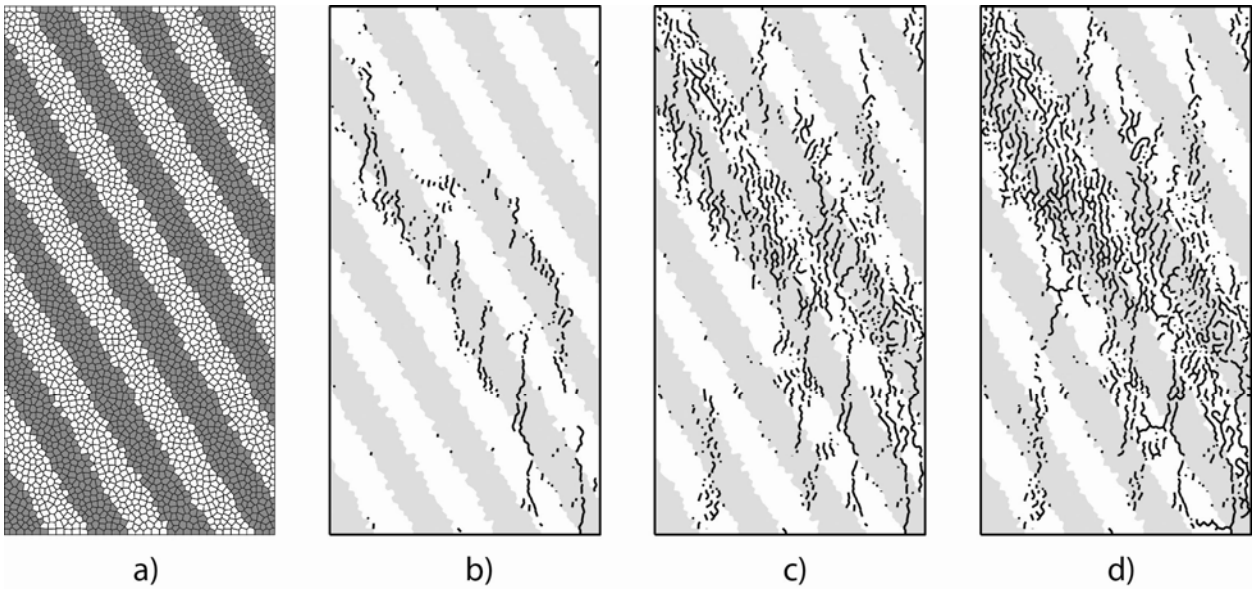

Figure 3-25. Transversely isotropic rock with bedding angle β=30°: (a) Voronoi discretization, (b), (c), (d) numerical results of fracture processes under uniaxial compression loading (early, intermediate and late stages).

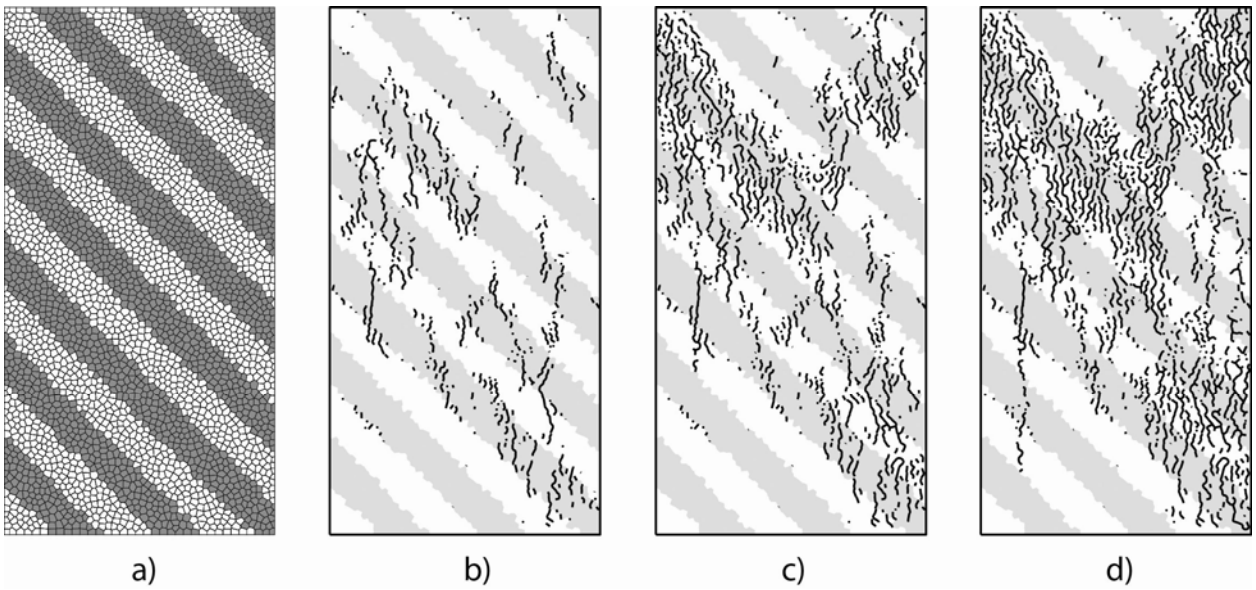

Figure 3-26. Transversely isotropic rock with bedding angle β=45°: (a) Voronoi discretization, (b), (c), (d) numerical results of fracture processes under uniaxial compression loading (early, intermediate and late stages).

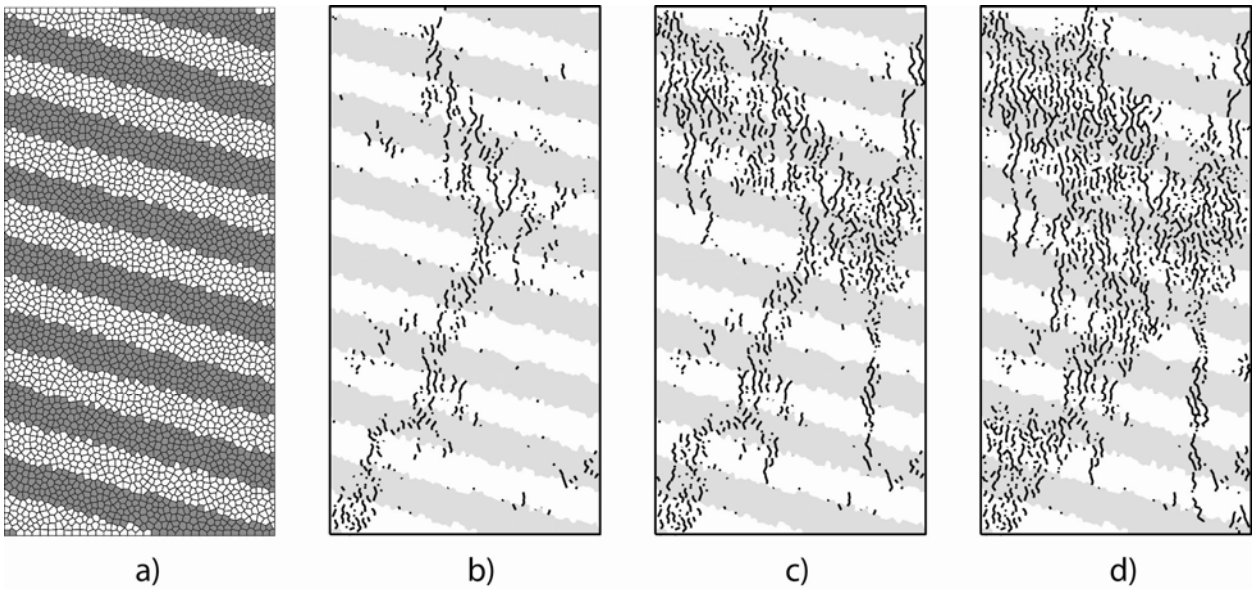

Figure 3-27. Transversely isotropic rock with bedding angle β=60°: (a) Voronoi discretization, (b), (c), (d) numerical results of fracture processes under uniaxial compression loading (early, intermediate and late stages).

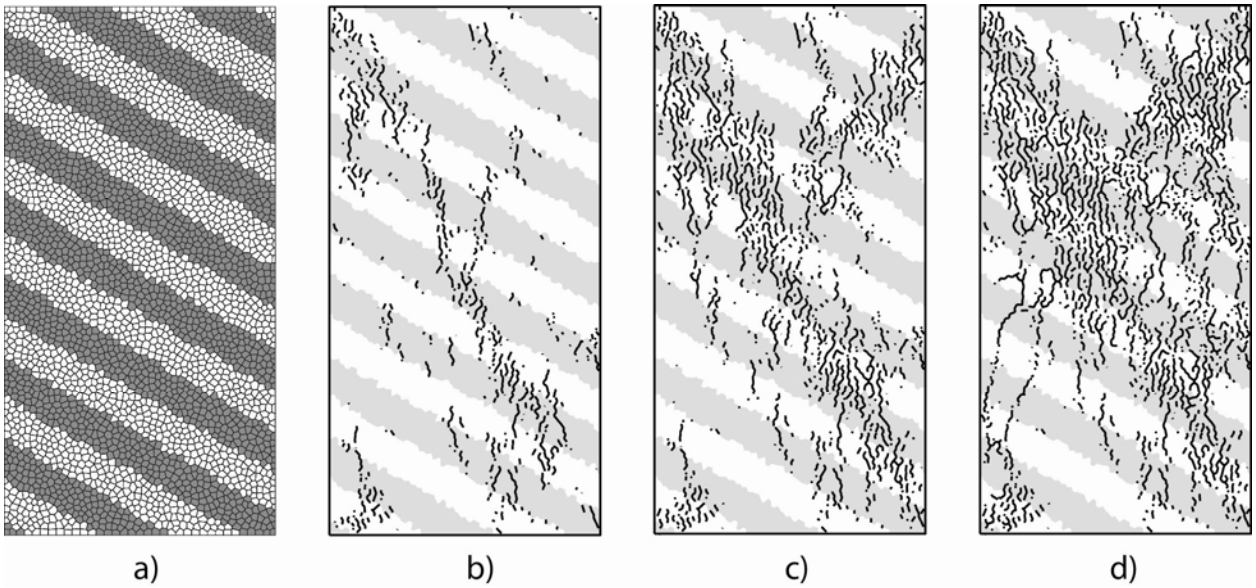

Figure 3-28. Transversely isotropic rock with bedding angle β=75°: (a) Voronoi discretization, (b), (c), (d) numerical results of fracture processes under uniaxial compression loading (early, intermediate and late stages).

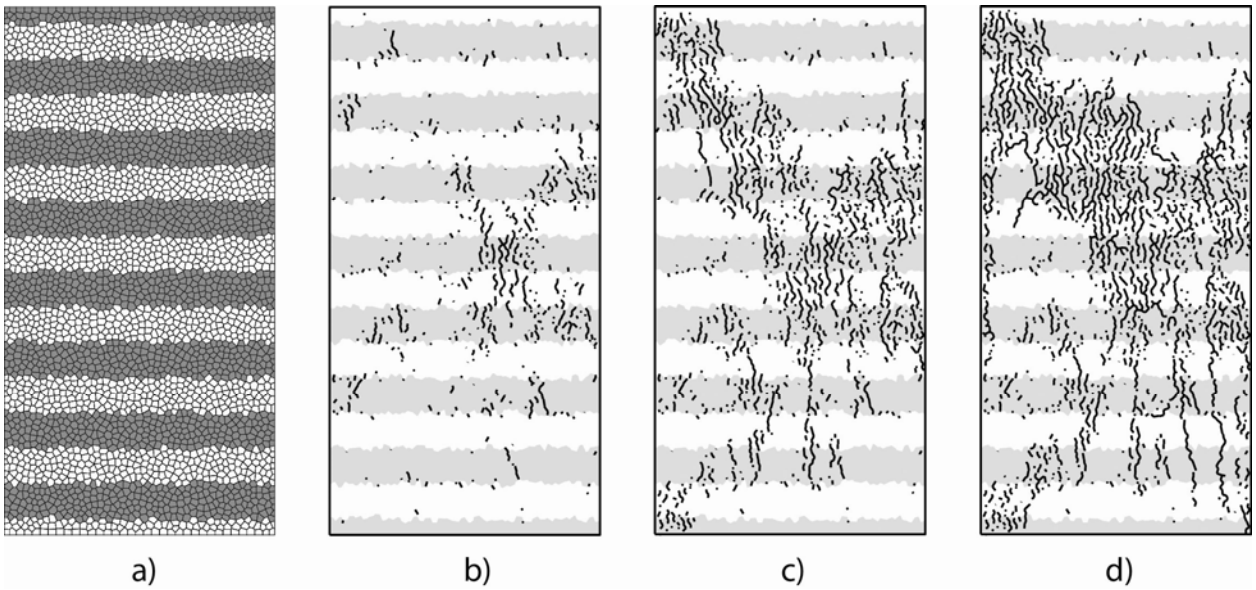

Figure 3-29. Transversely isotropic rock with bedding angle β=90°: (a) Voronoi discretization, (b), (c), (d) numerical results of fracture processes under uniaxial compression loading (early, intermediate and late stages).

3.5.4 Fracture damage modeling of the HG-A test

In this section we present the initial simulation of the Opalinus Clay's geomechanical and fracture damage response in the vicinity of the 1-m diameter HG-A microtunnel using the RBSN model. This simulation uses the modeling methodologies described in Section 3.5.1 for shear fracture and in Section 3.5.2 for representing anisotropic properties of the Opalinus Clay.

First, the basic stress profiles around the microtunnel under compressive stress condition are simulated using the RBSN model. Figure 3-30 (a) shows the 2D computational domain, which is 10m×10m with a circular opening (having a radius of 0.5 m) at the center, and is subjected to a far-field compressive stresses of 4.5 MPa in the horizontal direction and 6.5 MPa in the vertical direction. The model is considered as a homogeneous and isotropic material, whose elastic modulus and the Poisson's ratio are 15.5 GPa and 0.3, respectively. Figure 3-30(a) shows a discretization of the computational domain and the boundary conditions. The areal density of nodal points (or Voronoi grid size) can be controlled by changing a minimum allowable distance between nodes as a function of spatial coordinates (Asahina and Bolander, 2011). This problem may also be solved analytically using the Kirsch (1898) solution presented in Section 3.4. Figure 3-30(b) shows the RBSN simulation results and analytical model results for the stress profiles versus distance from the center of the domain. The RBSN model results closely match the analytical model results.

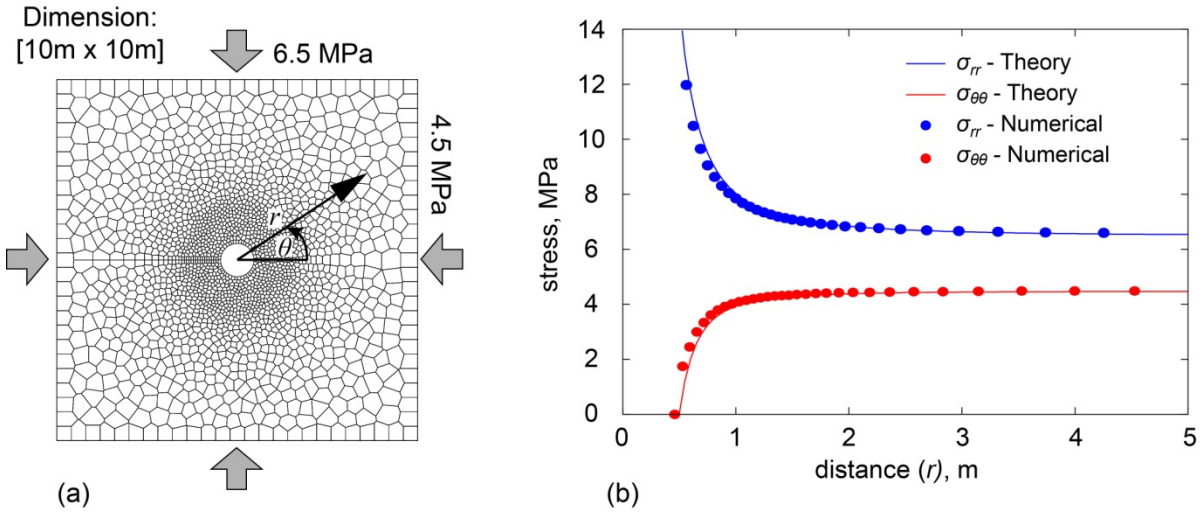

Figure 3-30. (a) Computational grid used for the RBSN simulator (2044 nodes), and (b) simulation results of radial and tangential stress for θ=0° versus the distance from the center of the domain.

Next, transverse isotropy is generated around the microtunnel with higher nodal density as shown in Figure 3-31. The layered system is discretized within a 1.5 m radius around the microtunnel to keep a manageable computational cost associated with the number of nodes. Beyond the 1.5 m radius, the rock matrix is represented as homogeneous and isotropic. The material properties for each phase used in the RBSN model are summarized in Table 3-2. Figure 3-31(c) shows fracture patterns around the microtunnel. The fractured regions are affected by the material anisotropy and are not symmetric. Non-uniform damage has also been observed around the tunnel in the HG-A test as shown in Figure 3-4. Marschall et al. (2006) observed two types of failure that are postulated to be a result of strength anisotropy and stress anisotropy. Fracturing shown in Figure 3-31(c) is also not distributed symmetrically around the tunnel. Fracturing is focused in the soft layers, which is expected based on the reduced material strength in the soft layer. However, the failure mechanism around the microtunnel is not simple because of interactions with the anisotropic strength and stress field and with pre-existing tectonic structures. As shown in Figure 3-4, most of the observed damage at the tunnel wall is associated with pre-

existing faults. Nevertheless, the differences in damage distribution relative to the orientation of bedding between Figures 3-31(c) and 3-4 needs to be investigated in future studies.

Table 3-2. Material properties for the Opalinus Clay.

	Stiff layer	Soft layer	Matrix (r >1.5m)
Young's modulus (GPa)	25.1	5.8	15.5
Poisson's ratio	0.3	0.3	0.3
Tensile strength (MPa)	3.3	1.0	2.2
Internal friction angle (degree)	25	25	25
Cohesion (MPa)	9.17	2.2	4.8

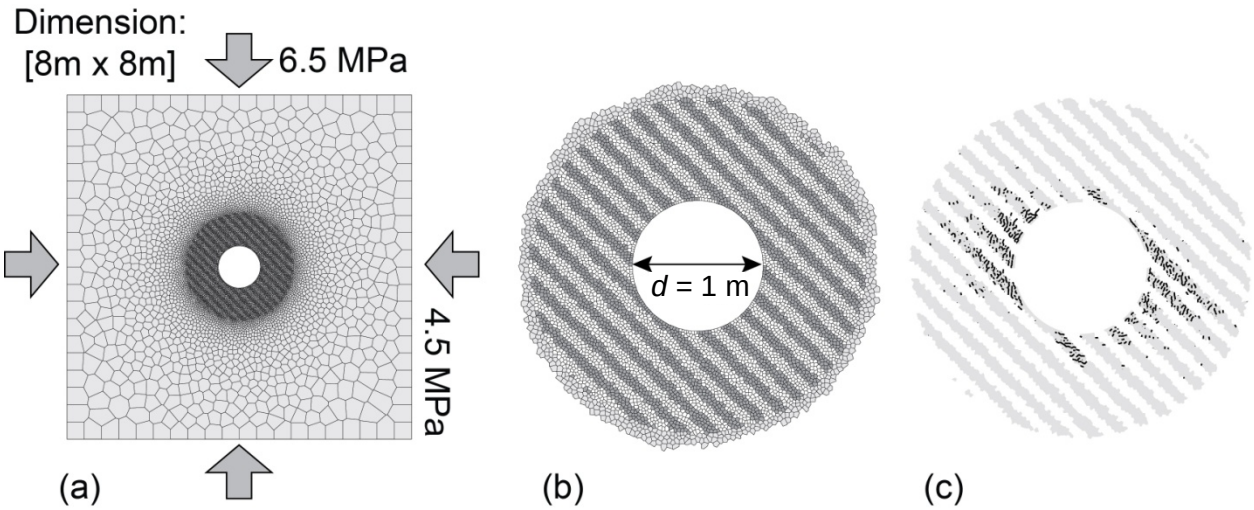

Figure 3-31. (a) Computational grid used for the RBSN simulator (10248 nodes), (b) enlarged view around the borehole, and (c) simulated fracture pattern.

4. CONCLUDING REMARKS

This report has addressed the following items for testing being conducted at the Mont Terri URL, Switzerland: (1) development and validation of a THM model for FE heater test (Section 2); and (2) development and validation of a hydro-mechanical fracture-damage model for the HG-A test (Section 3). The results of these efforts are summarized here:

FE Heater Test

We conducted new suite of simulations related to the FE test at Mont Terri, including scoping calculations, benchmarking, and some initial predictive modeling of the real heater test. These include model simulations using 1D axisymmetric, 2D plane strain, and full 3D model geometries. We conducted (for the first time) a THM analysis involving the BBM in a full 3D field setting for modeling the geomechanical behavior of the buffer. Compared to our previous 2D model analysis, this 3D analysis provides a much more accurate estimate of the temperature evolution near the heater and thereby should provide a better prediction of the peak temperature. Our current understanding is that the peak temperature may become as high as 160°C at the inner parts of the buffer. However, this prediction strongly depends on the thermal and diffusion properties of the buffer, which are parameters that have presently not been well constrained for this buffer material.

Our THM model simulation was conducted with a simplified buffer mechanical model, whereas a ubiquitous joint model was used for modeling the anisotropic mechanical strength properties of the Opalinus Clay. The analysis showed that some minor failure may occur near the tunnel wall behind the concrete lining after excavation. This failure does not expand much further during the 20-year heating, meaning that the rock mass remains in an elastic mechanical state.

Overall, the initial model analyses showed that our adopted modeling approach is adequate for modeling the coupled THM processes at the FE heater, including all components of bentonite, concrete lining, and Opalinus Clay. We managed to discretize the 3D model using the inclined mesh in both TOUGH2 and FLAC3D, and the modeling results are reasonable.

Our next steps will be (1) to compare our benchmarking simulation results with those of the other international modeling teams, (2) to model newly available laboratory experiments for constraining THM parameters of the MX-80 granular bentonite, and (3) provide a final prediction of FE heater experiment (should be completed and reported before start of heating).

HG-A Test

Use of the RBSN model for the HG-A test requires development of two additional model capabilities: (1) a method for computing fracturing under compressive load and (2) a method to treat the anisotropic geomechanical properties of the Opalinus Clay. The use of the Mohr-Coulomb failure criterion led to RBSN model predictions for fracturing under compressive load that roughly follow trends expected for a homogeneous medium. For a layered system, the results were also reasonable in that fracturing followed the stiff layers for high bedding angles but was not controlled by bedding at low bedding angles. Currently, rock failure is modeled using a brittle model in which all strength is lost at failure. However, a more realistic failure response results in a more gradual loss of strength following failure. In addition, contacts along fracture surfaces under compressive loads will lead to friction along fracture planes not currently accounted for in the model. Anisotropic properties for the bulk rock were represented in the RBSN model using layered heterogeneity. While the current approach was successful at producing the desired anisotropic bulk properties and trends for fracture behavior under compressive load, significant

differences remain between the RBSN results and observations in the HG-A test, indicating that further model development is needed. The results and test observations suggest that:

1. Either finer layering or a different approach may be needed for modeling anisotropic behavior.
2. Additional mechanisms need to be investigated for fracture under compressive load.
3. The geomechanical characteristics of existing fault features in the rock need to be incorporated.

Future work will also address:

1. Coupling of the hydro-mechanical response for post-excavation dryout and fracture formation and the associated dynamic pore-pressure response.
2. Development of a three-dimensional model capable of representing the HG-A fluid injection tests.

5. ACKNOWLEDGMENT

Funding for this work was provided by the Used Fuel Disposition Campaign, Office of Nuclear Energy, of the U.S. Department of Energy under Contract Number DE-AC02-05CH11231 with Lawrence Berkeley National Laboratory.

REFERENCES

Alonso, E.E., Gens, A., Josa, A. (1990). A constitutive model for partially saturated soils, *Géotechnique*, 40(3), 405-430.

Asahina, D., Bolander, J.E. (2011). Voronoi-based Discretizations for Fracture Analysis of Particulate Materials, *Powder Technology*, 213, 92-99.

Asahina, D., Landis, E.N., Bolander, J.E. (2011). Modeling of phase interfaces during pre-critical crack growth in concrete, *Cement & Concrete Composites*, 33, 966-977.

Birkholzer, J.T. (2012). Status of UFD Campaign International Activities in Disposal Research. Report prepared for U.S. Department of Energy Used Fuel Disposition Campaign, FCRD-UFD-2012-000295.

Birkholzer, J., Asahina, D., Chen, F., Gardner, P., Houseworth, J., Jove-Colon, C., Kersting, A., Nair, P., Nutt, M., Li, L., Liu, H.H., Painter, S., Reimus, P., Rutqvist, J., Steefel, C., Tynan, M., Wang, Y., Zavarin, M. (2013). An overview of US disposal research activities linked to international URLs. Proceedings of the 2013 International High-Level Radioactive Waste Management Conference (IHLRWM), April 28 – May 2, 2013, Albuquerque, New Mexico.

Bock, H. (2001). RA Experiment Rock Mechanics Analyses and Synthesis: Data Report on Rock Mechanics, Mont Terri Project, Technical Report 2000-02.

Bolander, J.E., Saito, S. (1998). Fracture analyses using spring networks with random geometry, *Eng Fract Mech*, 61, 569-91.

Bossart, P. (2012). Characteristics of the Opalinus Clay at Mont Terri, http://www.mont-terri.ch/internet/mont-terri/en/home/geology/key_characteristics.parsys.49924.DownloadFile.tmp/characteristicsofopa.pdf

Corkum, A.G., Martin, C.D. (2007). The Mechanical Behaviour of Weak Mudstone (Opalinus Clay) at Low Stresses, *International Journal of Rock Mechanics and Mining Sciences*, 44, 196-209.

Cusatis, G., Bažant, Z.P., Cedolin, L. (2003). Confinement-shear lattice model for concrete damage in tension and compression: I. Theory, *Journal of Engineering Mechanics*, 129 (12), 1439-1448.

Ewing, J., Senger, R. (2011). Evolution of Temperature, Pressure and Saturation in the Bentonite Buffer: Scoping Calculations in Support of the Design of the Full-Scale Emplacement Experiment at the Mont Terri URL. NAGRA NAB 10-38, September 2011.

Freivogel, M., Huggenberger, P. (2003). Modellierung bilanzierter Profile im Gebiet Mont Terri - La Croix (Kanton Jura), in: Geology, Paleohydrology and Stress Field, Heitzmann & Tripet (eds.), Reports of the Federal Office for Water and Geology (FOWG), Geology Series 4, Switzerland.

Garboczi, E.J., Day, A.R. (1995). An algorithm for computing the effective linear elastic properties of heterogeneous material: 3D results for composites with equal Poisson ratios, *J. Mech. Phys. Solids*, 43, 1349-1362.

Garitte, B. (2013). FMT FE-Experiment: 1D Benchmark definition for the modelling groups. Aktennotiz AN 13-300, NAGRA, Wettingen, Switzerland.

Garitte, B., Gens, A. (2012). TH and THM Scoping computations for the definition of an optimal instrumentation layout in the Full-scale Emplacement (FE). experiment NAGRA NIB 10-34, March 2012.

Garitte, B., Gens, A., Vaunat, J., Armand, G. (2013). Thermal Conductivity of Argillaceous Rocks: Determination Methodology Using In Situ Heating Tests, *Rock Mechanics and Rock Engineering* DOI 10.1007/s00603-012-0335-x.

Gens, A., Garitte B., Wileveau Y. (2007). In situ Behaviour of a Stiff Layered Clay Subject to Thermal Loading: Observations and Interpretation, *Geotechnique*, 57, 207-228.

Gens, A., Sanchez, M., Guimaraes, L.D.N., Alonso, E.E., Lloret, A., Olivella, S., Villar, M.V., Huertas, F. (2009). A full-scale in situ heating test for high-level nuclear waste disposal: observations, analysis and interpretation, *Geotechnique* 59, 377–399.

Itasca (2009). FLAC3D V4.0, Fast Lagrangian Analysis of Continua in 3 Dimensions, User's Guide. Itasca Consulting Group, Minneapolis, Minnesota.

Kawai, T. (1978). New Discrete Models and their Application to Seismic Response Analysis of Structures, *Nuclear Engineering and Design*, 48, 207-229.

Kirsch, G. (1898). Die Theorie der Elastizität und die Bedürfnisse der Festigkeitslehre, *Zeitschrift des Vereines deutscher Ingenieure*, 42, 797-807.

Lanyon, G.W., Marschall, P., Trick,T., de La Vaissière, R., Shao, H., Leung, H. (2009). Hydromechanical Evolution and Self-Sealing of Damage Zones around a Microtunnel in a Claystone Formation of the Swiss Jura Mountains, American Rock Mechanics Association, ARMA 09-333.

Liu, H.H., Houseworth, J., Rutqvist, J., Zheng, L., Asahina, D., Li, L., Vilarrasa, V., Chen, F., Nakagawa, S., Finsterle, S., Doughty, C., Kneafsey, T., Birkholzer, J. (2013). Report on THMC modeling of the near field evolution of a generic clay repository: Model validation and demonstration. (FCRD-UFD-2013-000244), U.S. DOE Used Fuel Disposition Campaign.

Marschall, P., Distinguin, M., Shao, H., Bossart, P., Enachescu, C., Trick, T. (2006). Creation and Evolution of Damage Zones Around a Microtunnel in a Claystone Formation of the Swiss Jura Mountains, *Society of Petroleum Engineers*, SPE-98537-PP.

Marschall, P., Trick, T., Lanyon, G.W., Delay, J., Shao, H. (2008). Hydro-Mechanical Evolution of Damaged Zones around a Microtunnel in a Claystone Formation of the Swiss Jura Mountains. American Rock Mechanics Association, ARMA 08-193.

Martin, C.D., Lanyon, G.W. (2003). Measurement of In-Situ Stress in Weak Rocks at Mont Terri Rock Laboratory, Switzerland, *International Journal of Rock Mechanics & Mining Sciences*, 40, 1077-1088.

Meier, O., Nussbaum, C., Bossart, P. (2005). HG-A experiment: Drilling of the microtunnel (BHG-A0 and BHG-A1), Mont Terri Project, TN 2005-55.

Nater, P. (2012). Mont Terri / FE-Experiment Geomechanische Modellierung des Vortriebs. NAGRA AN 12-184.

Nussbaum, C., Bossart P. (2006). HG-A experiment: Mapping of new breakouts developed in the HG-A microtunnel about 11 months after the excavation, Mont Terri Project, TN 2006-31.

Nutt, M. (2011). Used Fuel Disposition Campaign Disposal Research and Development Roadmap (FCR&D-USED-2011-000065 REV0), U.S. DOE Used Fuel Disposition Campaign.

Olivella, S., Gens A. (2000). Vapour transport in low permeability unsaturated soils with capillary effects, *Transport in Porous Media,* 40, 219–241.

Pariseau, W.G. (2006). Design Analysis in Rock Mechanics. London ; New York: Taylor & Francis.

Pollard, D.D., Fletcher, R.C. (2005). Fundamentals of Structural Geology, Cambridge University Press, Cambridge, U.K.

Pruess, K., Oldenburg, C.M., Moridis, G. (2011). TOUGH2 User's Guide, Version 2.1, LBNL-43134(revised), Lawrence Berkeley National Laboratory, Berkeley, California.

Rizzi, M., Seiphoori, A., Ferrari, A., Ceresetti, D., Laloui, L. (2011). Analysis of the Behaviour of the Granular MX-80 bentonite in THM-processes; Orders No 7'928 and 5'160; Swiss Federal Institute of Technology: Lausanne, 2011.

Rutqvist J., WuY.-S., Tsang C.-F., Bodvarsson G. (2002). A modeling approach for analysis of coupled multiphase fluid flow, heat transfer, and deformation in fractured porous rock, *International Journal of Rock Mechanics and Mining Sciences*, 39, 429-442.

Rutqvist, J., Ijiri, Y., Yamamoto, H. (2011). Implementation of the Barcelona Basic Model into TOUGH–FLAC for simulations of the geomechanical behavior of unsaturated soils, *Computers &Geosciences*, 37, 751-762.

Rutqvist, J., Zheng, L., Chen, F, Liu, H.-H, Birkholzer, J. (2013a). Modeling of Coupled Thermo-Hydro-Mechanical Processes with Links to Geochemistry Associated with Bentonite-Backfilled Repository Tunnels in Clay Formations. *Rock Mechanics and Rock Engineering*, (In Press, January 2013).

Rutqvist, J., Chen, F., Birkholzer, J., Liu, H.-H., Müller, H., Garitte, B., Vietor, T. (2013b). Modeling of coupled thermo-hydro-mechanical processes at Mont Terri heater experiment in Opalinus Clay, using TOUGH-FLAC. Proceedings of the 2013 International High-Level Radioactive Conference (IHLRWM), April 28 – May 2, 2013.

Salamon, M.D.G. (1968). Elastic Moduli of a Stratified Rock Mass, *Int. J. Rock Mech. Min. Sci.,* 5, 519-527.

Shlangen, E., Van Mier, J.G.M. (1992). Experimental and numerical analysis of micromechanism of fracture of cement-based composites, *Cement and Concrete Composites*, 14, 105-118.

Tang, C.A. (1997). Numerical simulation of progressive rock failure and associated seismicity, *Int. J. Rock Mech. Min. Sci*., 34, 249-262.

Thury, M., Bossart., P. (1999). The Mont Terri Rock Laboratory, a New International Research Project in a Mesozoic Shale Formation, in Switzerland, *Engineering Geology,* 52, 347-359.

Tonon, F., Amadei, B. (2003). Stresses in anisotropic rock masses: an engineering perspective building on geological knowledge, *International Journal of Rock Mechanics & Mining Sciences*, 40, 1099-1120.

UFD (2012). Office of Used Fuel Disposition International Program — Strategic Plan (2013) April 2012, U.S. Department of Energy.

van Genuchten, M.T. (1980). A closed-form equation for predicting the hydraulic conductivity of unsaturated soils, *Soil Sci Soc Am J,* 44, 892-898.

Vietor, T. (2012). Mont Terri Project - FE Experiment Modelling Kick-off Meeting. February 9, 2012, Mont Terri, Switzerland. NAGRA Technical Discussion TD-217.

Wang, Y. (2011). Research & Development (R&D). Plan for Used Fuel Disposition Campaign (UFDC). Natural System Evaluation and Tool Development, U.S. DOE Used Fuel Disposition Campaign.